Land Subsidence and its Mitigation

Giuseppe Gambolati and Pietro Teatini

THE **GROUNDWATER** PROJECT

i

Land Subsidence and its Mitigation

The Groundwater Project

Giuseppe Gambolati

Professor Emeritus,
School of Engineering,
University of Padova
Padua, Veneto, Italy

Pietro Teatini

Associate Professor,
Department of Civil, Environmental and Architectural Engineering,
University of Padova
Padua, Veneto, Italy

Land Subsidence and its Mitigation

The Groundwater Project
Guelph, Ontario, Canada

Please consider signing up to the Groundwater Project mailing list and stay informed about new book releases, events and ways to participate in the Groundwater Project. When you sign up to our email list it helps us build a global groundwater community. Sign-up↗.

Cover Image: Photos showing consequences of land subsidence and ground ruptures due to groundwater pumping. Top: the seafront of Pluit district, Jakarta in Indonesia, sited a few meters below the sea level and protected by the seawater through a concrete wall that needs to be raised every few years to counteract a land subsidence of 10-20 cm/year due to aquifer overexploitation (photo by Pietro Teatini, September 20, 2019). Bottom: a large earth fissure system at Siphon Draw, Apache Junction, Arizona, USA due to deformation of aquifer system accompanying groundwater pumping (photo by Pietro Teatini, November 6, 2019).

Dedication

The first author dedicates this effort to his four granddaughters Gaia, Cloe, Gioia and Iris. The second author dedicates this effort to his wife Sabrina and sons, Alberto and Michele.

Table of Contents

The Groundwater Project Foreword

The United Nations theme for World Water Day on March 22, 2022, is "Groundwater: making the invisible visible." This aligns with the essence of the Groundwater Project (GW-Project), which is aimed at raising groundwater consciousness and strengthening groundwater expertise worldwide, and is being accomplished by publishing books and supporting materials about "all-things-groundwater".

The GW-Project, a non-profit organization registered in Canada in 2019, is committed to contribute to advancement in education and brings a new approach to the creation and dissemination of knowledge for understanding and problem solving. The GW-Project operates the website https://gw-project.org↗ as a global platform for the democratization of groundwater knowledge and is founded on the principle that:

"Knowledge should be free and the best knowledge should be free knowledge." Anonymous

The mission of the GW-Project is to provide accessible, engaging, high-quality, educational materials, free-of-charge online in many languages, to all who want to learn about groundwater and understand how groundwater relates to and sustains ecological systems and humanity. This is a new type of global educational endeavor in that it is based on volunteerism of professionals from different disciplines and includes academics, consultants and retirees. The GW-Project involves many hundreds of volunteers associated with more than 200 organizations from over 14 countries and six continents, with growing participation.

The GW-Project, which began publishing books in August 2020, is an ongoing endeavor and will continue with hundreds of books being published online over the coming years, first in English and then in other languages, for downloading wherever the Internet is available. The GW-Project publications also include supporting materials such as videos, lectures, laboratory demonstrations, and learning tools in addition to providing, or linking to, public domain software for various groundwater applications supporting the educational process.

The GW-Project is a living entity, so subsequent editions of the books will be published from time to time. Users are invited to propose revisions.

We thank you for being part of the GW-Project community. We hope to hear from you about your experience with using the books and related materials. We welcome ideas and volunteers!

The GW-Project Steering Committee

July 2021

Foreword

Fresh groundwater resources provide many benefits to humanity and ecological systems, but pumping water from aquifers often has problematic consequences. One such consequence is subsidence of the land surface in urban areas caused by compaction of the low-permeability clay or silt beds that overly, underly or occur within the pumped aquifer, which is the subject of this book. The compaction occurs because the porosity of clay and silt beds decreases as the pore-water pressure declines. The aquifer provides the water while the low permeability beds cause the problem of compaction-induced subsidence of the land surface.

People living on the subsiding land do not sense that their land surface is changing position as when earthquakes occur. Substantial subsidence occurs over a period of years or decades, but the municipal engineers see subsidence effects early because slight subsidence begins to cause water problems due to changes in the slope of streets, ditches and sewer lines such that rainfall cannot escape as before. Areas where substantial subsidence causes problems are a small fraction of the global area in which aquifers have been heavily pumped because most low-permeability beds associated with aquifers are not porous enough to undergo large decreases in porosity. However, a substantial fraction of the global population lives in cities where subsidence is problematic and increasing. This is because the geology of aquifer systems most prone to compaction and subsidence are situated along coasts, especially where rivers discharge to the ocean. This geographical setting typically has thick soft, exceptionally porous deposits of young geological age so that minimal compaction has occurred over geological time, which makes human induced compaction likely. This geological setting exists where most of the world's expanding megacities are located including Alexandria, Bangkok, Dhaka, Ho Chi Minh City, Houston, Jakarta, Lagos, New Orléans, Rotterdam and Shanghai. Land subsidence is one of the world's underrated problems with consequences exacerbated by sea level rise as the climate changes.

The two authors of this book, Beppe Gambolati and Pietro Teatini, are distinguished professors in Italy and it is fitting that this book comes from Italy where the magnificent City of Venice has been recognized globally for its land subsidence problem for centuries. Although subsidence is primarily a result of groundwater pumping, the quantitative study of subsidence now resides in the discipline of geotechnical engineering and soil mechanics, which is where these book authors are founded and have global experience concerning subsidence problems.

John Cherry, The Groundwater Project Leader

Guelph, Ontario, Canada, June 2021

Preface

Land subsidence, that is, the loss of land elevation, is a major geomechanical process that threatens viability and sustainable development of many millions of people throughout the world, especially in, but not restricted to, coastal and highly urbanized areas. The most severe cases of land subsidence are associated to groundwater overdraft. Unfortunately, the unsustainable use of land and water resources is expected to increase in the next few decades, mainly in developing countries of Asia and Africa. The effects of climate change in terms of sea level rise, variation in the distribution and timing of precipitation, runoff and aquifer recharge will be compounded by an increasing concentration of population in (mega-) cities and elsewhere along the coasts of the world. The expanding need for freshwater resources in more and more concentrated, at-risk, areas will inevitably lead to an increase of sites affected by land subsidence, with a growing number of people involved.

Almost one century has passed since scientists started to investigate land subsidence of anthropogenic origin. Impressive progress has been made in terms of: a) recognizing the basic hydrologic and geomechanical principles; b) measuring aquifer compaction and ground displacements, in both the vertical and horizontal directions; c) modeling historic and simulating predicted future events; and, d) mitigating environmental impact through aquifer recharge and/or surface water injection.

This book addresses anthropogenic land subsidence, the most widespread and studied geomechanical response to groundwater pumping. A historical review is followed by a description of the major areas that have experienced considerable land subsidence illustrating a selection of the major environmental impacts. The main factors controlling the process and the basic principles and equations underlying it are discussed, with reference to the most relevant soil stresses and properties. Pumping from water table, confined and complex aquifer systems is outlined. Compaction of low permeability formations (aquitards) along with time-factor and compaction profiles are analyzed. The most advanced tools for recording and monitoring in situ deformation and surface displacements are mentioned. The occurrence opposite to land settlement, that is, the upheaval of land surface induced by aquifer recharge or water injection into the subsurface, is also reviewed. A few processes are mentioned which are still poorly understood, such as the influence of differential vertical compaction, horizontal displacements, and discontinuity in the bedrock on near-surface ground ruptures, fissure generation and fault reactivation including induced seismicity. Finally, the discussion focuses on the connection between research into groundwater geomechanics and the present challenges to be met in undertaking effective remedial measures aimed at mitigating the associated environmental and socio-economic impact.

Acknowledgements

The first author is indebted to R. Allan Freeze for introducing him to the issue of groundwater modeling, with special reference to groundwater pumping and related anthropogenic land subsidence in Venice, Italy.

We deeply appreciate the thorough and useful reviews of and contributions to this book by the following individuals:

- ❖ William Woessner, University of Montana, USA;
- ❖ Herb Wang, University of Wisconsin, USA; and,
- ❖ Tomo Tokunaga, The University of Tokyo, Japan.

The author and editors are grateful for the oversight of Amanda Sills and copyediting of Elhana Dyck, both of the Groundwater Project, Guelph, Ontario, Canada; and Eileen Poeter (Colorado School of Mines, Golden, Colorado, USA) for reviewing, editing and producing this book.

1   Introduction

Land subsidence is a sudden or gradual settling of the land surface caused by changes in the stress regime of the structure of subsurface. Subsidence driven by groundwater extraction most commonly occurs when aquifer materials are composed of lenses or layers of fine-grained compressible sediments in which pore-water heads are lowered causing sediment compaction. This reduction in volume results in a lowering of the land surface. Injecting water into aquifer systems has sometimes mitigated this anthropogenic subsidence; however, compaction of fine-grained sediments is not completely reversible in most cases. Land subsidence can be a major geomechanical consequence of groundwater withdrawal and results in:

- lowering of the elevation of the ground surface, that is, land subsidence, as a result of aquifer overdraft;
- formation of earth fissures caused by groundwater pumping in subsiding basins, especially in arid and semiarid regions;
- activation of pre-existing shallow faults, creating a failure of the land surface; and,
- induction or triggering of micro-seismic and seismic events because of changes in the natural stress regimes.

Additional impacts can also occur when aquifers experiencing subsidence are naturally recharged or attempts to stabilize or reverse groundwater related land subsidence by injecting water into the aquifers occurs. Upheaval of the ground surface has been observed in a number of areas as shown later in this book.

1.1   General Concepts and Principles

The mechanism by which rock and sediments deform and compact under the influence of a change in pore water pressure is well understood. In aquifer systems the total geostatic load acting on the aquifer and confining beds is balanced by the pore water pressure and the effective vertical and horizontal stresses (Figure 1). When an aquifer is pumped, pore water pressure can no longer support as large a percentage of the load from overlying formations. Therefore, more of this load must be borne by the grain-to-grain contacts (effective stress) of the geological material itself, with a stress transfer from the fluid to the solid phase. This increase in effective stress develops in both the pumped units and the adjacent formations (that is, intervening aquitards and confining beds) that compact. The amount of compaction is primarily related to the compressibility of the compacting layers. The resulting cumulative compaction of subsurface layers extends its effect to the ground surface, which therefore subsides (Figure 2). Pore-water pressure also can increase when water is added to an aquifer by natural recharge or injection. In some settings this may partially reverse, or mitigate, subsidence.
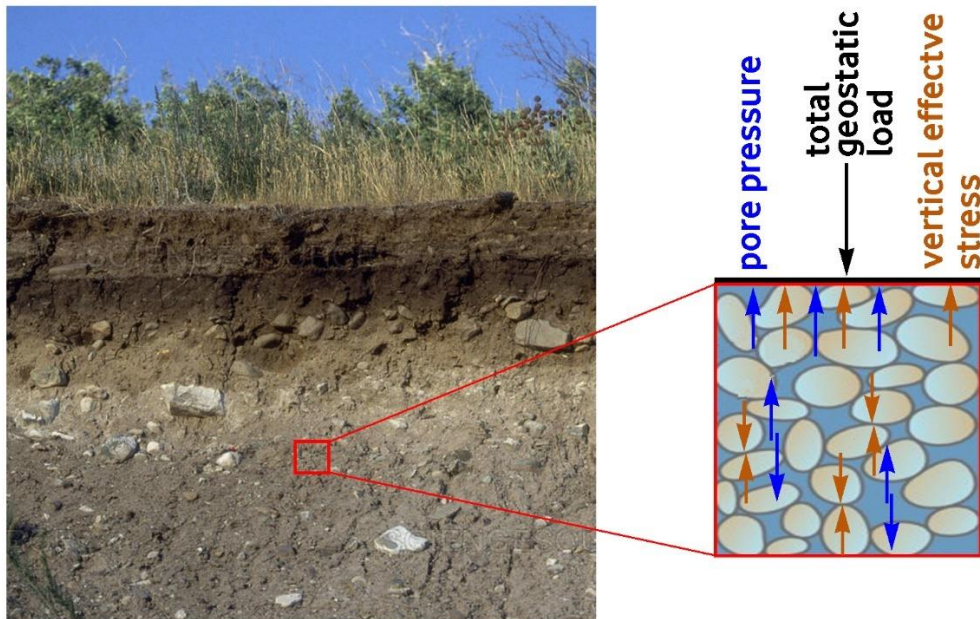
Figure 1 - The total geostatic load is supported by the vertical effective stress (in red) and the pore water pressure (in blue).
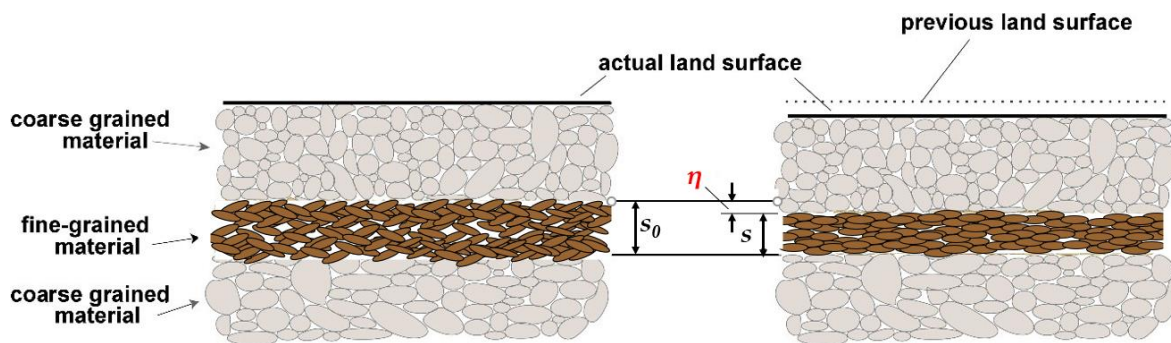
Figure 2 - Soil compaction η with a reduction of the porous space (grains are incompressible for all practical purposes).

The introduction of a pumping well into a natural fluid flow system produces a disturbance that propagates its effect in space and time through the geological medium. Around the well, a fluid head cone of depression develops and expands laterally, and to a minor extent also vertically (Figure 3). The magnitude and timing of the head drop caused by pumping depends on the distance between the well and the point of observation, the geometric, geologic configuration and boundaries of the subsurface basin and the geomechanical properties of both the fluid and formation: specifically, fluid density and viscosity and intrinsic medium permeability, porosity, and compressibility (Figure 4).

2
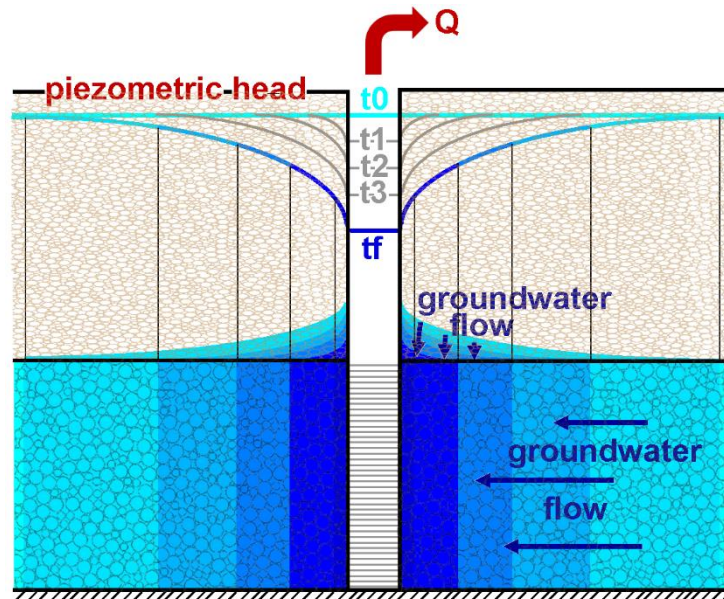
Figure 3 - Groundwater withdrawal from a well causes piezometric head decline in the pumped aquifer (darker blue represents lower head) and, to a lesser extent in the overlying fine-grained sediments. The piezometric head declines over time from the initial time (t0) level to the final time (tf) coned-shaped distribution.
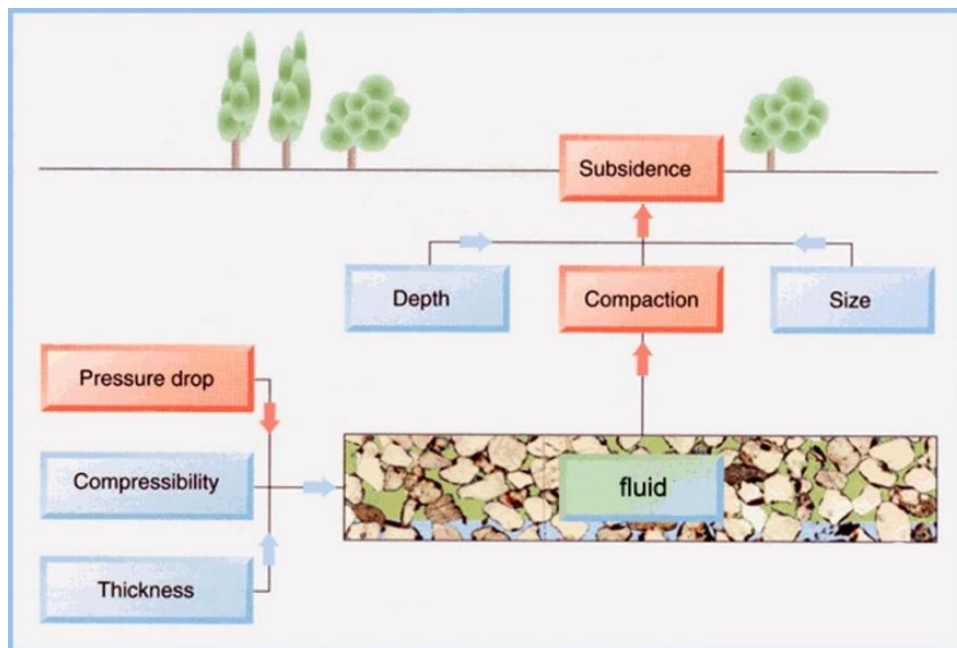
Figure 4 - Main factors controlling land subsidence due to subsurface fluid removal are the magnitude of the reduction of pore water pressure in the pumped strata and its thickness and compressibility that control the resulting amount of compaction; then the depth and extent of the compacted material influences the magnitude and distribution of subsidence at the surface. When compaction is deep and of limited lateral extent, surface subsidence is less than when compaction is shallow and wide spread.

When a porous body experiences a change in the internal flow and stress fields, due, for example, to a sedimentation process producing a total stress increase, or to fluid pumping which causes a decrease in pore pressure, the incremental effective stress and the

3

fluid-dynamic gradient that develop are intimately connected. This connection was first recognized by Biot (1941), who developed the coupled theory of consolidation (and hence the coupled theory of land subsidence) where flow and stress are intimately. It states that fluid flow influences the porous medium's deformation, which in turn affects the flow field. Groundwater hydrologists, who are mainly concerned with the fluid-dynamic aspects of this coupled interrelation, have advanced the uncoupled theory of flow, based on the so-called diffusion equation. Theis (1935) solved the single-phase flow of groundwater by incorporating the rock structural properties into a lumped geomechanical parameter (that is, the elastic storage coefficient S_s defined in the next section). Theis' solution to the diffusion equation is calculated separately, independently of the medium structural solution, in order to provide the pore pressure distribution. Once obtained, the pore pressure is used as the external driving force in predicting the medium deformation with a geomechanical model: in particular, the vertical displacement at the ground surface, that is, land subsidence.

Land subsidence has been documented to occur during some deep oil and gas reservoir pumping and during groundwater extraction. Let us compare anthropogenic land subsidence over gas/oil fields to that occurring over multi-aquifer systems. Due to stress/strain redistribution in the thick overburden separating the reservoir from the earth's surface, settlement above gas/oil fields is typically less than reservoir compaction, but it spreads over an area extending beyond the field itself (Figure 5a).
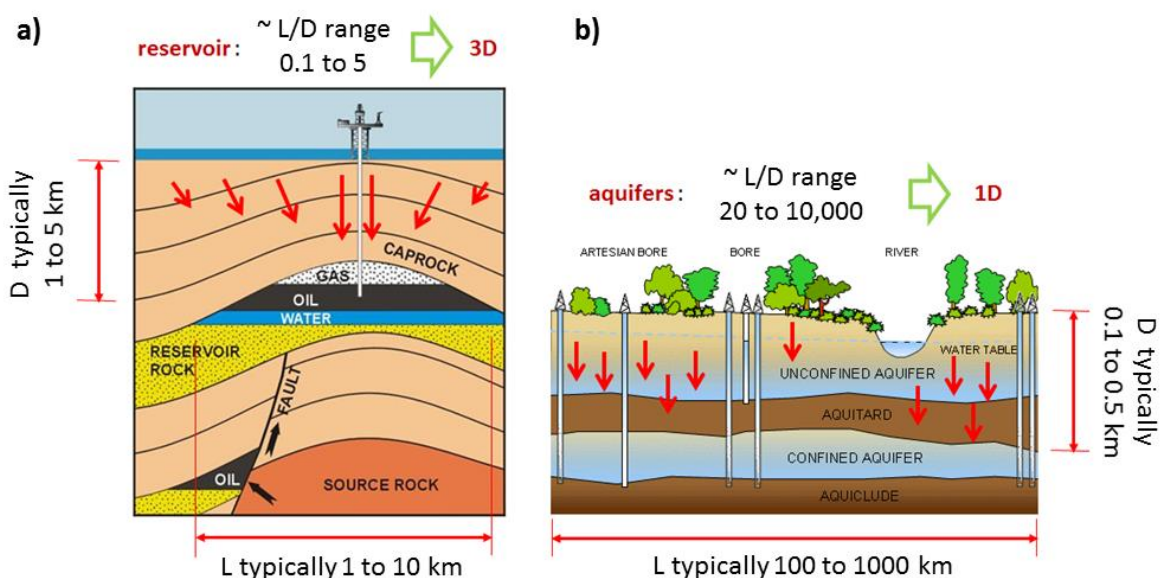
Figure 5 - Character of surface subsidence caused by fluid pumping from the subsurface. a) Oil/gas withdrawal: because of the typically large depth *D* relative to the areal extent *L*, that is, a relatively small ratio *L/D*, the displacement field (red arrows) caused by hydrocarbon production is three-dimensional. b) Groundwater pumping from an aquifer generally occurs from wells distributed over an area much larger than the aquifer depth, that is, *L/D* is large. Consequently, the displacement field is predominantly one-dimensional, along the vertical direction.

Conversely, aquifer systems are generally shallower and have a much larger areal extent than gas/oil fields. In these systems, sediment compaction is not contrasted by overlaying deposits and simply migrates to the ground surface. Hence, such stratified systems behave mechanically as if they were one-dimensional (1-D) structures, and, although fluid flow may be three-dimensional (3-D) (to give a simple example, vertical in the confining beds and aquitards, and horizontal in the aquifers), land displacement occurs mostly in the downward vertical direction (Figure 5b).

In addition to dimensionality, other factors differentiate the mechanism of gas/oil field compaction from that of aquifer/aquitard compaction. Usually, both subsurface environments consist of a sequence of sands and clays or sandstones and shales. Sandstones are cemented sands, whereas shales are clays that have undergone extensive mineralogical changes in the burial process associating them with hydrocarbon-bearing strata. These changes may have profoundly affected the shales' compaction properties. Most freshwater aquifer systems are normally consolidated and normally pressurized, or only slightly over-pressurized, and may lack important faults due to the typical formation mechanism involving a depositional alluvial/marine environment without significant interfering tectonic movements. However, their geomechanical simplicity may be partially offset by a litho-stratigraphic complexity related to the distribution of clayey, silty, and sandy soils within the compacting system. It is well known that clay may be up to two orders of magnitude more compressible than sand at shallow depth (Chilingarian and Knight, 1960). Hence, land subsidence of a freshwater system highly depends on the distribution of the clayey and silty fraction within confining beds, intervening aquitards, and interbedded lenses. Moreover, drainage from these beds can lag behind drainage from the producing sand, thus causing a delayed land subsidence which may manifest itself after wells shut down (Figure 6). In contrast, in deeply seated gas/oil fields, clay (shale) and sand (sandstone) tend to exhibit the same mechanical properties irrespective of lithology (Finol and Sancevic, 1995; Baú et al., 2002; Ferronato et al., 2013), which further differentiates the magnitude and extent of subsidence above pumped aquifer systems and productive gas/oil fields.

Conceptually, four factors may combine to produce measurable aquifer settlement records:

1. shallow burial depth of the pumped formations;
2. highly compressible deposits laid down in alluvial or shallow marine or lacustrine environments;
3. considerable pore pressure decline; and,
4. large thickness of the depressurized water-bearing strata.
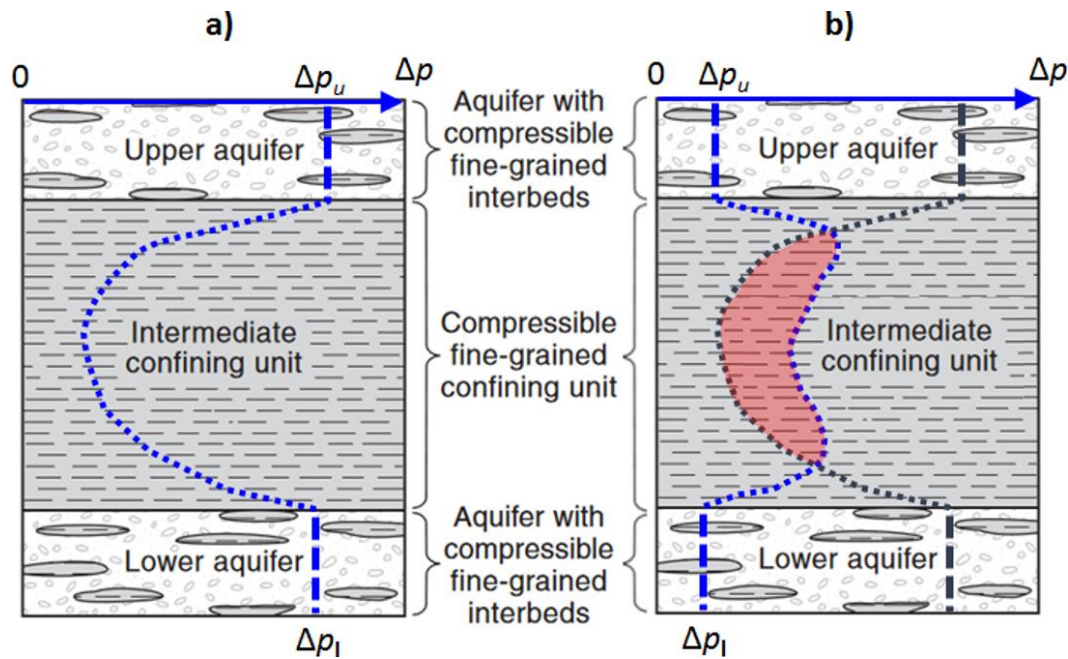
Figure 6 - Pore pressure depletion (blue dashed lines) in two aquifers and the intervening aquitard a) at the end of groundwater pumping and b) at some time after the well shutdown. The red-hatched zone represents the portion of the confining aquitard experiencing pressure decline after the well closure, that is, causing delayed subsidence.

Unless the aquifers are over-pressurized, factors 1 and 3 are mutually exclusive, while they can both be associated with factors 2 and 4. For a large subsidence to occur, however, a soft compacting deposit is needed, and/or a large pressure decline. To give a few examples, Mexico City sank by 10 m with a maximum pressure decline of only 0.7 MPa because of the extremely soft high-porosity soils of the compacting shallow formations located within the upper 50 m (Rivera et al., 1991). Settlements of 9 m and 6.7 m were reported from the Wilmington (Rintoul, 1981) and Ekofisk (Hermansen et al., 2000; Zaman et al., 1995) oil fields in California, USA, and the North Sea, Europe, respectively. These large settlements were due to the pronounced pore pressure drop (exceeding 20 MPa in the latter) combined with the considerable thickness of the compacting units. Although land subsidence above hydrocarbon fields is outside the scope of this book, it is perhaps worth mentioning that at Ekofisk the reservoir rock exhibited a sudden increase in compressibility at some stage of the field development, with a large irreversible deformation defined as "pore collapse", believed to be the main reason for the unexpected large settlement over the field (Zaman et al., 1995).

Some aquifers may be over-consolidated (Holzer, 1981). Over-consolidation tends to reduce the early subsidence rate and then generate a sudden unexpected growth at some stage of extraction when the effective stress exceeds the pre-consolidation stress. If the water- or gas/oil-bearing sediments are pre-consolidated it may be very difficult to predict anthropogenic land subsidence prior to the field/aquifer development. A pre-consolidation effect might have been caused in the geological past by uplift followed by erosion of the sediments overlying the fluid-bearing layers, by fluid overpressure, or both (Maltman,

6

1994). When pore pressure drops due to fluid removal, a reloading of the pumped formations takes place. Initially, compaction is slight, and thus, land settlement is also slight. However, as soon as the maximum experienced load is surpassed, rock compression occurs on the virgin loading curve with a sudden increase in compressibility and subsidence rate. Another factor that may influence the process is the presence of faults within the developed system and the overburden, as in the case of Las Vegas, NV, USA (Amelung et al., 1999). Faults may weaken the porous medium structure and make both analysis and prediction more difficult.

For the sake of completeness, we should mention other types of anthropogenic land subsidence that are not addressed by the present analysis. Most of them are less important in terms of socio-economic and environmental impact. They include underground mining, carbonate rock solution, subsurface erosion, surface loading, land drainage and reclamation, histosoil (peat) oxidation, dissolution of soil carbon and water application (Allen, 1984). An example of land subsidence due to peat oxidation is presented by Zanello et al. (2011).

1.2   Historical Framework

The first observation relating land subsidence to subsurface fluid removal was made in 1926 by the American geologists Pratt and Johnson (1926), who discussed land settlement on the Gaillard peninsula, in the center of Goose Creek Oil Field on Galveston Bay (Texas). They concluded that "*the Goose Creek subsidence was directly caused by the extraction of oil, water, gas, and sand from beneath the surface beginning in the year 1917*". They also made a conjecture concerning the mechanism governing the underlying process, postulating that "*the pore spaces are occupied by water draining more slowly from the adjacent clays; and it is a well-known fact that the draining of clays causes them to become more compact, and this in turn would permit subsidence of overlying surface*". However, a few years earlier, Fuller (1908) had already theorized that fluid withdrawal and a decrease in fluid pore pressure caused the sinking of the land surface because of the removal of hydrostatic support.

It is interesting to note how the general public's perception of anthropogenic land subsidence has drastically changed over time. Today the occurrence of settlement affecting large areas is a matter of great concern from a variety of viewpoints involving economic, environmental, and safety issues. In regions where ground sinking is caused by both groundwater pumping and hydrocarbon production, we may often see one party unload responsibility onto another. In the 1920s this was not the case, as we see from the poignant example of the Goose Creek oil field. The Gaillard peninsula, located at the mouth of Goose Creek and overlying part of the oil field, began to settle and was soon covered by the waters of San Jacinto Bay. By 1925 maximum subsidence had exceeded one meter and the area affected was about 4 km long and 2.5 km wide, approximately consistent with the boundary of the producing wells (Figure 7). The State of Texas claimed title to the lands

submerged by the subsidence and sought to recover the value of oil removed after the submergence. The court, however, decided in favor of the defendants, accepting their contention that the subsidence was not the result of a natural process but generated by an act of man, namely the removal of large volumes of fluids and sand from the underground "*No act of man can operate to deprive another man of his property under the law.*" If the subsidence had been a natural process, "*an act of God*", then presumably title to the submerged land and the underlying reserves would have passed to the state of Texas.
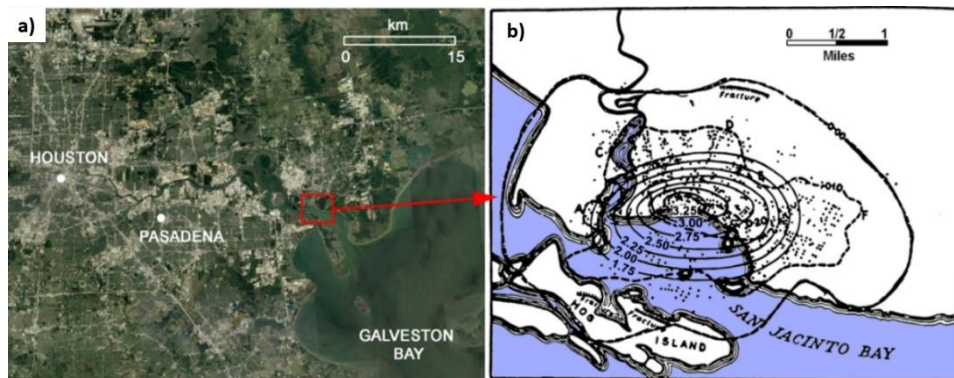
Figure 7 - a) Location of the Goose Creek mouth on the Galveston Bay close to Houston, Texas, USA. b) Land subsidence map (in feet, 100 feet is approximately 30.5 meters; 1 mile is approximately 1.6 kilometers) provided by Pratt and Johnson (1926).

Quantitatively speaking, the principle of effective intergranular stress advanced by Terzaghi (1923) showed soil consolidation as the primary cause of land settlement. Soon, this principle was recognized as being an active factor in the compaction of an aquifer (the Dakota Sandstone) (Meinzer and Hard, 1925), who stated that the overburden pressure of all beds above the confined Dakota aquifer was supported partly by the fluid pressure and partly by the sandstone itself, via the effective intergranular stress. They concluded that the grain-to-grain load had increased by about 50 percent because of the decline of artesian head. Based on both laboratory tests and field measurements, Meinzer (1928) cited evidence indicating the compressibility and elasticity of artesian aquifers. He recognized that water withdrawn from storage was released by compression of the aquifer and by expansion of the water, and that reduction of storage (compression) may be permanent (inelastic) as well as elastic.

Rappleye (1933) provided the first specific records of subsidence due to groundwater pumping in the Santa Clara Valley (California, USA), and Ingerson (1941) described the subsidence in the Delano-Tulare-Wasco (California, USA) area. He presented a map and profiles of land subsidence based on comparison between leveling surveys performed in 1902, 1930, and 1940. By this time the relationship between the removal of subsurface fluid (water, oil, gas) and land subsidence was recognized, at least in the USA.

Jacob (1940) postulated that when water is pumped out from an elastic artesian aquifer system and pore pressure is decreased. As a result, withdrawn water is derived from water expansion, aquifer compression, and compression of the adjacent and

8

intervening clay beds. He stated that the third source is probably the chief one: "*because of the low permeability of the clays (or shales) there is a time lag between the lowering of pressure within the aquifer and the appearance of that part of water which is derived from storage in those clays (or shales)*". Subsequently Lohman (1961) developed an equation for determining the amount of elastic compression of artesian aquifers from known declines in artesian pressure and hydro-mechanical properties of the aquifers. This compression was intended as being transferred to the ground surface, producing an estimate of the resulting land subsidence.

In the late fifties and sixties, the concept interrelating land subsidence and fluid withdrawal was universally accepted thanks to the fundamental contributions by Poland, a pioneer in anthropogenic land subsidence studies (Poland and Davis, 1969). Around the same time the principle of effective stress was universally recognized in geomechanics (Taylor, 1948; Terzaghi and Peck, 1948; Leonards, 1962). By the end of the sixties the concept and the mechanism underlying land subsidence of anthropogenic origin were clear. The way was open to new progress in the mathematical formulation of equations governing the process and corresponding solutions helpful in predicting expected land subsidence in exploited aquifer systems. A pioneering finite element model of the anthropogenic land subsidence of Venice is discussed by Gambolati and Freeze (1973) and Gambolati et al. (1974).
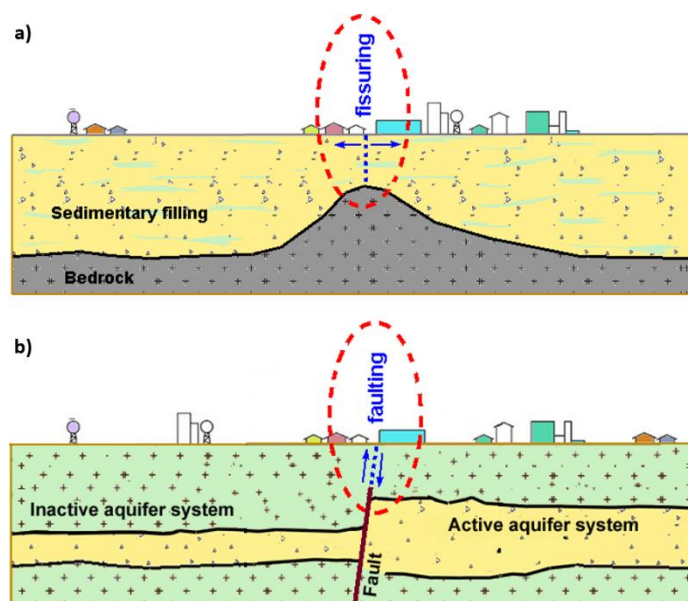
Figure 8 - a) Fissuring and b) faulting due to deformation of aquifer systems accompanying groundwater pumping.

A second important geomechanical effect associated with groundwater pumping from unconsolidated sedimentary aquifer systems is ground rupture. The nature of ground failure may range from fissuring, that is, formation of an open crack, to faulting, that is, differential offset of the opposite sides of the failure plane (Figure 8).

9

Ground ruptures associated with land subsidence were first observed in 1949, in central Arizona, by Feth (1951). In the wake of this pioneering work, it would take more than 20 years for the United States Geological Survey to undertake major investigations examining earth fissures in subsiding areas of the southwestern United States (California, Arizona, Texas, and Nevada). Holzer and Pampeyan (1981) recognized that "*the areal and temporal association of earth fissures with land subsidence caused by groundwater withdrawal indicated that these fissures were man induced*". The underlying mechanism was highlighted at that time, as soon as enough field data became available to test the hypothesis. Bending caused by localized differential displacements was originally proposed by Feth (1951) to explain the observed fissuring. He speculated that it might have been caused by extensional strains generated by locally varying degrees of subsidence. He attributed the differential subsidence to abrupt variations in aquifer thickness. Lofgren (1971) suggested that horizontal displacements measured in subsiding areas might be due to horizontal seepage forces. Based on the association of earth fissures with water table decline and other field evidence suggesting fissures formed at depth and propagated upward, Holzer and Davis (1976) held that fissures were caused by desiccation due to water table lowering. Over the last decade, the availability of three-dimensional geomechanical models has allowed for preliminary attempts at simulating ground ruptures as they relate to anthropogenic alterations in the porous medium stress state. Modeling suggests that primary controls are reactivation of a preexisting fault, differential compaction due to variations in thickness of aquifer/aquitard layers constituting the aquifer system, and tensile fracturing above bedrock ridges that form the base of the aquifer system.

1.3 Occurrence

Land subsidence is perhaps the most widespread and threatening geomechanical consequence of groundwater pumping. When groundwater withdrawals occur in densely populated and highly developed areas underlain by unconsolidated geological basins of alluvial, lacustrine or shallow marine origin, formed typically, although not exclusively, in the Quaternary period land subsidence is likely. Areas located close to the sea or a lagoon or delta are often impacted by subsidence. Quite often, especially at the onset of the occurrence, land settlement goes unnoticed, only to be discovered later on, when severe damage has already taken place. At this stage, undertaking effective remedial measures to mitigate the associated environmental and socio-economic impact may prove tremendously expensive. However, in recent times our awareness concerning the damage threatened by potential anthropogenic land subsidence has significantly grown at both the political and the general public level, thus contributing to lower the alarm threshold. As a major result, the most recent plans for subsurface resource development usually include a study of the related environmental impact presenting, wherever appropriate, numerical predictions of the expected land settlement above (and close to) the exploited system.

Figure 9 shows the areas of major anthropogenic land subsidence due to groundwater extraction worldwide. Table 1 gives the most significant records of the occurrences depicted in Figure 9. The maximum recorded land settlement of all time amounts to more than 14 m and was due to geothermal water production at Wairakei geothermal field, New Zealand (Allis et al., 2009) as shown in Figure 10a. However, settlement depths approaching 10 m are not unusual as in the San Joaquin Valley, California, USA (Galloway and Riley, 1999) and as shown in Figure 10 for Mexico City, Mexico (Cabral-Cano et al., 2008; Otiz-Zamora and Ortega-Guerrero, 2010).
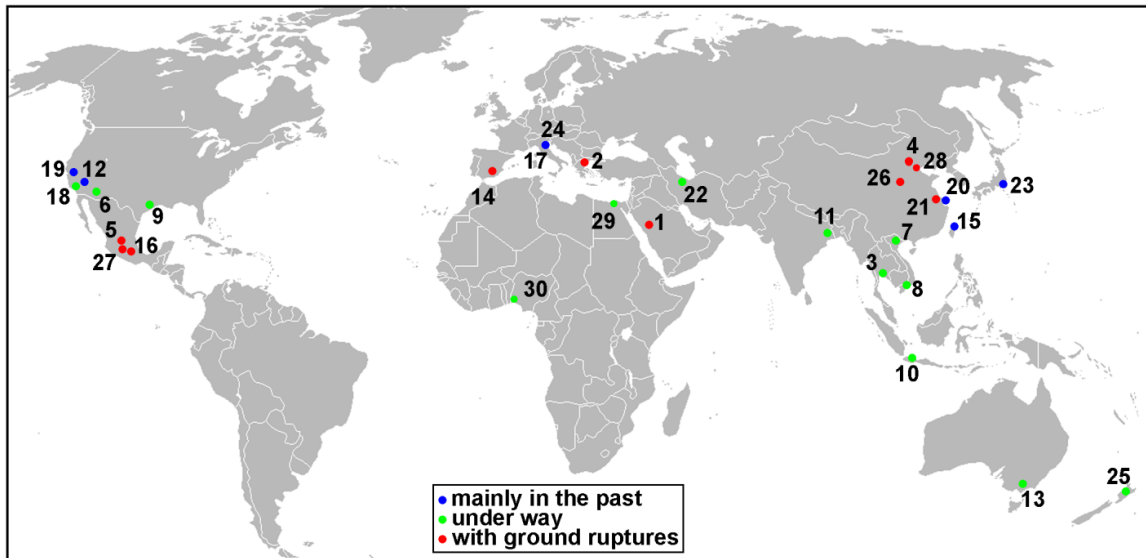
Figure 9 - Major worldwide areas of anthropogenic land subsidence due to groundwater withdrawal. Different symbols are used to distinguish cases of subsidence (i) occurring mainly in the past, (ii) still under way, and (iii) associated with ground rupture. 1: Wadi Al-Yutamah, Saudi Arabia; 2: Anthemountas Basin, Greece; 3: Bangkok, Thailand; 4: Beijing, P.R. China; 5: Celaya, Mexico; 6: Eloy Basin, Arizona, USA; 7: Hanoi, Vietnam; 8: Ho Chi Minh, Vietnam; 9: Houston, Texas, USA; 10: Jakarta, Indonesia; 11: Kolkata, India; 12: Las Vegas, Nevada, USA; 13: Latrobe Valley, Australia; 14: Lorca, Spain; 15: Taipei, Taiwan; 16: Mexico City, Mexico; 17: Ravenna, Italy; 18: San Joaquin Valley, California, USA; 19: Santa Clara Valley, California, USA; 20: Shanghai, P.R. China; 21: Su-Xi-Chang area, P.R. China; 22: Tehran, Iran; 23: Tokyo, Japan; 24: Venice, Italy; 25: Wairakei, New Zealand; 26: Xian, P.R. China; 27: Zamora de Hidalgo, Mexico City; 28: Tianjin, P.R. China; 29: Nile River delta, Egypt; 30: Lagos, Nigeria.
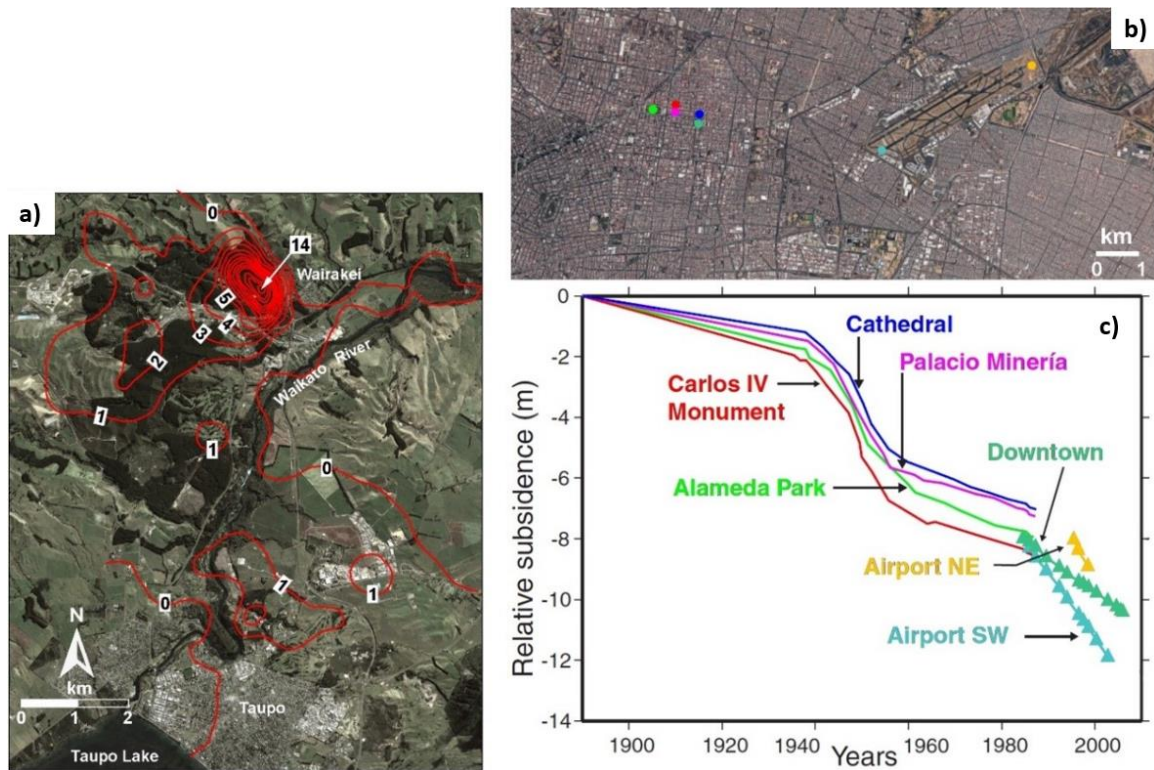
Figure 10 - a) Total subsidence at the Wairakei geothermal field over the 1953–2005 period. Contour line interval: 1 m; maximum subsidence contour line: 14 m (after Allis et al., 2009). b) The locations of the monitoring points. c) Multitechnique composite plot of the subsidence in the Mexico City downtown area since 1895. Pre-1985 leveling data were collected at selected city landmarks, whereas 1985–2002 data were derived from leveling of a modern benchmark network (after Cabral-Cano et al., 2008).

The depth of fluid abstraction wells may range from those tapping very shallow water table aquifers quite close to the ground surface, to those tapping very deep (4000-5000 m) gas/oil reservoirs. The overall extent of the sinking area can be large, totaling as much as 13,500 km² in the San Joaquin Valley (Poland and Lofgren, 1984) and 12,000 km² in the Houston-Galveston area of Texas (Gabrysch and Neighbor, 2000. China is perhaps the country with the largest cumulative area of subsidence (about 80,000 km²) subsurface water overdraft has occurred. Figure 9 also shows the major sinking cities in China (Xue et al., 2005). For an initial review of human-induced land subsidence through illustrative case histories worldwide and more recently from across the United States, the reader may consult Poland (1984) and Galloway et al. (1999), respectively.

Table 1 - Selected areas of major land subsidence due to groundwater withdrawal worldwide. The time of occurrence is provided between parentheses. Rates represent the local maximum measured rate for the specified period. Negative values indicate uplift.

#	Location	Maximum subsidence (m)	Maximum rate (cm/yr)	Depth of pumping (m)	Area of subsidence (m^2)	Principal references
1	Wadi Al-Yutamah	0.3 (1993-1996)	-	0-150	150	Banker and Al-Harthia [1999]
2	Anthemountas Basin	-	3.5 (1995-2001)	30-150	40	Raspini et al. [1933]
3	Bangkok	2.1 (1933-2002)	2 (2005-2010)	30-300	700	Phien-wej et al. [2006]; Aobpaet et al. [1999]
4	Beijing	1.1 (1955-2007)	5 (2003-2010)	20-400	4200	Zhang et al. [2014] Zhu et al. [2014]
5	Celaya	3.1 (1985-2008)	9 (2007-2011)	50-200	50	Huizar-´Alvarez et al. [2011]; Chaussard et al. [2014]
6	Eloy Basin	3.0 (1948-1977)	4 (2010-2014)	100-760	1000	Holzer et al. [1979]; Conway [2014]
7	Hanoi	0.5 (1988-2003)	7 (2007-2011)	0 - 80	35	Thu and Fredlund [2000]; Dang et al. [2014]
8	Ho Chi Minh	0.4 (1996-2005)	4 (2006-2010)	50-240	250	Erban et al. [2014]
9	Houston	3 (1915-2000)	2.5 (2005-2012)	60-900	12000	Gabrysch and Neighbors [2000]; Yu et al. [2014]
10	Jakarta	4.1 (1974-2010)	26 (2007-2011)	40-240	660	Ng et al. [2012]
11	Kolkata	1.1 (1956-2000)	4 (2001-2005)	50-160	150	Shau and Sikdar [2011]
12	Las Vegas	2 (1935-2000)	2.5 (1997-1999)	200-300	250	Amelung et al. [1999]; Hoffmann et al. [2001]
13	Latrobe Valley	1.3 (1960-1977)	1.5 (2006-2011)	0-150	400	Gloe [1984]
14	Lorca	2.2 (1992-2012)	16 (1992-2011)	50-300	140	Gonzalez et al. [2012]
15	Taipei	2 (1955-1991)	-0.7 (1989-2003)	50-250	200	Chen et al. [2007]
16	Mexico City	13 (1960 to present)	30 (2007-2011)	0-350	250	Ortiz-Zamora and Ortega-Guerrero [2010]; Chaussard et al. [2014]
17	Ravenna	1.4 (1897-2002)	0.2 (1998-2002)	80-450	400	Teatini et al. [2006]
18	San Joaquin Valley	10 (1930 to present)	30 (2007-2011)	60-600	13500	Galloway and Riley [1999]; Borchers and Carpenter [2014]
19	Santa Clara Valley	4.3 (1910-1995)	-0.5 (1992-2000)	50-280	500	Schmidt and Burgmann [2003]; Borchers and Carpenter [2014]
20	Shanghai	2.6 (1958-2002)	1.5 (2006-2011)	10-330	5000	Wu et al. [2010]; Dong et al. [2014]
21	Su-Xi-Chang area	1.1 (1960-1995)	3 (2003-2008)	20-200	4000	Shi et al. [2007]; Yu et al. [2009]
22	Tehran	3.0 (1989-2004)	15 (2004-2005)	20-100	500	Mahmoudpour et al. [2013]
23	Tokyo	4.3 (1900-1975)	-0.3 (1991-2005)	0-400	3400	Sreng et al. [2011]
24	Venice	0.12 (1952-1973)	0.1 (2008-2011)	70-350	150	Gambolati et al. [1974]; Teatini et al. [2012]
25	Wairakei	14.5 (1950 to present)	9 (2000-2007)	250-800	25	Allis et al. [2009]
26	Xian	2.3 (1959-1995)	11 (2005-2012)	50-370	240	Zhao et al. [2008]; Qu et al. [2014]
27	Zamora de Hidalgo	-	18 (2007-2011)	0-300	15	Chaussard et al. [2014]
28	Tianjin	3.2 (1959-2007)	11 (1975-1985)	0-550	8000	Yi et al. [2011]
29	Nile River delta	-	1 (2004-2010)	20-200	4800	Gebremichael et al. [2018]
30	Lagos	-	0.6 (2011-2018)	50-200	350	Cian et al. [2019]

13

1.4   Major Environmental Impacts

Some major impacts of anthropogenic land subsidence include:

- increased flood risk (frequency, depth and duration of flooding events) and more frequent inundation induced by rainfall because of the reduced effectiveness of the drainage systems;
- damages to buildings, foundations, infrastructures (roads, bridges, dikes) and underground structures (drainage, sewerage, pipes); and,
- disruption of water management and related effects (change of gradient of streams, canals, drains, increased seawater intrusion, increased pump power).

Moreover, as a result of limited available space, housing, industrial buildings and infrastructures are increasingly located in land settlement-prone areas, including flood plains and coastal marshes. These conditions may be aggravated in the long term by future climate changes climate causing sea level rise, stronger storm surges and increased precipitation.

Land subsidence causes direct and indirect damages. Direct damages include the loss of functionality and/or integrity of the structures such as buildings, roads, subways and underground utility networks (infrastructures). Indirect damages also occur such as a decrease of farmland productivity in deltaic areas because freshwater availability has been limited by an increase in saltwater intrusion (resulting from a decreased land elevation). The most common indirect effects are related to changes in relative surface and subsurface water levels. The estimation of the associated cost is quite complex. In practice operational and maintenance costs are addressed in several short- and long-term policies and budgeting. In China the average total economic loss due to anthropogenic land subsidence is estimated around 1.5 billion dollars per year 80-90 percent of which are indirect costs. In Shanghai, over the decade 2001-2010, the total cumulative loss approached two billion dollars. In Bangkok, Thailand, many private and public buildings, roads, pavements, levees and subsurface structures (sewage, drains) have been severely damaged by land subsidence although reliable estimate of costs are not available. The total cost of damage referred to subsidence in The Netherlands was estimated at over 3.5 billion euro per year.

Unexpected environmental problems can also occur after the cessation of land subsidence. When pumping regulation allows water levels to begin to recover water may begin to appear in unexpected areas. For example, in Tokyo a fast recovery of the piezometric head caused infrastructure damages by buoyant forces acting on the building foundations and groundwater seeped into the basement floor of buildings and tunnels (Tokunga, 2008). In the industrial zone on the Venice mainland, Italy, a significant re-pressurization of the deep confined aquifers occurred once the pumping was shut down in the early 1970s. More than 400 deep abandoned boreholes, improperly plugged, acted as preferential conduits that supplied water to recharge the phreatic aquifer requiring large water draining and treatment costs for the factories established in the area (Paris et al., 2010).

Prior to development, evaluation of the prospective impacts that groundwater/hydrocarbon production may have on the local environment and a set of guidelines describing steps needed to assess the potential environmental risk and implement a strategy for a "*sustainable*" development are needed. Three basic major steps can be envisaged in a control program to be set up in advance of the withdrawal inception:

1. Prediction of the expected land settlement in the area using the state-of-the-art models. These should rely on the available information supplied by the project related exploratory boreholes and the previous general knowledge of the subsurface basin of interest.

2. Continuous monitoring and measuring of the subsidence where environmental, economic and social vulnerability is high. Monitoring should start well before the inception of production so as to identify, with reasonable certainty, the actual consequences of the planned development. Land surface monitoring using methods such as spirit leveling, DGPS, Differential Global Positioning System, InSAR, and Interferometric Synthetic Aperture Radar should be conducted. Monitoring at the depth of the depleted formations should also be conducted using tools like extensometers. A network for measuring micro-seismicity should also be installed.

3. Prevention of the expected anthropogenic land subsidence or mitigation of the settlement experienced during aquifer/field development. Sensitive spots (subsidence values larger than defined sustainable) should be identified and mitigation proposed. A pressure maintenance program including options for recharging the formation with properly treated surface water should be considered.

The activities described above are obviously interconnected and data acquired in one step may be used in the others. For a recent thorough review of the major issues associated with anthropogenic land subsidence due to fluid withdrawal the reader is referred to Gambolati et al. (2005) and Gambolati and Teatini (2015). A discussion that integrates the technical, social, economic, legal, and political conflicts arising from land subsidence is provided by Freeze (2000).

2   Theory of 1-D Soil Consolidation and Aquifer Response to Pumping

Stratified systems behave mechanically as if they were one-dimensional (1-D) structures, and, although fluid flow may be 3-D, displacement occurs mostly in the downward vertical direction (Figure 5b). This presentation of the theoretical foundation used to examine anthropogenic land subsidence is a two-step process. The first step addresses the fluid-dynamic component. It controls the porous medium's flow behavior as accounted for by the elastic storage S_s. The second step solves the structural problem by using the spatial gradient of the fluid pore pressure p calculated in the first step as a driving

force within the geomechanical medium (which may be over- or under-consolidated and faulted). The spatial gradient of p controls the solid skeleton deformation and subsidence (that is, vertical displacement) at the land surface.

2.1   Effective Intergranular Stress and Soil Parameters

The theories of land subsidence are founded on basic principles of soil mechanics. Thus, the following discussion describes soil parameters, however, references to soil can be viewed as aquifer and confining bed material in a groundwater system.

The soil is viewed as a set of grains in contact. Assume a degree of saturation equal to 1 (that is, full saturation). Make a (macroscopically) horizontal cross section through the soil intersecting the contact points (Figure 11).
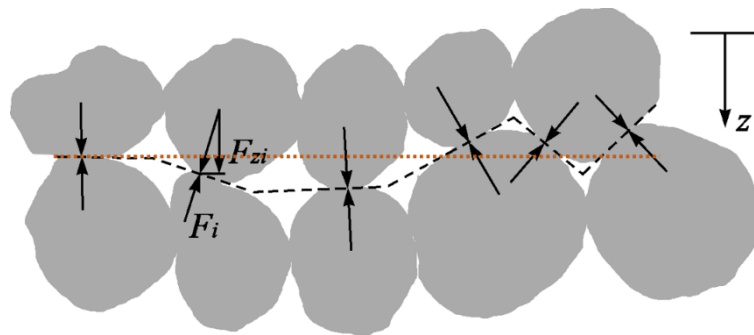
Figure 11 - Schematic vertical cross-section through a porous medium. The black dashed line is the crossing surface and the dotted orange line is the horizontal projection of the crossing surface.

Consider a piece of such a section with area A on a horizontal plane (dotted orange line, Figure 11) and n contact points (black arrows, Figure 11). If F_{zi} is the vertical component of the force that the grains exchange through the ith contact area (Figure 11), we define "*effective intergranular stress*" σ_z by Equation 1.

$$\sigma_z = \frac{\sum_{i=1}^{n} F_{zi}}{A} \tag{1}$$

Equation 1 shows that effective intergranular stress is the uniform stress over the unit horizontal projection of a crossing surface with n contact points. Stress is a force per unit area and has dimensions of $ML^{-1}T^{-2}$, that is, the same dimensions as pressure. The effective intergranular stress is equivalent to the combined individual stresses, $\sigma_{zi} = F_{zi}/A_i$ spread over the horizontal area, A, with stress taken to be positive in compression such that the force is the same. That is,

$$\sigma_z A = \sum_{i=1}^{n} \sigma_{zi} A_i$$

namely:

$$\sigma_z = \frac{\sum_{i=1}^{n} \sigma_{zi} A_i}{A} = \frac{\sum_{i=1}^{n} F_{zi}}{A}$$

16

Denote the geostatic stress by σ_c, that is, the weight of a soil column applied to a unit horizontal area at a given depth. The weight of a soil column is the combined weight of the solids and the fluids in the pores. In the case of full saturation, σ_c is equilibrated by σ_z and the pore pressure p as shown in Equation 2. The fluid pressure is distributed over the unit area minus the area of grain contacts as expressed in the parentheses of Equation 2.

$$\sigma_c = \sigma_z + p\left(1 - \sum_{i=1}^{n} A_i \cos\alpha_i\right) \tag{2}$$

where:

σ_c = geostatic stress ($ML^{-1}T^{-2}$)

σ_z = effective intergranular stress ($ML^{-1}T^{-2}$)

p = pore pressure ($ML^{-1}T^{-2}$)

α_i = angle between the contact area, A_i, and the vertical

Ai = contact area normal to the force between grains (L^2)

The contact area $\Sigma(A_i \cos\alpha_i)$ is much smaller than 1 (as explained in Box 1↓), thus the quantity within the parentheses is essentially 1, hence, on first approximation, Equation 2 becomes Equation 3.

$$\sigma_c = \sigma_z + p \tag{3}$$

The geostatic load σ_c is also called "*total vertical stress*". If σ_c remains constant during pumping (this is essentially the case for a pumped confined aquifer because pores do not drain), a decrease of p induces an equal increase of effective intergranular stress, σ_z, under whose effect the pumped formation compacts. Of course, this is a preliminary analysis. A more complete study should take into account second order effects such as the forces of mutual attraction among the grains and the fluid surface tension as well as the gas pressure in partially saturated soils.

To evaluate the compaction of a formation with decreased pore pressures we need to define a few dimensionless characteristic soil parameters:

- the void ratio e, that is, the ratio of the pore volume to the grain volume; and,
- the porosity ϕ, that is, the ratio of the pore volume to the total volume.

The following relationships hold:

$e = P$oreVolume/(TotalVolume - PoreVolume) = $\phi/(1 - \phi)$

$\phi = e/(1 + e)$

A most important experimental profile is the behavior of e versus σ_z as derived from laboratory tests on soil samples from the compacting formation. Qualitatively, the behavior of e versus σ_z is shown in Figure 12. If the effective intergranular stress increases, the formation compacts and e decreases. As a first approximation, we assume the grains to be incompressible (the grains are much, much stiffer than the porous matrix, and especially

17

so in shallow soils). This implies that the porous medium compaction is due essentially to the reduction of the pore volume, that is, the reduction of e and ϕ.
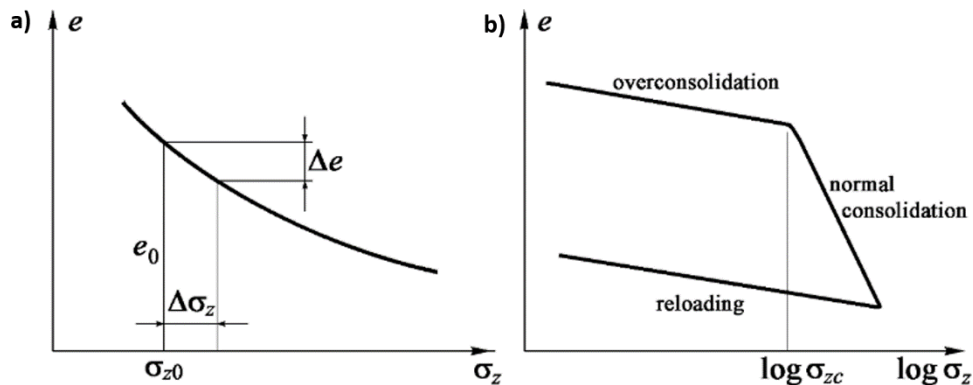
Figure 12 - Typical behavior of the void ratio e against a) the effective intergranular stress σ_z and b) log σ_z. The over-consolidation (if present), normal consolidation, and reloading phases are highlighted on (b). Over-consolidation denotes a soil that has, in the past, experienced a maximum effective stress equal to σ_{zc} that was later reduced (e.g., because of surface erosion).

The total compaction η of a layer (η has dimensions of length) as illustrated in Figure 2 (repeated here for the readers convenience) with initial thickness s_0 and initial void ratio e_0 is completely due to reduced pore space as reflected by Equation 4.
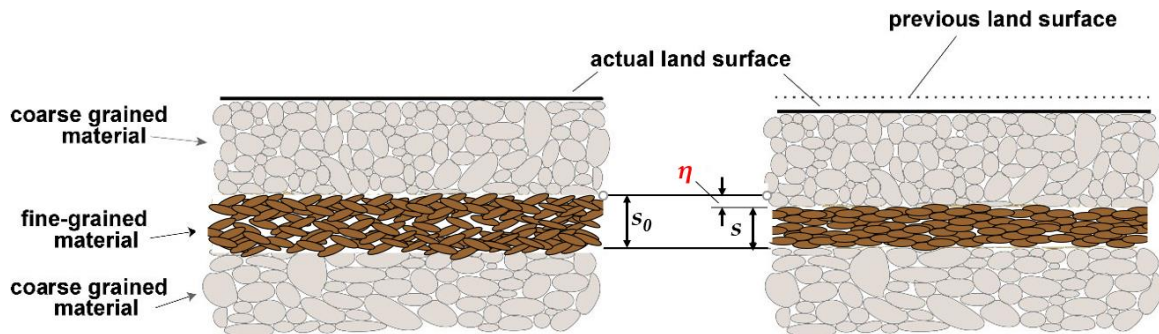
Repeat of Figure 2 for the reader's convenience - Soil compaction η with a reduction of the porous space (grains are incompressible for all practical purposes).

$$\eta = s_0 \frac{\Delta e}{1 + e_0} \tag{4}$$

Equation 4 is readily derived by means of the following geometric consideration: if we assume the solid grains are incompressible, the grain volume "disappeared" because of compaction must be equal to the increased volume of the grains within the compacted layer. Let A represent the horizontal area of the compacting layer. With reference to Figure 2, the grain volume loss due to compaction η is equal to $\eta A(1 - \phi_0)$, i.e.,

$$\eta A/(1 + e_0)$$

18

and the increased grain volume in the compacted layer is equal to $sA\big((1 - \phi) - (1 - \phi_0)\big)$, that is,

$$(s_0 - \eta)A \left(\frac{1}{1 + e_0 - \Delta e} - \frac{1}{1 + e_0} \right).$$

Then, equating the above two equations and rearranging yields Equation 4.

The uniaxial vertical soil compressibility c_b is the fractional change in volume, $d(\Delta V)/\Delta V$, in response to a unit change in stress, $d\sigma_z$, and has dimensions of inverse stress $M^{-1}LT^2$.

$$c_b = \frac{d(\Delta V)}{d\sigma_z} \frac{1}{\Delta V}$$

where:

$$c_b \;=\; \text{uniaxial vertical soil compressibility } (M^{-1}LT^2)$$

$$\Delta V \;=\; \text{volume before compaction } (L^3)$$

Since $d(\Delta V)/\Delta V$ = (Pore Volume change)/(Pore Volume + Grain Volume) = $\Delta e/(1 + e)$, we can substitute $\Delta e/(1 + e)$ for $d(\Delta V)/\Delta V$ to obtain the following expression for c_b.

$$c_b = \frac{1}{d\sigma_z} \frac{\Delta e}{(1 + e)}$$

The uniaxial vertical soil compressibility can be expressed as shown in Equation 5 by including a minus sign so as to obtain a positive c_b value (σ_c and σ_z are assumed to be positive even though they are compressive stresses). Then, compressibility, c_b, can be estimated in the laboratory by finding the slope of the experimental profile shown in Figure 12a and evaluating Equation 5.

$$c_b = -\frac{de}{d\sigma_z} \frac{1}{1 + e} \tag{5}$$

The minus sign in the above equation is introduced so as to obtain a positive c_b value (σ_c and σ_z) are assumed to be positive although they are compressive stresses). Assume c_b is constant, then Equation 5 leads to:

$$\frac{de}{1 + e} = -c_b d\sigma_z$$

and integration leads to:

$$ln(1 + e) = -c_b \sigma_z + C$$

which simplifies to Equation 6.

$$e = C \exp^{(-c_b\sigma_z)} - 1 \tag{6}$$

The integration constant C is determined by prescribing that $e = e_0$ for $\sigma_z = \sigma_{z0}$, thus C is:

19

$$C = (1 + e_0) \exp^{-(-c_b\sigma_{z0})}$$

and substituting C into Equation 6 results in Equation 7.

$$e = (1 + e_0) \exp^{[-c_b(\sigma_z - \sigma_{z0})]} - 1 \tag{7}$$

Generally, e_0 corresponds to the initial conditions where $\sigma_z = \sigma_{z0}$ prior to the inception of pumping. The assumption of constant c_b has validity over a limited range of σ_z. The porous medium becomes stiffer as $\Delta\sigma_z$ increases and compaction progresses. Therefore, Equation 7 will be used for σ_z values falling within a given stress range. In general, c_b will be calculated using Equation 5 once the profile of Figure 12 is available.

2.2   Pumping from a Water Table Aquifer

For the sake of simplicity, assume a water table aquifer is horizontal and the piezometric decline due to pumping over a given time interval is Δz. Let θ_w be the moisture content (i.e., the fraction of the total porous medium volume occupied by water, moisture content is equal to porosity in a fully saturated medium) within the unsaturated zone above A, and, between the phreatic surfaces (labeled as the piezometric levels A and B in Figure 13) after the piezometric surface has declined from A to B.
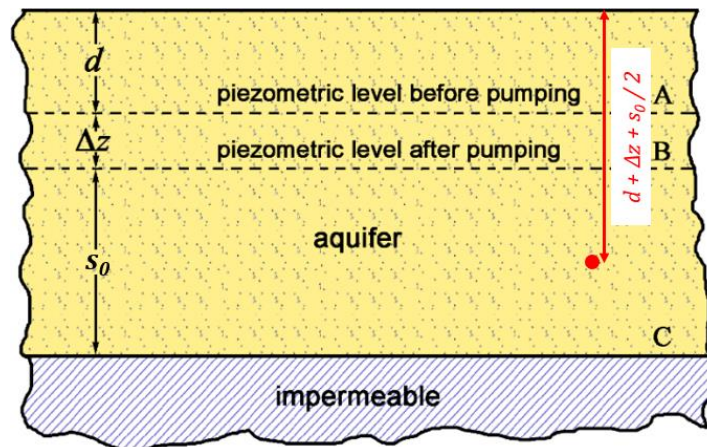
Figure 13 - Sketch of a pumped water table aquifer.

As a result of lowering the piezometric level, there will be an increase of effective stress due to drainage of water from the zone between A and B because that zone is no longer under the influence of pore water pressure (Archimedes' upward buoyant force). At any point location between B and C, the geostatic stress, σ_c, is decreased by the quantity $\gamma\Delta z(\phi - \theta_w)$, with γ being the specific weight of water with dimensions $\text{ML}^{-2}\text{T}^{-2}$, and the quantity $\gamma\Delta z$ being p. Therefore, the effective stress, σ_z, is increased by (Equation 8),

$$\Delta\sigma_z = \gamma\Delta z(1 - \phi + \theta_w) \tag{8}$$

20

that is to say, it is increased by the difference in Archimedes' force exerted upon the solid grains before and after pumping. The layers underlying the water table aquifer, where p remains constant, experience a σ_z reduction equal to the σ_c reduction (that is, $\gamma\Delta z(\phi - \theta_w)$) with a resulting small rebound. As the magnitude of the rebound is small, it is discarded in the following calculation. Let's refer to the mid-point between B and C in Figure 13. The stress σ_{z0} before withdrawal is as shown in Equation 9.

$$\sigma_{z0} = (1 - \phi)[\gamma'(d + \Delta z + s_0/2) - \gamma(\Delta z + s_0/2)] + \gamma\theta_w d \tag{9}$$

where:

γ' = specific weight of the solid grains [ML^{-2}T^{-2}]

To obtain Equation 9 we used Equation 3 where σ_c is equal to the geostatic weight of a soil column with height $h = d + \Delta z + s_0/2$, that is, $\sigma_c = \gamma\theta_w d + \gamma'h(1 - \phi) + \gamma\phi(h - d)$, and $p = \gamma(h - d)$. We thus locate the σ_{z0} point in Figure 12a and, by making use of Equation 8, compute the subsidence at a given depth according to Equation 4 as follows.

$$\eta = \frac{\Delta e}{1 + e_0}\left(s_0 + \frac{\Delta z}{2}\right)$$

It is easier to visualize the relationship between compaction and void ratio using an abstract version of Figure 2 in which all solids are grouped with no pore space and all pore space occupies the remainder of the volume, with example values assigned and calculations carried out, as explained in Box 2⤵. Box 2 also provides a worked example of calculating the change in effective stress for a decline in the piezometric level of an unconfined aquifer as shown in Figure 13.

If s_0 is large, we can divide s_0 into a number of sublayers and implement the above calculation for the mid-point of each sublayer ($\Delta\sigma_z$ is the same for each sublayer while σ_{z0} changes).

In summary, the compaction of a phreatic aquifer is shown in Equation 10.

$$\eta = \left(s_0 + \frac{\Delta z}{2}\right)c_b\Delta\sigma_z \tag{10}$$

In Equation 10, c_b is the uniaxial vertical soil compressibility, and $\Delta\sigma_z$ is the change in the effective intergranular stress (Equation 8).

2.3   Pumping from a Single Confined Aquifer

Let Δz be the piezometric decline in the confined aquifer (Figure 14). Since the weight of the overlying soil column does not change, that is, σ_c is constant, there is an equal, albeit of opposite sign, change in the effective intergranular stress and the pore pressure, that is, $\Delta\sigma_z = p = \gamma\Delta z$. Computing σ_c at the mid-point of the aquifer as the sum of the stress σ'_c at the bottom of the overlying aquitard plus the weight of aquifer column down to the mid-point results in:

$$\sigma_c = \sigma_c' + 0.5s_0[(1-\phi)\gamma' + \phi\gamma]$$

thus, the intergranular stress is shown by Equation 11.

$$\sigma_{z0} = \sigma_c' + 0.5s_0[(1-\phi)\gamma' + \gamma\phi] - p \tag{11}$$

where:

σ_c' = geostatic stress at the bottom of the overlying impermeable layer

p = pore pressure measured on the mid-plane of the aquifer prior to the piezometric decline [$ML^{-1}T^{-2}$]
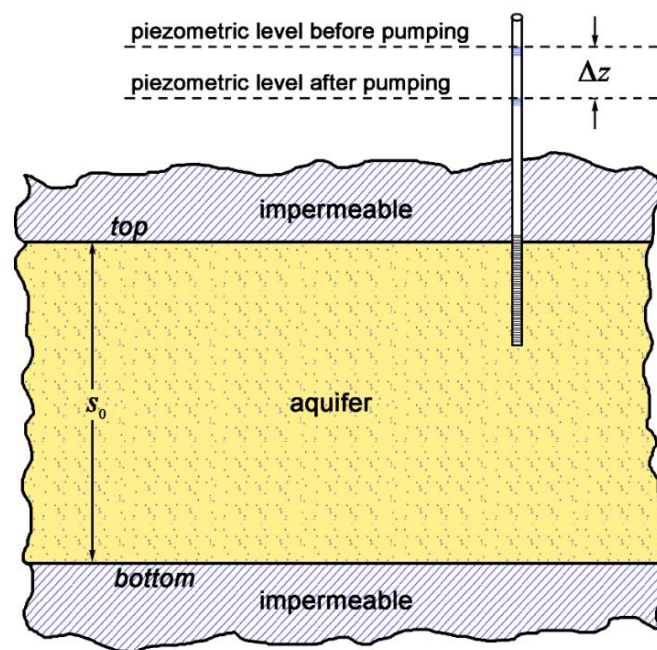
Figure 14 - Sketch of a pumped confined aquifer.

Land subsidence is equal to the aquifer compaction as calculated by the use of a graph as shown in Figure 12 and Equation 3. Again, if s_0 is large, it can be split into sub-intervals and σ_{z0} computed for each sub-interval (while $\Delta\sigma_z$ is the same for each sub-interval).

In summary, the compaction of a single confined aquifer amounts to (Equation 12):

$$\eta = s_0 c_b \Delta\sigma_z \tag{12}$$

with s_0 the aquifer thickness, c_b is the uniaxial vertical soil compressibility, and $\Delta\sigma_z$ is the change in the effective intergranular stress.

2.4   Pumping from a Multi-aquifer System

Let's consider an example of a complex multi aquifer system composed by an unconfined and two confined aquifers (Figure 15). Denote by Δz_1, Δz_2, and Δz_3, the piezometric decline in the three pervious formations, respectively. Land settlement η_1 caused by the depressurization of the unconfined aquifer is computed as is described in Section 2.2. As far as the two confined aquifers are concerned, we have to take into account the decrease of the total geostatic stress equal to $\Delta z_1 \gamma (\phi_f - \theta_w)$, with ϕ_f the porosity of the water table aquifer. As a result, σ_z increases for formations 2 and 3 (Figure 15), respectively:

$$\Delta \sigma_2 = \Delta z_2 \gamma - \Delta z_1 \gamma (\phi_f - \theta_w)$$
$$\Delta \sigma_3 = \Delta z_3 \gamma - \Delta z_1 \gamma (\phi_f - \theta_w)$$

The compactions η_2 and η_3 of the confined aquifers are obtained from Equation 4 and Figure 12 where the representative effective stress prior to pumping is calculated by the use of formulae similar to Equation 11. The subsidence η at the ground surface is then represented by Equation 13.

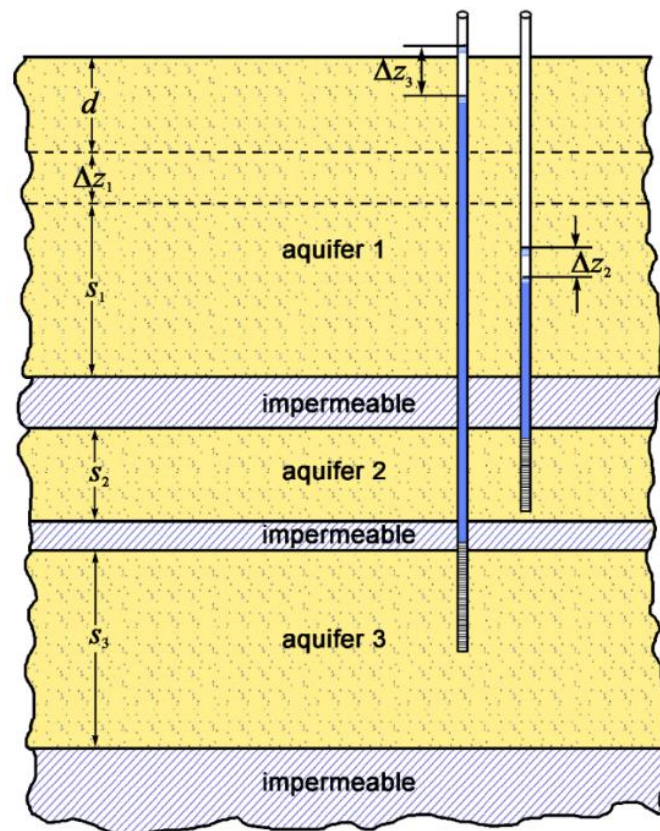$$\eta = \eta_1 + \eta_2 + \eta_3 \tag{13}$$

Figure 15 - Sketch of a pumped multi-aquifer system.

2.5   Delayed Compaction of Aquitards (Confining Beds)

An aquitard (or confining bed) is a clayey-silty low permeability formation that does not provide an appreciable quantity of groundwater to pumping wells; however, it can transmit appreciable water to adjacent aquifers. While flow in an aquifer is predominantly two-dimensional (2-D) and horizontal, particularly if wellbores are fully penetrating, flow in the aquitards separating the aquifers is mostly 1-D and vertical. In a complex aquifer system (for example, Figure 16) the role played by the intervening aquitards is important as they can represent a significant source of water to the aquifers and can contribute greatly to land subsidence as clay/silt compressibility c_b is usually much larger than that of the sand/gravel.
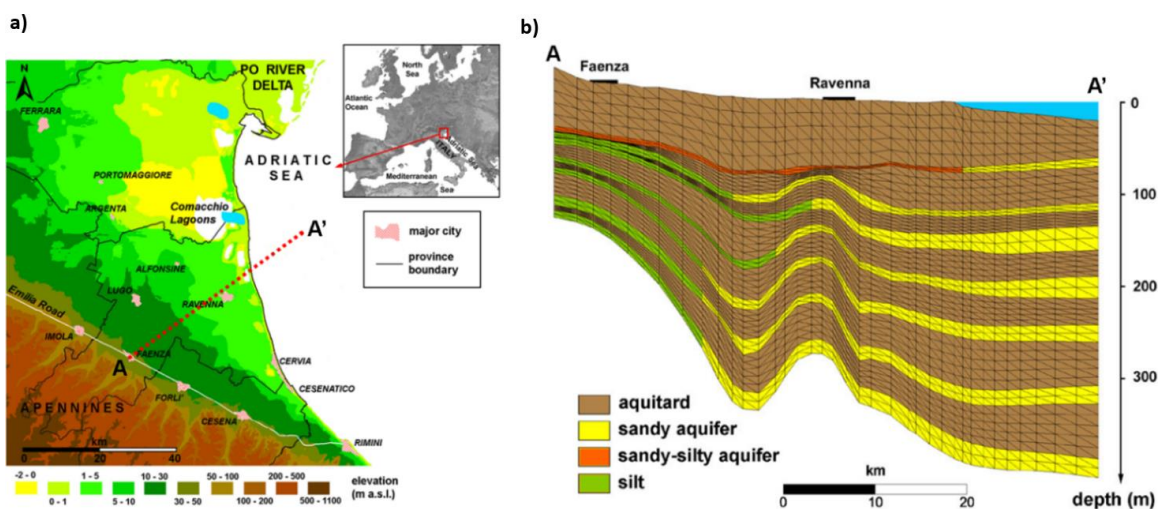
Figure 16 - a) Digital elevation model of the Emilia-Romagna plain, Italy, and b) vertical cross section along the A-A' alignment shown in (a) of the complex multi-aquifer system used to supply freshwater to the coastland (modified after Teatini et al., 2006).

Normally aquitard compaction is larger and delayed in time relative to aquifer compaction. The law that governs pore-water decline in the aquitard as a function of time and the factors controlling compaction are explained in this section. Darcy's law describing the velocity of groundwater flow in an aquitard can be written as shown in Equation 14.

$$v_z = -K \frac{\partial h}{\partial z} \tag{14}$$

where:

$$v_z \;=\; \text{apparent seepage velocity [LT}^{-1}\text{]}$$

$$K \;=\; \text{hydraulic conductivity [LT}^{-1}\text{]}$$

$$h \;=\; \text{hydraulic head} = z + p/\gamma \text{ [L]}$$

$$z \;=\; \text{vertical coordinate positive downward [L]}$$

$$\partial h/\partial z \;=\; \text{vertical hydraulic gradient [LL}^{-1}\text{]}$$

The hydraulic conductivity is a function of the physical properties of fluid and soil as shown in Equation 15.

24

$$K = k^* \frac{\gamma}{\mu} \tag{15}$$

where:

k^* = intrinsic permeability [L^2]

γ = specific weight of water [ML^{-2}T^{-2}]

μ = dynamic viscosity of water [ML^{-1}T^{-1}]

Intrinsic permeability is dependent exclusively on the properties of the medium:

$$k^* = CD^2$$

where:

D = a representative length of the porous medium
(for example, the average grain size)

C = appropriate parameter related to the soil type

Other more complex relationships (depending on porosity, mean pore diameter, and specific surface area) have been developed for intrinsic permeability of reactive clays, especially if salt is dissolved into the pore water (for example, Raffensperger and Ferrell Jr., 1991).

Assume the initial conditions are in equilibrium, and all the hydrologic and geomechanical quantities presented here are incremental with respect to the initial conditions. Let's balance the weight of water in an elementary soil sample of initial length Δz and unitary cross-sectional area (shown as 1 in the expressions below) between time t and $t + \Delta t$:

- Inflow: (γv_z) (1) (Δt)
- Outflow: $\gamma(v_z + \partial v_z/\partial z\ \Delta z)$ (1) (Δt)
- Weight of water expelled by the porous space contraction and the expansion of the water expressed by Equation 16 (we assume incompressible solid grains the total medium volume change coincides with the porous volume change):

$$-[(\gamma\Delta(\phi\Delta z)\ 1\ \Delta p) + (\gamma\phi\beta\ 1\ \Delta p)] \tag{16}$$

where:

β = volumetric compressibility of water (ML^{-1}T^{-2})

In Equation 16 the total geostatic stress σ_c is assumed to be constant, so (from Equation 3):

$$\Delta\sigma_z = -\Delta p$$

The change in pressure, Δp, is negative when p is reduced, as happens during groundwater pumping. Notice that $\Delta(\phi\Delta z)$ is equal to $\Delta\{[e/(1 + e)]\Delta z\}$ with $\Delta z/(1 + e)$ constant because this is the solid part (grains) of the elementary volume (1) Δz. Hence (from Equation 5) we have:

$$\frac{\Delta e}{1 + e} = c_b\Delta p$$

and therefore, we obtain:

25

- Outflow – Inflow = Weight of water expelled, i.e.

$$\gamma \frac{\partial v_z}{\partial z} \Delta z \Delta t = -\gamma(c_b + \phi\beta)\Delta z \Delta p$$

Cancelling γ and Δz on both sides and remembering that the hydraulic head $h = z + p/\gamma$, we know that $\Delta p = \gamma\Delta h$, and using Equation 14 when the increment of time approaches zero $\Delta t \to 0$ we obtain Equation 17:

$$\frac{\partial}{\partial z}\left(K\frac{\partial h}{\partial z}\right) = \gamma(c_b + \phi\beta)\frac{\partial h}{\partial t} \qquad (17)$$

Solving Equation 17, complemented with the appropriate top and bottom boundary conditions and initial conditions, provides the pressure dissipation within the aquitard, and hence the Δp needed to compute the aquitard compaction versus time. The specific storage coefficient is defined in Equation 18.

$$S_s = \gamma(c_b + \phi\beta) \qquad (18)$$

S_s represents the "*specific elastic storage*" [L⁻¹] and along with the hydraulic conductivity, K, defines Terzaghi's consolidation coefficient c_v that controls both magnitude and timing of aquitard compaction as shown in Equation 19 given that $\phi\beta << cb$ for typical aquifer confining beds.

$$c_v = \frac{K}{\gamma(c_b + \phi\beta)} \approx \frac{K}{\gamma c_b} \qquad (19)$$

The initial conditions correspond to $\Delta p = 0$ for the entire thickness, b, of the aquitard while the boundary conditions are given by Δp in the overlying and underlying aquifers. If the pressure drop Δp_0 is the same at top $(z = 0)$ and bottom $(z = b)$, then pressure conditions are symmetrical above and below the middle of the aquitard, hence $\frac{\partial p}{\partial z} = 0$ at $z = b/2$. In this case, the solution to Equation 17 can be expressed in terms of a series expansion. Writing the solution in terms of p produces Equation 20.

$$p = p_0 - \frac{4}{\pi}\Delta p_0\left[\frac{\pi}{4} - \frac{\sin(\pi z/b)}{\exp^{(\pi/b)^2 c_v t}} - \frac{1}{3}\frac{\sin(3\pi z/b)}{\exp^{(3\pi/b)^2 c_v t}} - \cdots\right] \qquad (20)$$

where:

z = vertical coordinate positive downward starting from the aquitard top $(0 \le z \le b/2)$

t = time since the initial change in pressure at the aquitard boundary

For $t = 0$, and setting $\pi z/b = x$ $(0 \le x \le \pi/2)$ Equation 20 becomes Equation 21.

$$p(z,0) = p_0(z) - \frac{4}{\pi}\Delta p_0\left[\frac{\pi}{4} - \left(\sin x + \frac{1}{3}\sin 3x + \frac{1}{5}\sin 5x + \cdots\right)\right] \qquad (21)$$

The content within the parentheses of Equation 21 is the Fourier series development of the function $f(x)$:

$$f(x) = \begin{cases} \pi/4 & \text{for } 0 \le x < \pi \\ -\pi/4 & \text{for } \pi < x \le 2\pi \end{cases}$$

Keeping in mind the range of variability of $x\,(0 \le x \le \pi/2)$ we conclude that Equation 20 accurately represents the initial pore pressure at time $t = 0$.

2.6   Time Factor and Compaction Profile

The (positive) compaction $\eta(t)$ of the half aquitard at time t is:

$$\eta(t) = \int_0^{b/2} c_b(p_0 - p)\ dz$$

Substituting Equation 20, and integrating term by term leads to Equation 22.

$$\eta(t) = \frac{4}{\pi^2} c_b \Delta p_0 b \sum_{n=0}^{\infty} \frac{1}{(2n+1)^2} \left\{ 1 - \frac{1}{\exp^{[(2n+1)\pi/b]^2 c_v t}} \right\} \tag{22}$$

For $t = 0$ we get $\eta(0) = 0$, while for $t = \infty$ Equation 22 becomes Equation 23.

$$\eta(\infty) = \frac{4}{\pi^2} c_b \Delta p_0 b \left(1 + \frac{1}{3^2} + \frac{1}{5^2} + \frac{1}{7^2} + \dots \right) \tag{23}$$

The above series converges to $\pi^2/8$ and therefore $\eta(\infty)$ is the ultimate compaction of the half aquitard, as was already pointed out for the various aquifers represented by Equations 4 and 5 and is expressed here as Equation 24.

$$\eta(\infty) = c_b \Delta p_0 \frac{b}{2} \tag{24}$$

It may be interesting to compute the time needed by the aquitard to achieve a given percentage of full compaction, $\eta(\infty)$, provided by Equation 24. To this aim we introduce the dimensionless time factor T_v (Equation 25) as defined by Terzaghi (1923).

$$T_v = 4 \frac{c_v t}{b^2} \tag{25}$$

Denoting the percentage compaction as w, Equation 26 shows that it is a function of only T_v.

$$w(T_v) = \frac{8}{\pi^2} \sum_{n=0}^{\infty} \frac{1}{(2n+1)^2} \left\{ 1 - \frac{1}{\exp^{[\pi^2(2n+1)^2 T_v/4]}} \right\} \tag{26}$$

The behavior of $w(T_v)$ is shown in Figure 17. There are basically two ways to use Figure 17:

- enter Figure 17 with a given percent of the final compaction, to obtain the corresponding T_v and calculate the time t needed to reach that percentage from Equation 25; or,
- select a time t, compute T_v from Equation 25 and derive the percentage compaction from Figure 17.

The compaction of the aquitard at time t is shown as Equation 27.

$$\eta(t) = 2w(T_v) \; \eta(\infty) = w(T_v) \; c_b \Delta p_0 b \tag{27}$$
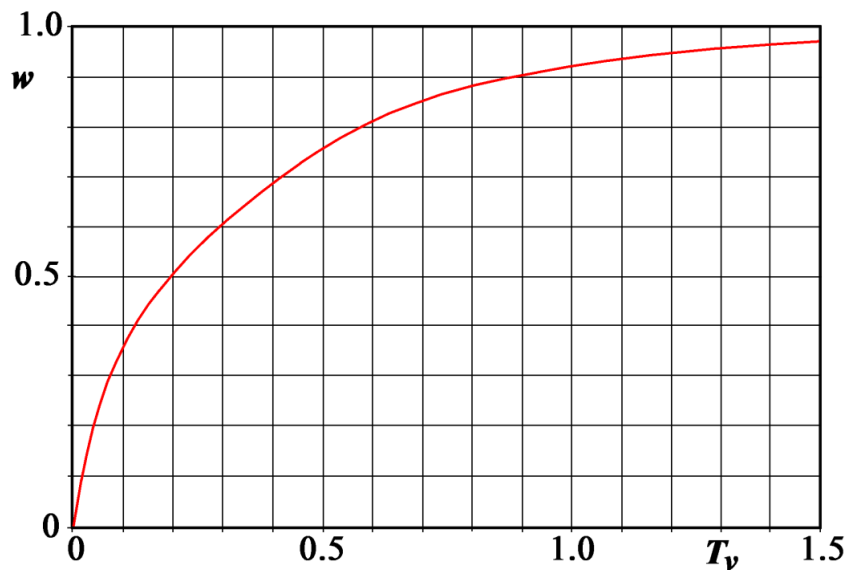
Figure 17 - Behavior of the aquitard compaction $\eta(t)$ relative to the ultimate compaction $\eta(\infty)$, $c_b \Delta p_0 b$ versus time factor T_v.

Figure 17 is also helpful to compute the compaction of an aquitard that is in contact with a non-productive aquifer, for example, with $\Delta p_0 = 0$ at the aquitard bottom. In fact, notice that because of the linearity of Equation 17 and, with Δp_0 equal on both aquitard top and aquitard bottom, we can superpose the effects, namely we can separately compute the compaction of the aquitard subject to $\Delta p_0 \neq 0$ on top and $\Delta p_0 = 0$ on bottom and vice versa $\Delta p_0 = 0$ on top and $\Delta p_0 \neq 0$ on bottom. The Δp behavior versus z for various time values is shown in Figure 18 from right and left respectively.

28
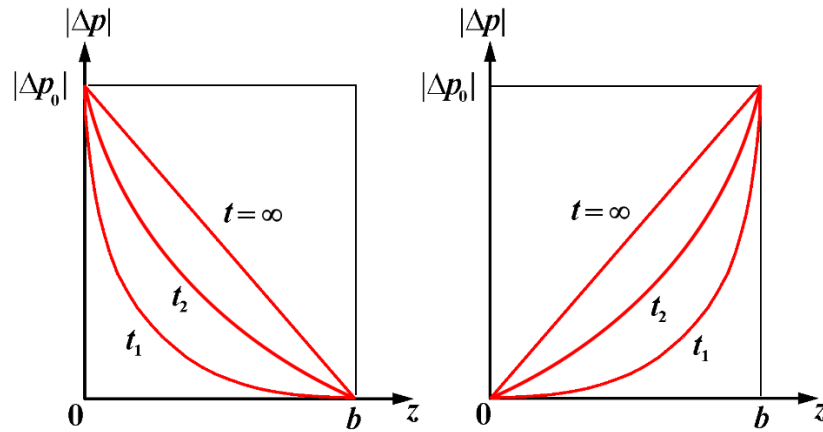
Figure 18 - Schematic behavior of the pore pressure decline in an aquitard subject to an instantaneous pore pressure drop Δp_0 on top ($z = 0$, left) and bottom ($z = b$, right) for representative time values.

The area underlying a Δp_0 profile at any given time, for instance t_1, is the same on the left and right images of Figure 18. Such an area, however, is proportional to the compaction of the aquitard subject to $\Delta p_0 \neq 0$ on both top and bottom, that is, half the value $\eta(t)$ provided by Equation 22. In summary, if one of the adjacent aquifers is not pumped the aquitard compaction is given by Equations 22 and 24 at current time t and $t = \infty$ respectively. We can use the graph of Figure 17 as explained earlier with the percent compaction relative to the final compaction described by Equation 24.

A straightforward generalization is the implementation of the previous outcome to the case where aquifers top and bottom experience different pore pressure drops, that is, $\Delta p_1 \neq \Delta p_2$. The ultimate aquitard compaction is given by Equation 28.

$$\eta(\infty) = \frac{1}{2} (\Delta p_1 + \Delta p_2) \, c_b \, b \qquad (28)$$

Figure 17 may be used as described above along with the percentage relative to $\eta(\infty)$ of Equation 26. In case for which the pore pressure drops Δp_1 and Δp_2 on top and bottom of the aquitard are a continuous function of time, they can be approximated with stepwise functions with the effects of the incremental drops superposed at the corresponding times.

3   Measuring and Monitoring Subsidence and Compaction

The analysis and prediction of expected anthropogenic land subsidence due to fluid pumping require a careful reconnaissance study of the area of interest, with a detailed layout of the basin's geology and geometry and reconstruction of the pumping rate evolution, pressure head, and displacements of the land surface. Geomechanical and hydraulic properties are of the utmost importance. Pre-consolidation stress; zones of overpressure; and the presence of faults and thrusts along with their extent, orientation and geomechanical properties (that is, friction angle and cohesion) must all be reliably

29

identified. Advanced technology such as 2-D and 3-D seismic surveys, airborne-electromagnetic investigations, well-logs, exploration boreholes, pumping tests, and specific laboratory analyses can be of great value. Much progress has been made, since the traditional spirit leveling, in accurately monitoring ground surface movements. New techniques include Global Navigation Satellite Systems (GNSS) and Interferometric Synthetic Aperture Radar (InSAR) by which land subsidence is measured from space with high accuracy. Advances have also been accomplished in measuring shallow and deep aquifer system compaction by single-level cable and multi-level magnetic borehole extensometers.

Anthropogenic land subsidence modeling and forecasting tools are continuously improved. They take advantage of both enhanced computer devices (for example, parallel hardware) and advanced measurements technology applied to horizontal and vertical ground movements (for example, Differential Global Positioning System (DGPS) and InSAR technologies). Modeling tools are helpful in determining and distinguishing among multiple causes, and can be effectively combined with measurement techniques. Once the models have been calibrated to the observed history of the aquifer, they can be used in their predictive capacity to evaluate various future scenarios of groundwater use. They can be used to develop integrated resource management programs that should take environmental and socio-economic impacts into account. The models are used to evaluate the adverse consequences of fluid extraction in a medium/long time range, in particular for urban flood management of coastal areas and in other cases of environmental vulnerability. The following sections present methods used to measure land subsidence.

3.1   Spirit Leveling

Spirit (differential) leveling is the traditional method of determining ground elevation changes and, despite its simplicity, can be very accurate. Equipment and procedures are described in detail in several manuals, for example, in Rappleye (1948) and Floyd (1978). The technique was developed in the nineteenth century and continues to be applied. The method allows surveyors to carry an elevation from a known reference point to other geodetic marks using a precisely leveled telescope and a pair of graduated vertical rods. For each survey, the elevation difference, e_d, between two benchmarks is recorded twice by accumulating the elevation differences between a series of temporary turning points. The method assumes the stability of the reference benchmark, thus special care must be taken in tectonically active zones. The discrepancy between e_d measured in the forward and backward directions (relative to the direction of the traverse) must not exceed $1.5\sqrt{D}$ mm for a "very high (first order)" precision survey, and $3\sqrt{D}$ mm for a "high (second order)" precision survey, D being the length of the benchmark line in kilometers. Typically, benchmarks are spaced 1 km apart and turning points are 20 to 100 m apart. Once a network of benchmarks has been established and surveyed by precise leveling, a further survey at some later date shows whether vertical movements have occurred (Figure 19).
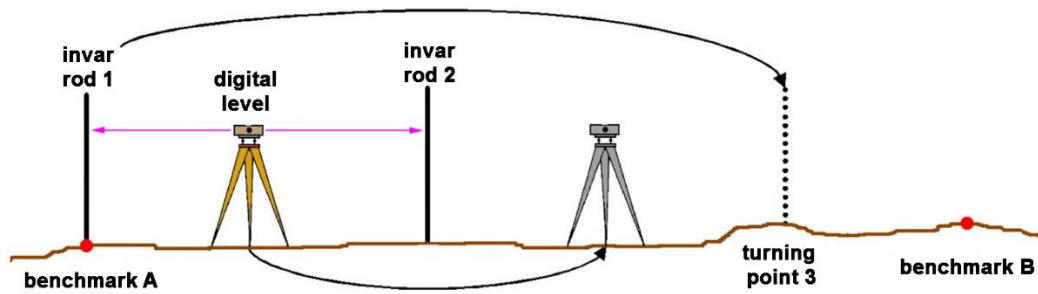
Figure 19 - Sketch of a leveling survey.

Digital levels and invar rods (invar is an alloy of iron and nickel with a negligible coefficient of expansion) help fulfill the selected accuracy, eliminating the human errors and increasing the measurement speed. To ensure long-term time series, the benchmarks, a brass cup or headed bolt, are grouted into massive structures, such as bridge abutments, bedrock outcrops, or attached at the top of a 5 to 10 m long bar driven into the ground and protected by an outer sleeve. Examples of leveling networks established to control land subsidence due to fluid withdrawal are published by Ikehara and others (1997) and Tosi and others (2007).

3.2   Global Navigation Satellite Systems

Developed in the early 1970s and fully operational for civil uses since the mid-1990s, Global Navigation Satellite Systems (GNSS) have been widely used to monitor land movements occurring over large areas caused by earthquakes, tectonic plate motion, and plate boundary deformation. These systems include the United States Global Positioning System, GPS; the Russian Global Navigation Satellite System, GLONASS; and the European Galileo global navigation satellite system. These systems, generally, although wrongly termed "GPS", consist of earth-orbiting satellites producing radio signals that can be used to obtain accurate land surface positions. GPS has been operational since 1995 with a constellation of 24 satellites at an average orbit altitude of about 20,000 km, arranged in six orbital planes inclined 55° relative to Earth's equator. As of October 2017, there were a total of 31 operational satellites in the GPS constellation.

The signals from at least four satellites can be used by an autonomous receiver anywhere on or near the Earth to determine its approximate absolute (that is, non-differential) position. High precision measurements of crustal movements can be made with differential GNSS by finding the relative displacement between GNSS receivers. Multiple stations situated around an actively deforming area (such as a volcano or fault zone) are used to determine strain and ground movement. Over the last decade, a large number of GNSS tracking stations have been established worldwide. These large over-national and over-continental networks are managed by different institutions and consortiums (for example, SOPAC (sopac.ucsd.edu/index.shtml↗), UNAVCO (www.unavco.org↗), and EUREF (www.epncb.oma.be↗)).

31

GNSS observations collected simultaneously at two receivers (one receiver may be a continuous global positioning system) are used to compute a precise baseline between the receivers. Given the known location of the Continuous GNSS (or base station), the 3-D position of the roving receiver is determined by adding the observed baseline vector to the known position. Therefore, geodetic networks of reference marks have been established in subsiding zones. They are surveyed and resurveyed by portable GNSS receivers that are temporary placed on the marks, and used as a reference for one or more continuous GNSS stations (C-GNSS station) located in the area. An example is provided for the Venice region of Italy in Figure 20. One of the first such networks was designed specifically to monitor land subsidence caused by groundwater extraction was established in the Antelope Valley, Mojave Desert, California, USA in 1992 (Ikehara and Phillips, 1994).
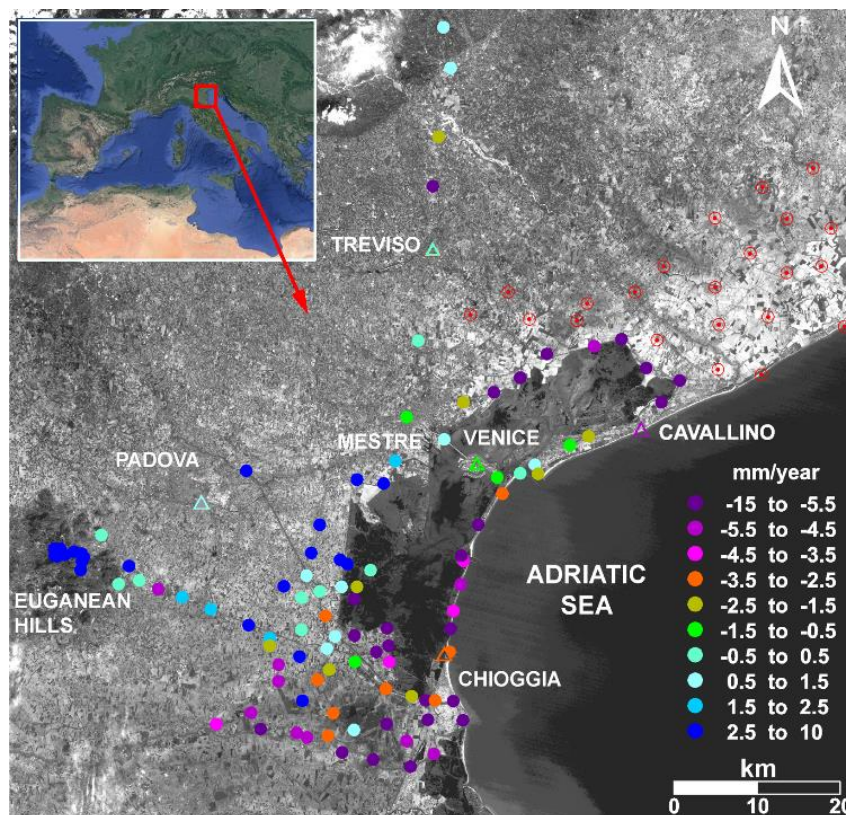
Figure 20 - LANDSAT image of the Venice region (Italy) with the GNSS (circles) and C-GNSS (triangles) networks. Colors are representative of the displacement rates (mm/year) measured between 1999 and 2003. New GNSS benchmarks added to the network in 2004 are indicated with open red circles (after Teatini et al., 2005).

3.3   InSAR

Many scientific papers have been published over the last two decades on the topic of interferometric Synthetic Aperture Radar (SAR)-based methodologies for measuring displacements in the earth surface, in particular, land movements due to groundwater pumping (for example, Amelung et al., 1999; Hoffmann et al., 2001; Buckley et al., 2003; Hoffmann et al., 2003; Galloway and Hoffmann, 2007; Bell et al., 2008; Higgins et al., 2014; Tosi et al., 2016; Da Lio et al., 2018). The most well-known and widely used SAR

32

processing-chains among a continuously increasing variety of algorithms include: Differential SAR Interferometry - DInSAR (Gabriel et al., 1989), Permanent Scatterer InSAR - PSInSAR (Ferretti et al., 2001), Small Baseline Subset - SBAS (Berardino et al., 2002), Interferometric Point Target Analysis - IPTA (Wegmuller et al., 2004), and ''Squeezed'' SAR - SqueeSAR (Ferretti et al., 2011).

SAR-based techniques exploit the phase difference of the radar signals between or among a number (at least two) of satellite acquisitions over the same area. The phase difference is strictly related to the earth surface displacement occurring between the acquisitions once the surface topography contribution is removed and the atmospheric disturbance mitigated. SAR-based methodologies allow for the detection and measurement of sub-centimeter-scale ground movement with high spatial detail and high measurement resolution. Several SAR-borne satellites have been in operation from 1991 to the present (ERS-1/2; ENVISAT; JERS-1; Radarsat-1/2, ALOS, TerraSAR-X, Cosmo-SkyMed) and SENTINEL-1 has been in operation since mid-2014, thus a large satellite SAR data archive exists over many areas. Figure 21 shows two significant examples of SAR-derived land subsidence.
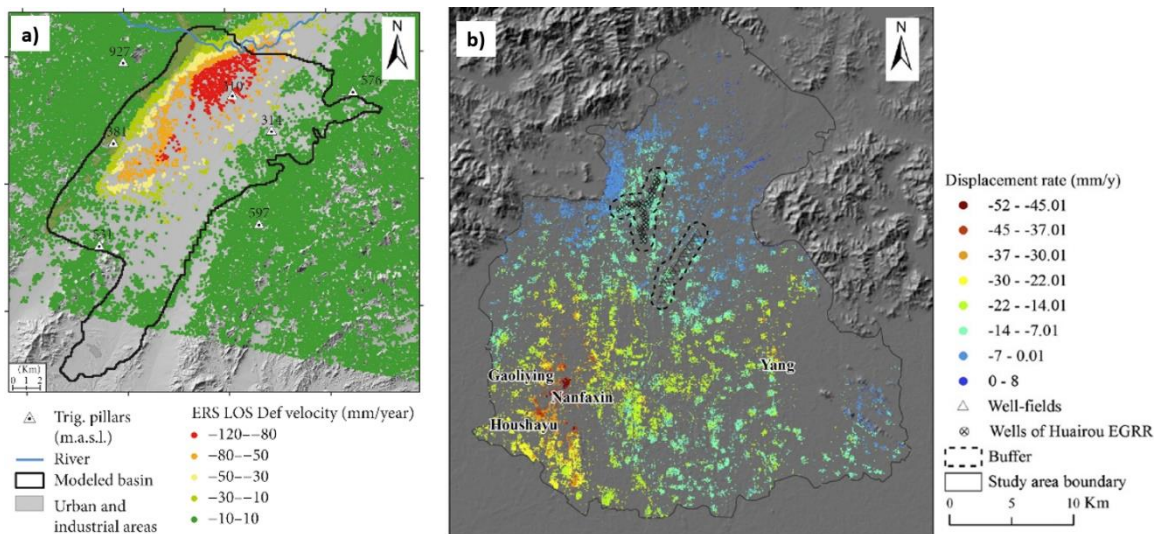
Figure 21 - a) Alto Guadalentín Aquifer (SE Spain): LOS deformation velocities from ERS data (C-band, 1992–2000) (modified after Ezquerro et al., 2017). b) Northern Beijing plain, China: average displacement rate detected by IPTA from June 2003 to January 2010. Negative values mean land subsidence, positive values mean uplift (modified after Zhu et al., 2015).

As in the case of leveling, SAR-based data are differential measurements, that is, displacements relative to a reference point. Therefore, the movement of the reference point has to be known, for example, from previous leveling or permanent GPS stations, in order to calibrate the SAR results and obtain "absolute" displacements. SAR-based measurements are 1-D measurements related to the projection along the satellite Line-Of-Sight (LOS) of the 3-D displacement vector affecting the radar target. Given that the radar viewing angle is less than 45° from the vertical, the SAR outcome is most sensitive to vertical motion. However, the combination of the Earth's rotation and satellite motion makes it possible for

any area of interest to be illuminated by the satellite radar sensor along two different acquisition geometries: one having the satellite flying from south to north, known as "ascending mode" and the other from north to south called "descending mode" as portrayed in Figure 22.
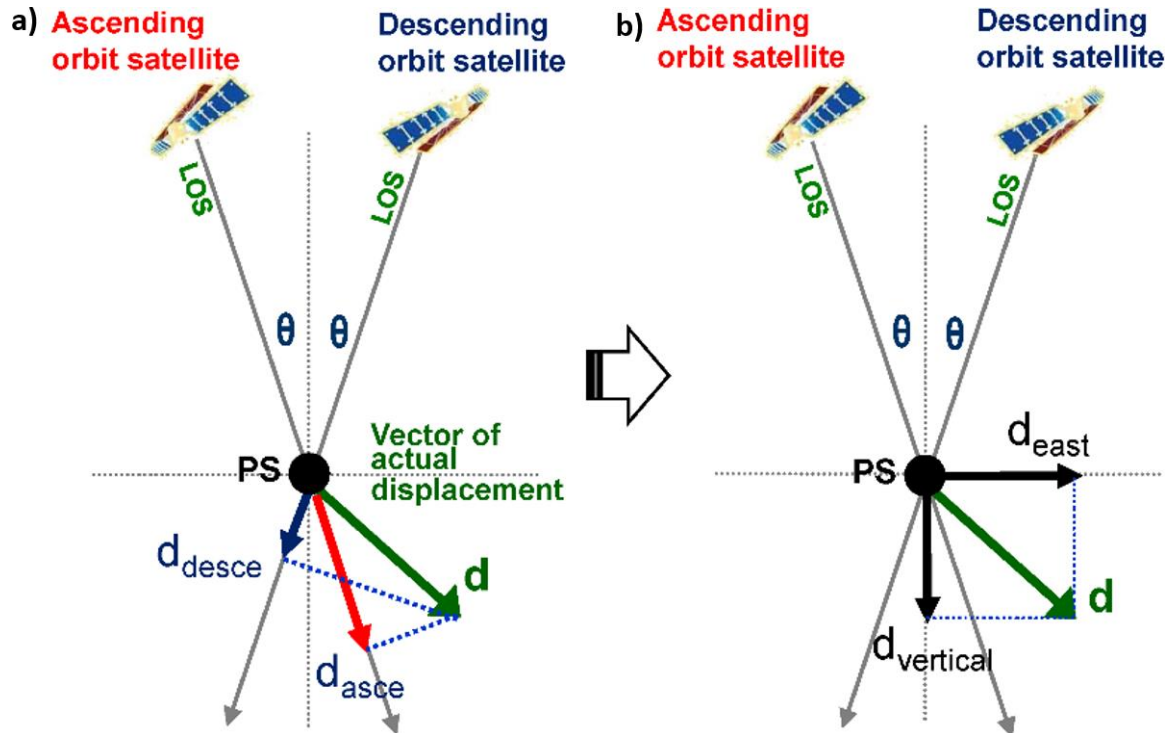
Figure 22 - The satellite SAR imaging geometry along the ascending and descending orbits and the projection relation between the LOS displacements and the 3-D motion components. The a) combination of movement components along the ascending (d_{asce}) and descending (d_{desce}) LOS directions allows for quantification of actual displacements (d) and, consequently; b) displacement components along both vertical ($d_{vertical}$) and west-east (d_{east}) directions.

Whenever two data sets of SAR images are available, acquired over the same area and during the same time frame along ascending and descending orbits, the SAR results can be used successfully to estimate two components of the local displacement, that is, the vertical ($d_{vertical}$) and the west-east (d_{east}) components, thus significantly improving our understanding of the event under study as illustrated for the Phoenix, Arizona, USA area in Figure 23. The following system of equations can be used to make the determinations (Pepe and Calò, 2017).

$$\begin{bmatrix} d_{vertical} \\ d_{east} \end{bmatrix} = \begin{bmatrix} \dfrac{d_{asce} - d_{desce}}{2\sin\theta} \\ \dfrac{d_{asce} + d_{desce}}{2\cos\theta} \end{bmatrix}$$
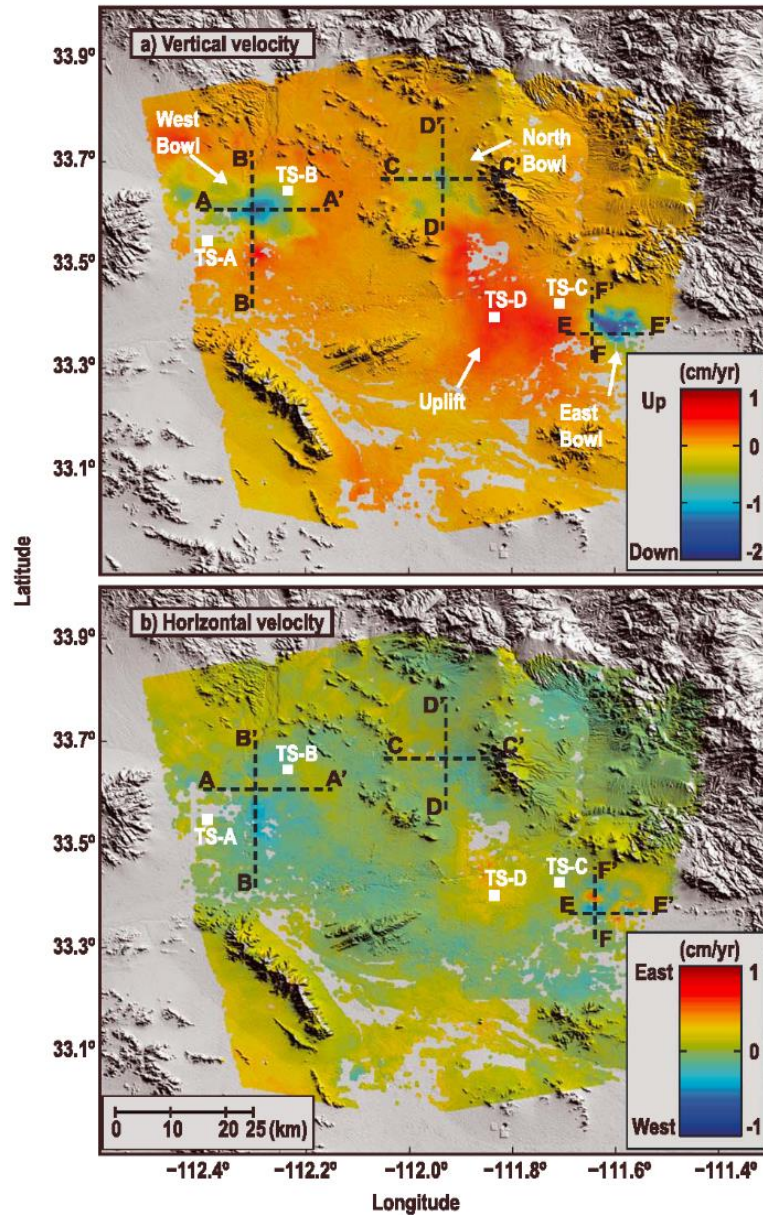
Figure 23 – In the Phoenix, Arizona, USA metropolitan area: a) vertical and b) horizontal velocity maps from ENVISAT ascending and descending combined data sets (modified from Miller and Shirzaei, 2015).

SAR processing-chains can provide millions of data points over a large region (1×10^4 to 1×10^5 points per km²) and are often less expensive than sparse point measurements from "traditional" labor-intensive spirit-leveling and costly C-GPS stations. Moreover, SAR results have shown that land displacements due to groundwater withdrawal and injection are characterized by a spatial variability almost impossible to detect by other surveying techniques. For these reasons, leveling and GPS have been used less and less over recent years to measure land subsidence. However, we emphasize that they remain of paramount importance in calibrating the SAR outcome as described above, and are essential in providing measurements over natural terrain, densely vegetated zones,

35

or farmlands where the SAR signal loses coherence and the interferometric algorithm cannot be applied.

3.4   Borehole Extensometer

Continuous measurements of soil deformation in a (normally small) number of locations in a subsiding area have been carried out using borehole extensometers. They are used to measure the change in the distance between the land surface and a subsurface benchmark situated at the bottom of a deep borehole. If the subsurface benchmark is established below the base of the compacting aquifer system or in the bedrock, the extensometer can be used as the stable reference for local geodetic surveys. The first borehole extensometer was installed in 1955 by the United States Geological Survey in the San Joaquin Valley, California, USA (Poland, 1984). Since then, extensometer technology has seen progressive improvement, playing an important role in relating land subsidence to the compaction of confined aquifer systems.

Several types of early borehole extensometers are reviewed by Poland (1984). Recently, anchored cable counterweighted extensometers and slip-joint casing extensometers have been widely used. The measuring devices are schematically shown in Figures 24a and 24b. A typical cable counterweighted extensometer tool consists of a balance beam carrying a cable or a pipe, which is fastened at one end to an anchor weight located at the bottom of the compacting system, and at the other end to a counterweight keeping the cable at a constant tension (Figure 24a). To build up a sliding-joint casing extensometer, a hole is drilled to a depth where rock is stable. The hole is then lined with a steel casing with slip-joints to prevent crumpling as subsidence occurs. An inner pipe rests on a concrete plug at the bottom of the borehole and extends to the top. This inner pipe then transfers the stable elevation to the surface. Measurement of the distance from the inner pipe to the surrounding land surface provides the amount of compaction that has occurred over a given time interval (Figure 24b). A computer-controlled system records the compaction data against time. The instrumental precision heavily depends on the actual extensometer implementation, but a nominal deformation resolution of 0.01-0.1 mm can be achieved over a 200-1000 m depth (Riley, 1986).

In the case of multi-aquifer systems, extensometer stations are composed of close multiple-borehole extensometers installed at different depths, so as to derive the deformation of each single formation by subtracting the records acquired at various depths. A recent alternative to multiple- extensometer stations are multiple-position borehole extensometers that incorporate a number of independent markers anchored to the formation borehole at different depths (Figure 24c). Magnetic markers have been used in Taiwan (Hwang et al., 2008; Hung et al., 2012) to compute vertical compaction in boreholes using repeat borehole logging with magnetic sensors on calibrated lines or tapes in order to measure temporal changes in marker positions. This method is capable of monitoring

36

from ten to several tens of marker positions in a single borehole at measurement resolutions of about 1-2 mm over a depth of several hundred meters.
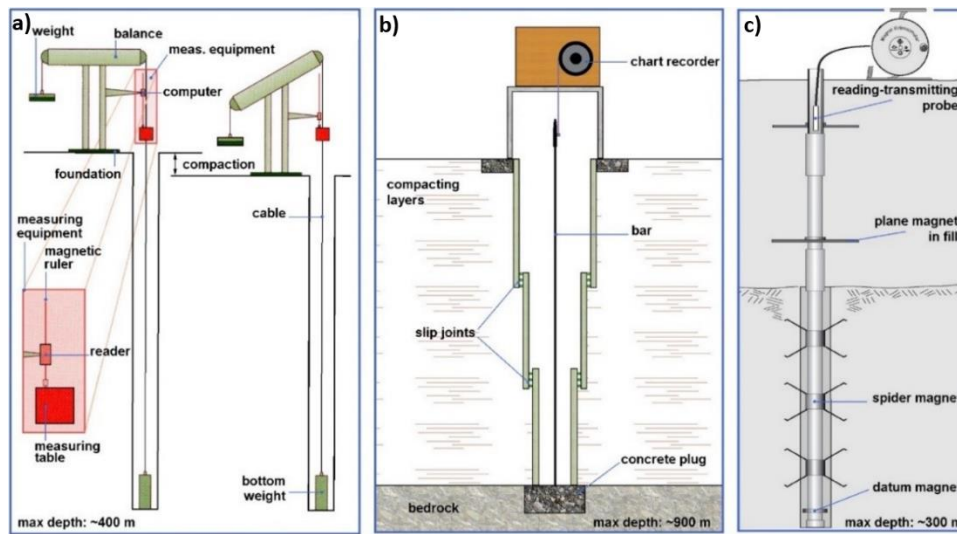

Figure 24 - Schematic representation of a) a single-layer cable extensometer; b) a slip-joint casing extensometer; and, c) a multilayer magnetic borehole extensometer used to record the deformation of aquifer-aquitard systems.

A relatively dense network of extensometer stations has been established in metropolitan areas experiencing significant land subsidence. Two major examples are Houston, Texas, USA and Shanghai, China. The Houston-Galveston area is an extreme example of subsidence hazards, a problem that affects many other USA metropolitan areas, for example: Los Angeles, California; Sacramento, California; and New Orleans, Louisiana. Portions of Houston experienced severe settlement, up to 3 m, from 1915 to 2001. The United States Geological Survey has been operating 13 borehole extensometers at 11 sites since 1973 for the purpose of observing compaction of aquifers in the area. The borehole extensometers, which were designed according to the sliding-joint casing type, span a depth down to 936 m (Yu et al., 2014). Shanghai is the first city in China where land subsidence was investigated and monitored, being one of the country's most densely populated and developed areas. The maximum cumulative land subsidence was 2.6 m in 2002 and the total area of land subsidence was about 5000 km^2 in 2006. A number of the 27 extensometer groups have been used since the 1960s to monitor compaction of individual aquifers and aquitards to a depth of approximately 350 m (Wu et al., 2010).

Horizontal extensometers were used to measure differential horizontal ground motion at earth fissures caused by changes in groundwater levels in South-Central Arizona, USA (Carpenter, 1993). Buried horizontal extensometers made of quartz tubes or invar wires were used to precisely and continuously measure fissure opening in a natural environment over a scale of 330 m. Following enlargement of the ground rupture occurrence in several countries worldwide, other specific mechanical and optical instrumentation has recently been developed and used in urban areas such as Iztapalapa,

Mexico City, Mexico (Carreon-Freyre et al., 2010), and Beijing, China (Zhu et al., 2015). These monitoring stations allow one to accurately measure the relative displacements characterizing the rupture in a 1-D (only opening) or 3-D (opening and sliding) reference system as shown in Figure 25.
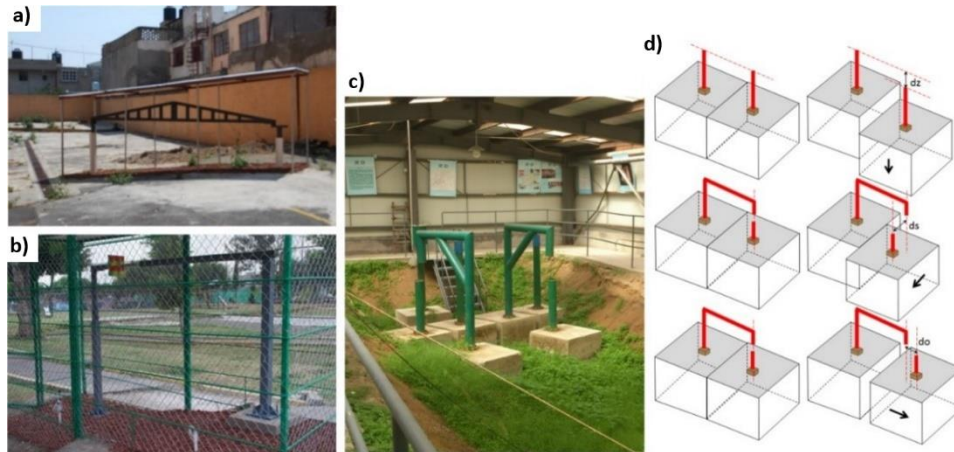

Figure 25 - Some examples of ad hoc instrumentation developed to monitor opening and sliding of earth fissures or faults activated by the overdraft of aquifer resources. a) 1-D apparatus and b) 3-D apparatus established in Iztapalapa, Mexico City, Mexico (courtesy of Dora Carreon-Freyre, Centro de Geociencias, National Autonomous University of Mexico). c) 3-D instrumentation installed in the northern Beijing plain (courtesy of Lin Zhu, Normal Capital University, Beijing, China). d) A sketch showing how 3-D movements can be measured through the apparatus established in the Beijing plain.

3.5   Fiber Optics

Following the development and large use for monitoring civil infrastructures, distributed fiber optic sensors (FOS) have become even more popular in the recent years to perform real-time observations and provide early warning of natural and anthropogenic geo-hazards, such as landslides (Schenato et al., 2017), debris flows, land subsidence (Wu et al., 2015), and earth fissures (Liu et al., 2017). The common assumption that enables the sensing feature in optical fibers is that the surrounding environment affects the local properties of the fiber itself: the back-propagating light generated when an optical signal is fed into the fiber is used to investigate the local properties of the fiber, and therefore to figure out the changes in the surrounding environment. Very simply, local temperature and strain intrinsically influence frequency and intensity of the scattered signal and therefore variations of temperatures, displacements, loads, earth pressures, pore water pressures and soil moistures can be captured with high accuracy. Schenato (2017) and Zhu et al. (2017) provide accurate reviews of the state-of-the-art.

In Japan, a FOS system has been introduced in boreholes to monitor formation compaction accompanying the exploitation of natural gases (Ikeda et al., 2015). Wu et al. (2015) initiated a study on applying FOS to land subsidence monitoring in Suzhou, China, where a complex multi-aquifer system has been over-drafted during recent decades. The fully distributed strain sensing cables were vertically installed in boreholes for

38

displacement monitoring. The borehole was filled with a fine sand-gravel-bentonite mixture after the cables were installed, and no strategies for temperature compensation were adopted. The displacements were calculated based on the axial strain measurements of the cables.

Liu et al. (2017) investigated the feasibility of using fixed-point distributed optical fiber sensor in earth fissure monitoring. To improve the fiber strength, the structure of the cable was made of three layers from the core to the outer coating materials: the bare-optical fiber, a polyurethane coating, and a spiral-shaped metal sheath. Five-centimeter-long sections of cable were further encased into an aluminum alloy tube and placed in a heat-shrinkable tube (10 cm-long) at regular distances. These raised portions of cable were used to anchor the cable to the ground with nails. The distance between anchors was fixed to 2 m after careful consideration, and the cable was pre-stressed during installation. Additional strain-free cables were measured for temperature compensation. The sensor system was successfully used in an earth fissure site in Wuxi, China, where two main ground fissures (with a maximum strain value of 360 $\mu\varepsilon$, that is, 360×10⁻⁶) were detected and measured (Figure 26).
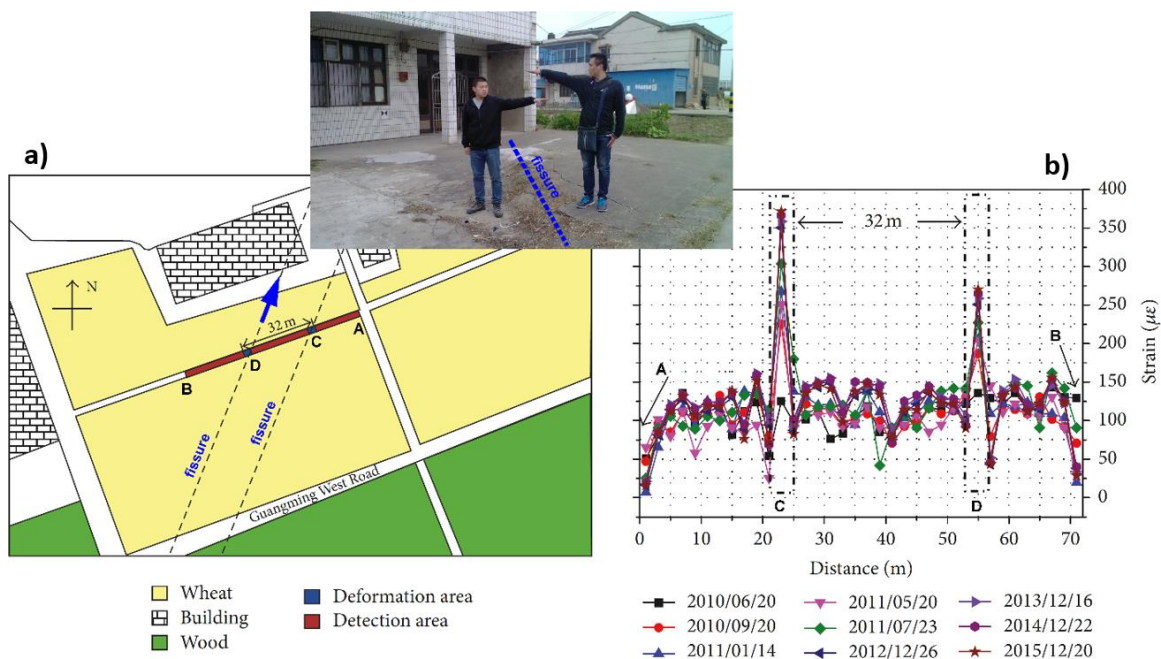
Figure 26 - a) Map with the trace of the earth fissures in Wuxi, China, and the location of the FOS monitoring equipment. The blue arrow represents the orientation of the photo shown in the inset. b) Strain distribution along the cable: the two peaks correspond with the main ground fissures (modified after Liu et al., 2017).

4   Mitigation of Land Subsidence by Water Injection

The simplest, most straightforward action toward mitigating land subsidence caused by fluid withdrawal would seem to be artificial fluid injection. It goes without saying that other strategies can help to prevent land subsidence, including the policy of requiring withdrawal limits, permits, fees, taxes, metering, and enforcement control on

groundwater pumping as exercised by central and local authorities. Freeze (2000) conveys the general recommendation that land subsidence should act as a guiding factor when defining a groundwater exploitation management strategy, along with more traditional factors, such as water table decline, saltwater intrusion, and avoidance of groundwater contamination.

Generally speaking, when land subsidence has occurred and/or is still occurring, methods used to control, mitigate, or arrest it include reduction of pumping rates, artificial aquifer recharge from the land surface, re-pressurization of depleted layers by way of injection wells, creation of a hydraulic barrier to stop advancement of the cone of depression, and generation of an overpressure in geological units unaffected by pumping in order to build a structural obstacle to the migration of in-depth compaction to the ground surface. A combination of any of the above methods can be used as well, consistent with a cost/benefit analysis. An example of conservative mitigation strategy is one whereby the effective stress within the depleted formation does not increase beyond the stress level experienced to date. A more aggressive strategy might dictate a decrease in the effective stress and/or the active involvement of overlying formations through the use of fluid injection. Injecting water into a geological formation generates an increase in pore pressure, a decrease in effective stress, and hence an expansion of the injected formation. Part of the latter may migrate to the ground surface, giving rise to an anthropogenic land rebound and/or uplift.

While anthropogenic land subsidence is a well-known process, the reverse, namely artificial land uplift, is a much less observed and recognized event, even though the practice of injecting fluids underground is more than a half a century old. Injection technology has been advancing continuously since it came into wide use in the 1950s and 1960s in order to reinject the formation water extracted along with hydrocarbons, or to dispose of industrial wastes. The number of injection wells has grown exponentially, to the point that EPA (the United States Environmental Protection Agency) has identified approximately 400,000 injection boreholes in the USA alone (USEPA, 2002). The injection of water-based solutions, hydrocarbons, CO_2 or N_2 to enhance oil production (EOR) started in the 1940s and soon became an accepted technique for recovering additional oil from reservoirs that were already depleted or water flooded. Thermal recovery processes by vapor injection, used in reservoirs containing heavy (viscous) oil or bitumen, are generally accompanied by an noticeable uplift (for example, locally recorded up to 30 cm). Examples include the Cold Lake (Stancliffe and van der Kooij, 2001), Shell Peace River (Du et al., 2008), and Athabasca oil sands (Collins, 2007), in Canada.

In the Krechba gas field, Algeria, land rebound was caused by the reinjection of CO_2 separated from the produced gas (Vasco et al., 2010). Storing gas underground may generate measurable land uplift as well (Teatini et al., 2011a). The aquifer systems underlying Tokyo and Osaka, Japan (Sreng et al., 2011) and Taipei, Northern Taiwan (Chen et al., 2007), experienced a natural flow field recovery after cutting the water pumpage, and

significant land rebound as well. There are also examples of water being pumped into an oil field to mitigate land subsidence caused by oil production, including the case of Long Beach, California, USA. Here the mitigation program was carefully controlled and monitored (Pierce, 1970; Rintoul, 1981; Colazas and Strehle, 1995). Water injection started on a major scale in 1958 using appropriately treated seawater collected from shallow wells 30–120 m deep, later mixed with formation wastewaters produced with the oil. Eleven years later, when 2 m^3/s was being pumped into the oil field, the settling area had been reduced from 58 to 8 km^2, with local land surface rebound of 30 cm.

Land motion related to subsurface fluid injection went unnoticed for a long time in the vast majority of cases. There are a number of reasons for this. First, in most cases, the disposal of fluids occurred in deserted or sparsely inhabited areas where measuring surface displacements was not a priority, in part due to the large cost of leveling surveys. In other instances, uplift was so slight that no environmental hazards were created, no monitoring was installed, or the area involved was quite limited, with no damage to engineered structures or infrastructures reported or even expected. Only in recent times has satellite technology offered a relatively inexpensive, spatially distributed, accurate methodology for detecting ground movements worldwide. It has revealed anthropogenic uplifts of some interest in terms of magnitude, size of the area involved, and time of occurrence. The use of SAR-based techniques has grown rapidly over the last decade, facilitating the detection and measurement of rising areas. This is particularly true for surface movements connected with natural fluctuations of the groundwater head and in areas of aquifer storage and recovery (ASR), which have been systematically monitored by the United States Geological Survey: including, among others, Santa Clara Valley, California, USA (Schmidt and Burgmann, 2003), Santa Ana basin, California, USA (Galloway and Hoffmann, 2007), and Las Vegas Valley, Nevada, USA (Hoffmann et al., 2001; Bell et al., 2008). Measured uplift amounted to 4 cm from 1992 to 1999 in Santa Clara Valley and 3 cm from 2003 to 2005 in Las Vegas Valley. In addition, surface and borehole tiltmeters have been widely used in recent years to monitor ground heave within relatively small areas (Du et al., 2008). Teatini et al. (2011b) provide a recent thorough review of areas uplifted anthropogenically by injecting fluid underground.

As far as soil compressibility is concerned, the value of c_b in the first loading cycle is to be used if the aquifer is pumped, and in unloading/reloading when the aquifer is recharged/repressurized. The ratio $c_{b,loading}/c_{b,unloading}$ decreases with depth and may approach 1 order of magnitude for very shallow silty/clayey sediments (Teatini et al., 2011b).

Because of their low elevation and location on the sea, Shanghai in China and Venice in Italy represent two special cases where land subsidence mitigation is of paramount importance. Shanghai, a coastal city situated in the southern part of the Yangtze Delta, China, has experienced a large land subsidence (Table 1) due mainly to excessive long-term groundwater withdrawal and, secondarily, to the rapid development of the area.

41

Groundwater extraction in Shanghai dates back to 1860. The pumped water volume was quite small before 1949 and then it increased rapidly, especially in the late 1950s. The yearly pumping rate reached its peak of 200×10^6 m^3/year in 1963 (Figure 27a). Intensive groundwater extraction has caused severe land subsidence. During the period 1957–1961, the maximum yearly rate of subsidence peaked up to 17 cm/year as shown in Figure 27a (Zhang et al., 2015, Ye et al., 2016).
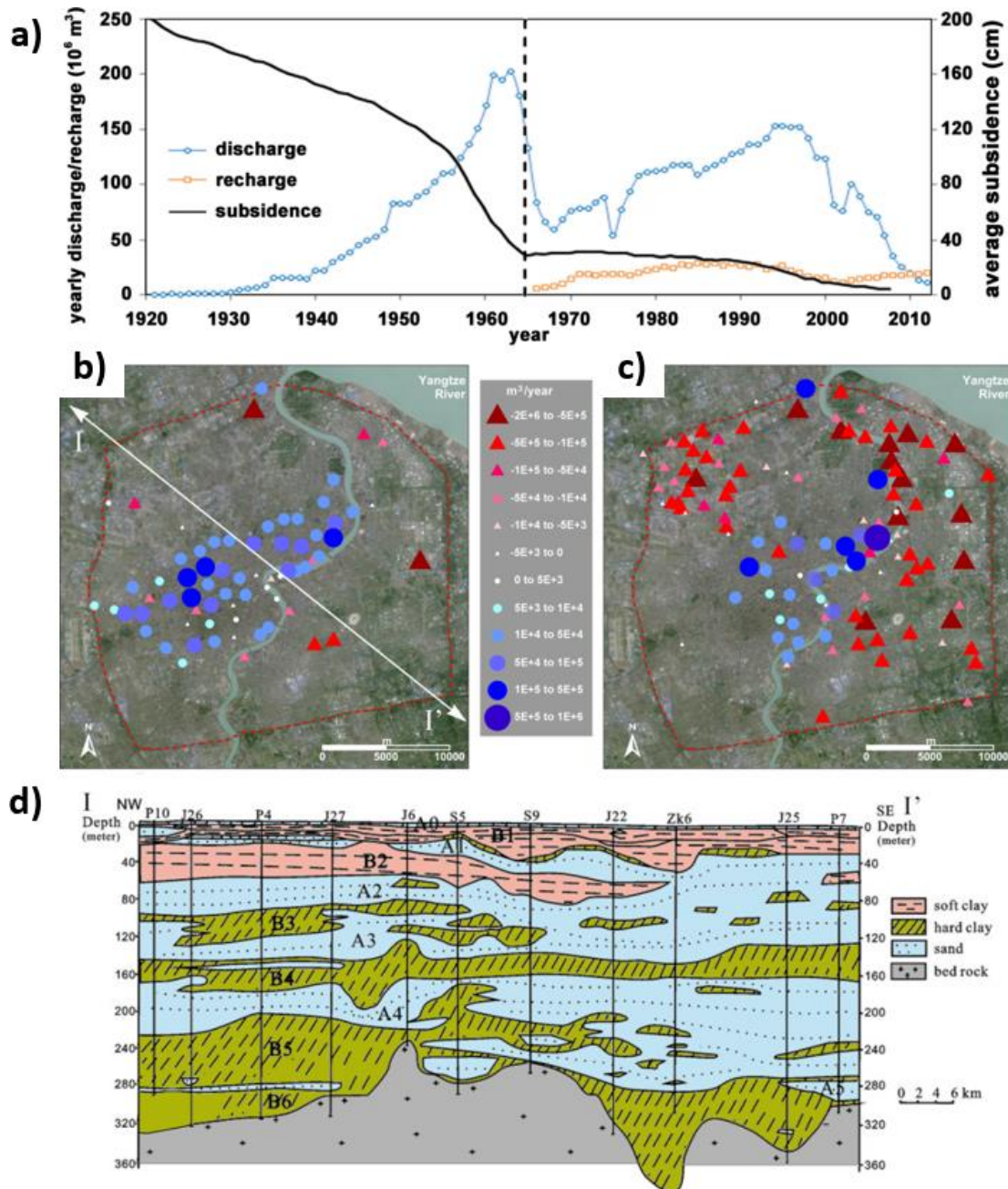
Figure 27 - a) History of groundwater pumping, artificial recharge, and average land subsidence in Shanghai (modified after Zhang et al., 2015). Pumping and recharge wells in b) aquifer A2 and c) aquifer A4 in Shanghai. The white-to-red triangles represent pumping wells (negative values), white-to-blue circles represent recharge wells (positive values). Symbol size is proportional to the average yearly rate from 1980 to 1996 (modified from Ye et al., 2016). d) Representative hydrogeological section of the Shanghai aquifer system along the cross-section I-I' shown in (b) (modified from Ye et al., 2016).

42

In order to control land subsidence, a series of measures were implemented by the Shanghai government beginning in the 1960s. These measures include:

- reduction of groundwater withdrawal;
- exploitation of deeper producing layers; and,
- artificial recharge of aquifers.

Pumping gradually moved from the second (A2) and third (A3) confined aquifer to the fourth (A4) and fifth (A5) aquifers, with decreasing yearly pumpage since 1998. Artificial recharge started in 1966 and slightly increased in the following years. The recharge has been carried out using properly treated tap water taken from the Huangpu River. Over the period 1983–1989, the yearly injection rate was nearly constant at 30×10^6 m^3/year. After that, it decreased slowly and increased year after year since 2003 (Figure 27a).

Figures 27b and 27c show the discharge and recharge wells in aquifers A2 and A4, along with the average annual discharge and recharge rates over the period 1980-1996. The number of recharge wells was much larger than the number of pumping wells in aquifer A2. Conversely, several pumping wells with high flow rates and a few recharge wells were active in aquifer A4. Because of the implementation of the above mitigation measures, land subsidence recently decreased to about 1 cm/year.

In Venice, land uplift is predicted with the aid of a finite element (FE) model (Figure 28a). An upheaval of the city induced by seawater injection into deep saline aquifers could significantly reduce the frequency of the high tides that periodically flood Venice. A recent exceptional high tide on November 12, 2019, peaked at 187 cm above datum and severely damaged the city (https://www.voanews.com/europe/venice-mayor-declares-disaster-city-hit-2nd-worst-high-tide↗). Early numerical studies based on a simplified lithostratigraphy of the Venetian subsurface (Comerlati et al., 2004) suggested that the city might be raised by pumping seawater into deep aquifers through 12 wells located on a 10 km diameter circle. Using a more accurate 3-D reconstruction of the Quaternary deposits, developed very recently from about 1050 km of multichannel seismic profiles and eight exploration wells, along with a more accurate representation of the injection boreholes, new FE predictions were performed (Teatini et al., 2011c). The new model simulates the lithostratigraphy of the lagoon subsurface and allows for a reliable assessment of the water volumes injected into the geologic formations based on the measured bottomhole overpressures, which vary both in space and time. Selection of the best hydraulic conductivity is discussed by Teatini et al. (2010), while rock compressibility in the unloading condition has been derived in agreement with Comerlati et al. (2004) and Ferronato et al. (2013). Pumping is planned along two Pleistocene sequences originating from the Alps and Apennines sedimentation and terminating just south and north of Venice, respectively, and the shelf portion of a rather continuous Pliocene sequence below the central lagoon, with arenite layers as deep as 1000 m below mean sea level. With a proper tuning of the injection pressure, the model (Teatini et al., 2011c) allows for

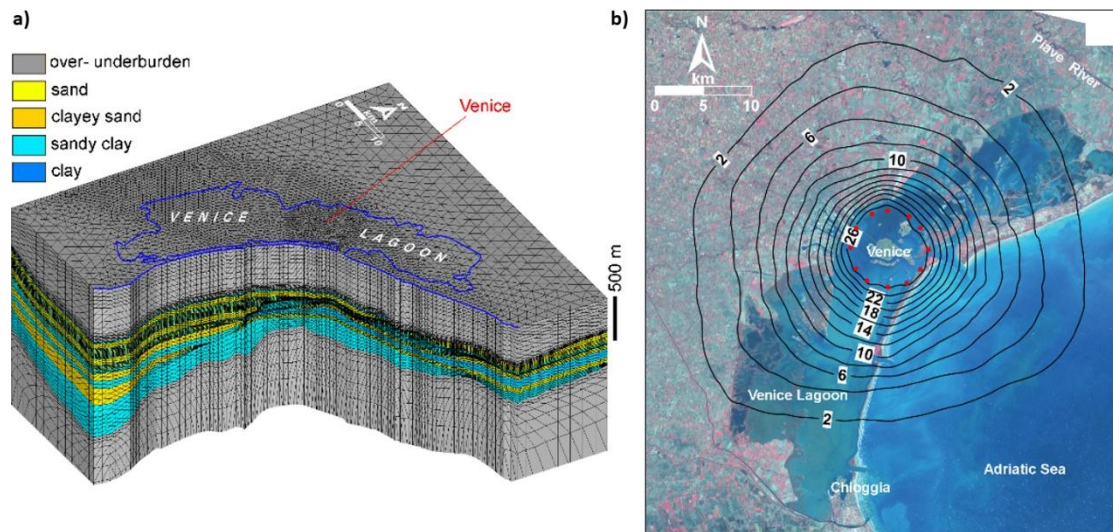prediction of a fairly uniform 25-30 cm uplift over 10 years after the initiation of injection (Figure 28b).

Figure 28 - a) Axonometric view of the tetrahedral mesh used to predict the anthropogenic uplift of Venice by seawater injection into saline aquifers. The mesh has 1,905,058 elements and 328,215 nodes. b) Predicted uplift (cm) at Venice after 10 years of injection into saline aquifers 650–1000 m deep below the lagoon. The injection wells are marked in red (modified after Teatini et al., 2011c).

A pilot experiment has been designed to verify the feasibility of the project for uplifting Venice (Castelletto et al., 2008). The pilot experiment plan foresees three boreholes located at the vertices of a triangle with sides 1 km long, in a lagoon area to be selected in the vicinity of Venice's historical center. The aim would be (1) to obtain further detailed lithostratigraphy of the underground lagoon; (2) to perform an injection test with (treated) seawater and measure the overpressure generated in the injected formation; (3) to monitor continuously and in real time land uplift in the area, with the aid of high-precision leveling, GPS, and satellite interferometry; and (4) to set up and experiment with a procedure of optimal control; for instance, the uniformity of uplift may be checked with the aid of sensor feedback automatically accommodating the injection rate in each single well. A detailed description of the project for anthropogenic uplift of Venice, its major environmental impact, and expected cost is provided by Gambolati and Teatini (2014).

5   Geomechanical Processes Related to Anthropogenic Land Subsidence

Apart from compaction or expansion, pore pressure change in the pumped or injected formation may induce other geomechanical processes, for example, the generation of local fractures that may extend to the ground surface, reactivation of preexisting faults, with a sharp increase in hydraulic conductivity, and reduction in strength. The consequences may greatly affect surface structures and infrastructures and expose aquifers to the risk of contamination.

44

The description of these mechanisms can be done with the aid of the Mohr-Coulomb representation of the effective stress state in the (σ, τ)-plane as shown in Figure 29, where compressive stresses are marked as positive. When water is removed, the pore pressure p decreases with respect to the original value $(p < p_0)$ and the effective stress σ increases in accordance with Terzaghi's principle. Hence, Mohr-Coulombs circle moves right-ward, that is, farther from the shear-τ-axis and generally, from the failure line bounding the envelope of the allowable stress states. In contrast, when fluid is injected p rises and may exceed p_0. In this case, the effective stress falls below the original in situ value, with Mohr-Coulombs circle moving left-ward, that is, toward the τ-axis and generally, the failure line. It is worth pointing out that during both pumping and injection, the maximum (σ_1) and minimum (σ_3) effective stresses may follow different paths, possibly creating an increase in the diameter of Mohr-Coulombs circle that approaches the failure line as shown in Figure 29 (Teufel et al., 1991; Segall and Fitzgerald, 1996). Notice that external stresses, that is, tectonic stresses, are assumed to be constant over the time period of an aquifer or reservoir production life (a few decades as a maximum). By distinction, the principal stress orientation and the ratio σ_1/σ_3 change significantly with depth (Zoback, 2007).
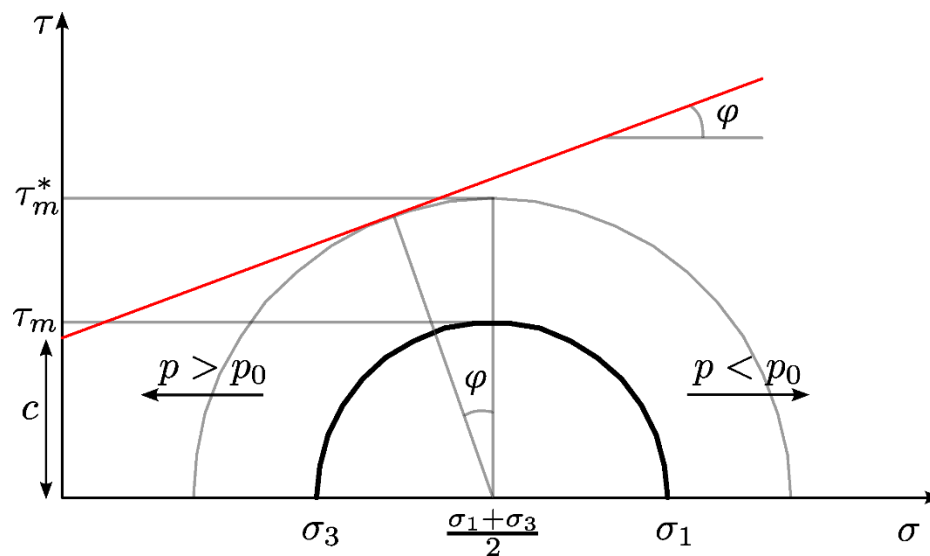
Figure 29 - Mohr-Coulomb's circles. When the pore pressure p increases because of fluid injection, the circles move left-ward and may achieve the limiting yield surface or friction line $\tau = c + \sigma tan\varphi$ where σ and τ are the normal and shear stress, respectively, c is the cohesion and φ is the friction angle. τ_m and τ_m^* are the current largest and maximum allowable shear stress, respectively, σ_1 and σ_3 are the maximum and minimum principal stress, respectively.

Two failure mechanisms may occur: a) if Mohr-Coulombs circle touches the envelope line a shear failure may ensue or a preexisting fault/thrust may be activated, and b) if Mohr-Coulombs circle crosses the τ-axis a tensile failure takes place. Moreover, a dilation (or dilatancy) phenomenon may be induced, that is, an increase in volumetric strain due to shear, increasing the magnitude of the injected formation's expansion. Shear dilation accompanies yield and strain weakening with permanent alteration in the fabric of

45

the fluid-bearing stratum through irreversible deformation, grain rearrangement, permeability change and porosity increase, potentially contributing to a measurable rebound of the land surface (Zoback, 2007).

5.1   Ground Ruptures

Ground ruptures associated with land subsidence caused by groundwater withdrawal have been reported from many alluvial basins in semiarid and arid regions since the late 1970s. Examples occur in the southwestern USA (Holzer et al., 1979; Jachens and Holzer, 1979; and, Holzer and Galloway, 2005), central Mexico (Pacheco et al., 2006; and Carreon-Freyre et al., 2016), Iran (Ziaie et al., 2009; and Mahmoudpour et al., 2013), Saudi Arabia (Bankher and Al-Harthia, 1999), Pakistan (Khan et al., 2013), and China (Shi et al., 2007; Wang et al., 2009; and He et al., 2017).

Fissure development has been observed both within areas where natural resources are exploited and along the area boundaries. Density, shape, length, aperture, depth, and dislocation of the fissures vary greatly from site to site, and are mainly related to subsoil lithostratigraphic variations. In several places only a few isolated fissures have formed; in others, many. Fissures vertically dislocated more than 2 m have been observed, up to 15 km long, 1-2 m wide, and 15-20 m deep. Considerable economic, social, and environmental damage is reported. Damage includes the rupture of borehole casings, pipes, and canals used for withdrawing groundwater and conveying water, oil and gas. Impacts occur in both rural zones, where the water is mainly used for crop production (for example, in the Sarir agricultural area, Libyan desert, and in southcentral Arizona, USA), as well as in urban areas (for example, in Mexico City, Queretaro, Mexico, and Celaya located within the Trans-Mexican Volcanic Belt in Mexico; in Beijing, Xian, and Wuxi China). Other consequences include the reduction of potable water supplies; cost increases for groundwater extraction; damage to surface structures (for example, houses, historical palaces, churches, and other buildings); cracking of infrastructure such as streets, water pipes, railways, and runways; injuries to livestock and other animals as well as to people; creation of preferential flow paths for contaminants from the surface into shallow aquifers, and triggering of severe soil erosion and creation of badlands topography near the rupture (Figure 30).

Figure 30 - A few examples of earth fissures due to groundwater pumping in a) Arizona, USA (courtesy of Joe Cook, Arizona Geological Survey, Tucson, AZ); b) damaging a house in Shunyi, Beijing, China (courtesy of Lin Zhu, Normal Capital University, Beijing, China); and, c) in Quetta, Pakistan (courtesy of Najeebullah Kakar, University of Balochistan, Quetta, Pakistan).

Several mechanisms have been proposed to explain the origin of ground rupture associated with the development of natural resources. Representations of a few proposed mechanisms are shown in Figure 31 (Holzer et al., 1979; Sheng and Helm, 1998; and Sheng et al., 2003). According to the direction of pumping-induced stresses below the surface, we may identify two main types of ground rupture: tensile fissures and shear fissures (Holzer and Pampeyan, 1981). The main difference between these two fissure types is the vertical offset observed in the field. Typically, tensile-induced earth fissures create slight or no offsets, while shear-induced earth failures have measurable scarps (Holzer and Pampeyan, 1981). However, this distinction may be difficult to recognize in urban areas, where some shear-induced ruptures initially appear without any vertical offset, as structures/infrastructures on the land surface mask the actual rupture displacements.

Starting from the early 2000s, research was mainly focused on modeling, and hence predicting, ground failure. A Mohr-Coulomb failure criterion was used by Budhu (2008) to analyze fissure initiation in heterogeneous sedimentary deposits. He found that the most potent mechanism for earth fissures formation combines bending and shearing. Geological discontinuities are the preferred location for ground failure to occur, with ruptures that initially form at the surface and then propagate downward, or vice versa, depending on the prevailing mechanisms. Using a continuum approach and the ABAQUS geomechanical simulator software (https://www.3ds.com/products-services/simulia/products/abaqus/↗), Hernandez-Marin and Burbey (2010, 2012) studied the spatial distribution of deformation, and normal and shear stresses that potentially lead to the formation of ground ruptures. Their results indicate that the presence of a preexisting fault zone largely controls the

47

deformation and stress regime of the porous medium during pumping, with areas of stress accumulation that may eventually lead to fissure formation. The simulations were carried out on 2-D vertical sections representing the Las Vegas Valley.
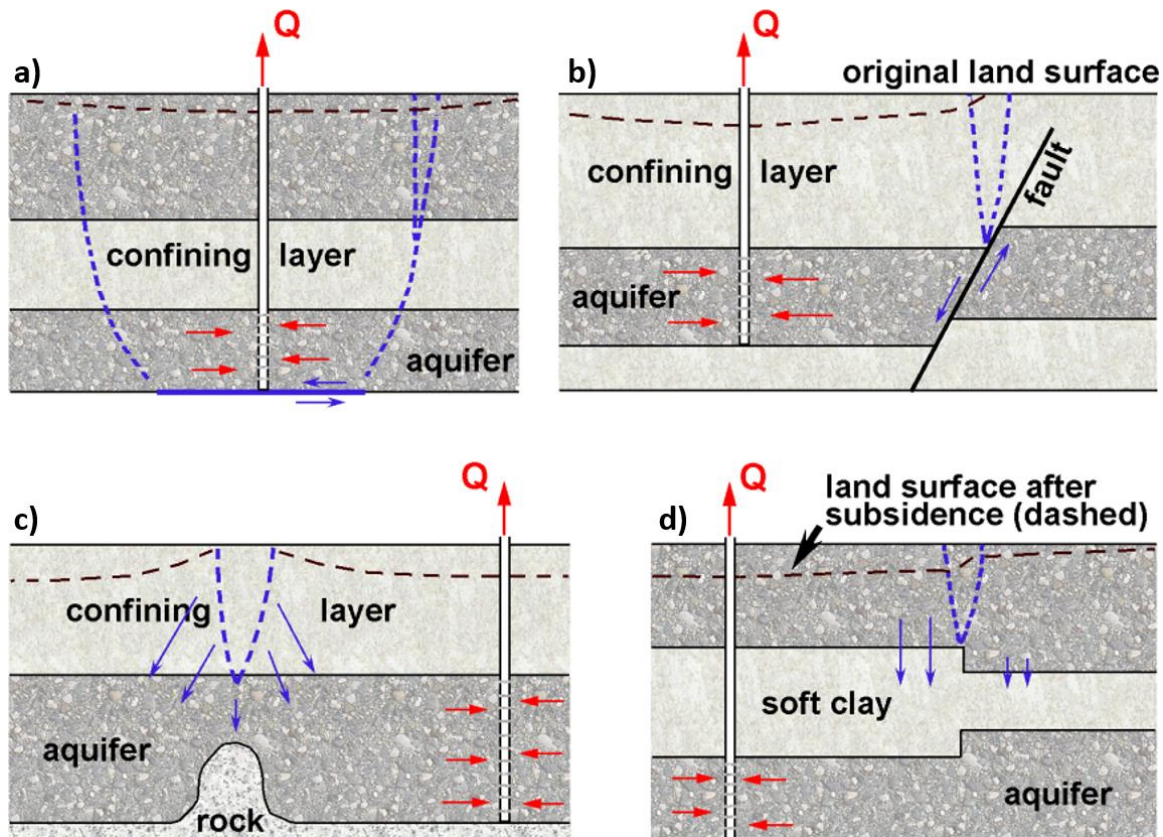
Figure 31. Sketches of some mechanisms that induce ground ruptures (dashed blue lines): a) horizontal displacement due to shearing on the plane of weakness or to tensile failure; b) reactivation of an existing fault caused by horizontal displacements; c) tensile fracture above a bedrock ridge; d) differential compaction due to heterogeneous thickness of [aquifer (rigid)]/[aquitard (compressible)] layers (modified after Sheng and Helm, 1998). The red and blue arrows represent the flow and displacement fields, respectively.

Recently, an original numerical approach based on "Interface Elements" (IE), developed to simulate the possible activation of regional faults due to hydrocarbon production (Ferronato et al., 2008; and, Jha and Juanes, 2014) has been used to simulate the earth fissure generation and propagation caused by groundwater pumping in Wuxi, China. Groundwater pumping between 1985 and 2004 has caused land subsidence larger than 2 m (Ye et al., 2018). The model outcomes show the presence of a shallow (~80 m deep) bedrock ridge crossing the Yangtze River delta is the key factor triggering earth fissure development in this area (Figure 32). Bending of the alluvial deposits around the ridge tip and shear stress due to the uneven piezometric change and asymmetrical shape of the bedrock have caused the earth fissure to form at the land surface and propagate downward to a maximum depth of approximately 20 to 30 m. Maximum sliding and openings are computed to be in the range of 10 to 40 cm, respectively.

Figure 32 - 3-D FE-IE mesh developed by Ye et al. (2018) to model land subsidence and earth fissure propagation in Wuxi, China. The various geologic components (bedrock, aquifers and aquitards, fissure) are highlighted with different colors and enlarged in the sub-panels (modified from Ye et al, 2018).
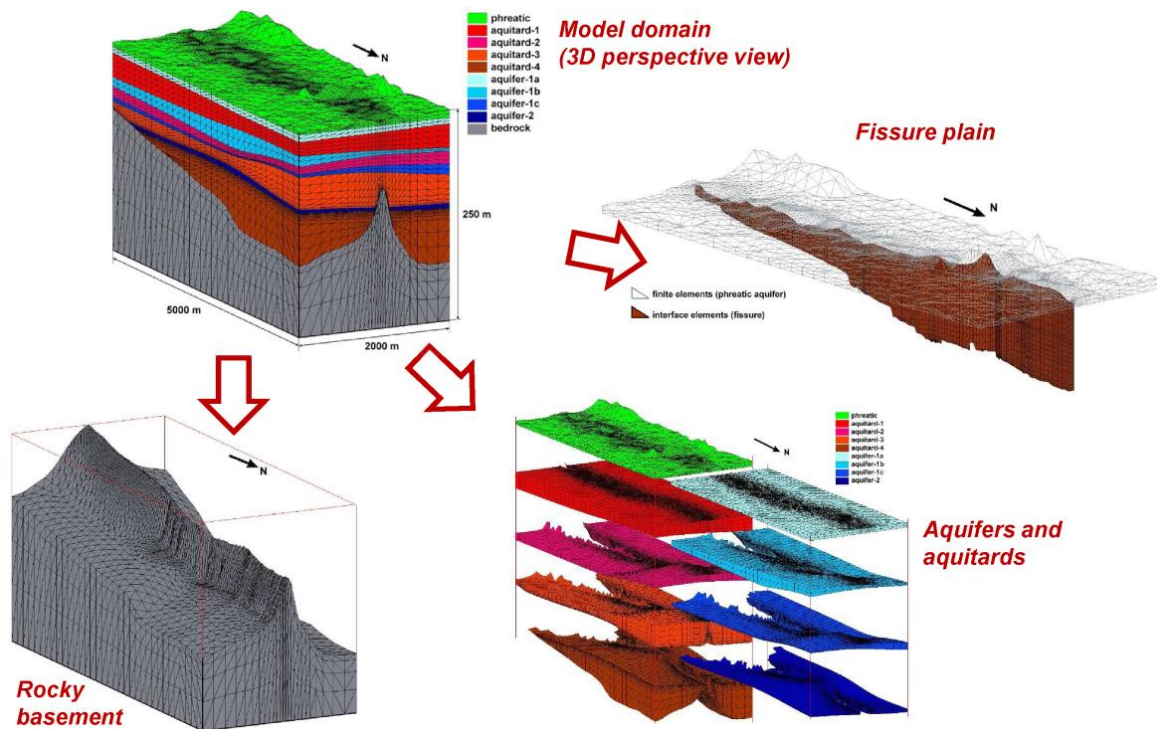
The geomechanical model of earth fissuring and fissure activation is based on the structural equations of poroelasticity (as discussed in Box 3↴) solved in a three-dimensional setting with the aid of the FE-IE approach. While standard FEs are used to represent a continuum, IEs prove especially effective in examining the relative displacements of adjacent elements, such as the opening and slippage of preexisting faults or the generation of new fractures (using an elastoplastic constitutive law based on the Mohr-Coulomb failure criterion). A zero-thickness IE compatible with linear FE consists of a pair of linear elements (1-D in a 2-D problem, 2-D in a 3-D problem) with the opposite nodes coinciding. The interface displacements in the local reference frame associated with each element are the aperture δ_n and the slippage δ_{s1} and δ_{s2} between the "top" and the "bottom" face of the element. The displacement components are related to the interface stresses σ_n, τ_{s1}, and τ_{s2}, with σ_n taken as the normal stress (negative in compression, positive in expansion), and τ_{s1} and τ_{s2} as the shear stress components in the interface plane. Irreversible plastic displacements of the interface may take place wherever the limiting tensile or the shear strength are exceeded. Assuming conservatively that no tensile strength is allowed, the opening of fissure/fault surfaces occurs when the stress normal to the interface plane, that is, σ_n, becomes positive. Irreversible slip occurs when the Mohr-Coulomb failure criterion is violated. Sealing fissures, that is, ones with a no-flux surface, are simulated allowing the pressure gradient acting on the contact surface to be different.

Ground ruptures are the focus of the recently funded UNESCO-IGCP641 project M3EF3 (Mechanisms, Monitoring and Modeling Earth Fissure generation and Fault activation due to subsurface Fluid exploitation). A large amount of material about ground ruptures can be found in the project website (http://www.igcp641.org/↗).

5.2   Induced Seismicity

In recent years, concerns have been raised about the risk of inducing or triggering seismic activity as a consequence of pumping water from or injecting water into geologic formations (Ellsworth, 2013). Very recently, injection-induced earthquakes have become a discussion topic and a focus for research in connection with (i) hydraulic fracturing of tight shale formations for hydrocarbon production; (ii) disposal of wastewaters; and (iii) enhanced geothermal systems. The activation of thrusts/faults caused by groundwater withdrawal (as well as by fluid injection) may pose a serious hazard of anthropogenic seismicity. According to Ellsworth (2013), the mechanism responsible for inducing seismicity "appears to be the well-understood process of weakening a pre-existing fault" by changing the fault loading conditions. In essence, "increasing the shear stress, reducing the normal stress and/or elevating the pore pressure can bring the fault to failure triggering the nucleation of an earthquake" (Figure 33). The number of earthquakes with magnitude $M \geq 3$ recorded annually in the USA midcontinent has grown significantly since 2001, with anthropogenic earthquakes suspected as being largely responsible for the increase. Magnitudes are usually determined from measurements of an earthquake's seismic waves as recorded on a seismogram. Notice that the M scale is logarithmic, so that each unit represents a ten-fold increase in the amplitude of the seismic waves. The value $M = 3$ characterizes "minor" events, i.e., events often felt by people, but very rarely causing damage. As the energy of a seismic wave is $10^{1.5}$ times its amplitude, each unit of magnitude represents a nearly 32-fold increase in the seismic energy (strength) of an earthquake. Earthquake initiation and propagation is site-dependent, influenced by fault frictional properties and geometry, the pre-seismic natural stress regime, stress changes induced by anthropogenic activity, and the volume of injected or pumped fluid.
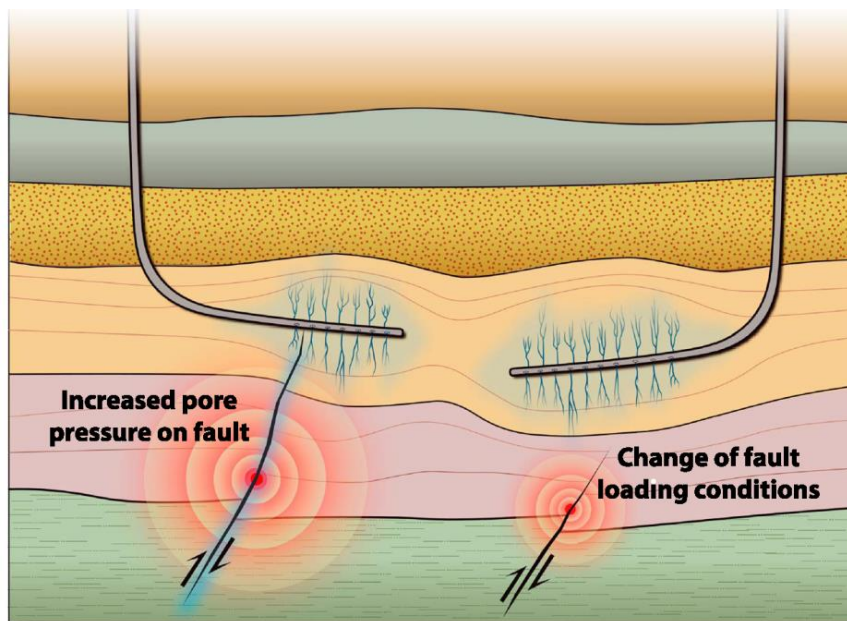
Figure 33 - Sketch of the mechanisms inducing earthquakes: (left) pore pressure increase or (right) change of the geostatic load in the vicinity of a fault. In the above cases, both the effective normal and tangential stresses acting on the fault change, causing fault reactivation (after Schultz et al., 2017).

Several cases have been reported in which micro-seismic events were correlated directly to hydraulic fracking. These cases are notable because of the public concern they raised, although the magnitudes are small, usually not creating appreciable damages. Extracting hydrocarbons from shale requires the generation of a network of open fractures connected to the producing boreholes. This is accomplished by way of a high-pressure injection of water into the formation. Thus, fracking intentionally induces numerous micro-seismic events, the vast majority of which are of $M < 1$. However, a number of cases have recently been experienced where earthquakes large enough to be felt correlated directly to hydraulic fracturing. Holland (2013) investigated a sequence of events in south-central Oklahoma, with maximum $M = 2.9$, revealing a clear temporal correlation between fracking operations in a nearby well and seismic activity. On April 2011, the Blackpool area of northern England experienced seismicity of magnitude 2.3 shortly after the hydraulic fracturing of a well to develop a shale gas reservoir in the Bowland basin (The Royal Society and the Royal Academy of Engineering, 2012).

Injection disposal wells appear to have triggered or induced several earthquake sequences in the mid-western USA. Before 2011, the $M = 4.8$ event in 1967 near Denver, Colorado, USA, was the largest event widely accepted in the scientific community as having been induced by wastewater injection (Hermann and Park, 1981). By that time, the earthquakes had migrated as far as 10 km from the injection point along an ancient fault system, tracing a critical pressure front of 3.2 MPa. Wastewater disposal appears to have induced over 109 small earthquakes ($0.4 < M < 3.9$) from January 2011 to February 2012 in Youngstown, Ohio, USA, close to a deep fluid injection well. The main shocks occurred at

depths between 3500 and 4000 m along a fault located in the Precambrian basement (Kim, 2013). A similar situation was observed in central Arkansas, USA (Horton, 2012).

A number of studies have explored the response of water injection-induced activity in enhanced geothermal systems. The most prominent example is an $M = 3.4$ event induced in 2006 by the stimulation of a geothermal reservoir below the city of Basel, Switzerland, at a depth of about 5000 m (Häring et al., 2008). Thousands of smaller shocks were recorded afterward, leading insurance companies to claim over 7 million euros in damage. In 2003, at the geothermal site of Soultz-sous-Forts, France, stimulation of the 4800 m deep reservoir produced seismic events with magnitude of up to $M = 2.9$ in 2003 (Baisch et al., 2010). Epicenters align along a preexisting subvertical regional-scale fault structure. A hot-fractured-rock project was launched at Cooper Basin, South Australia, in 2002 to exploit the Habanero granite reservoir at a depth of 4000-4500 m. Various stimulation experiments have been conducted which triggered earthquakes with moment magnitude between 1.7 and 3.1 with hypocentral distances between 2.4 and 7.8 km and depth between 3900 and 4500 m (Baisch et al., 2010). In these cases, injection caused significant changes in the effective stress regime due to both the pressure change of the formation fluid and the thermal drawdown of the rock, increasing the likelihood of fault reactivation and consequently, induced seismicity (Gan and Elsworth, 2014).

As regards the possibility of inducing seismic events by groundwater pumping, the $M = 5.1$ earthquake that occurred in May 2011 in Lorca, southeast Spain, is a renowned case study. The earthquake struck the city of Lorca causing significant property damage, injuring hundreds of people and resulting in nine casualties. The hypocenter was located in a complex, active system of strike-slip faults at a depth of 3 km. According to Gonzalez et al. (2012), the event may have been triggered by the significant crustal unloading caused by the ~250 m decline in groundwater level occurring between 1960 and 2010 as a consequence of aquifer over-draft. The decrease in total stress may have relaxed the effective normal stress acting on the fault plane, thus triggering its reactivation. However, we note that there exists no general consensus in regards to the relation between piezometric lowering and the 2011 event.

When concern is raised about the possibility of inducing earthquakes, an area-wide reconnaissance study aimed at identifying major geological discontinuities is of paramount importance. These data are best used as input to a modeling tool capable of predicting fault/thrust activation resulting from the removal or injection of fluid (Ferronato et al., 2008; Gan and Elsworth, 2014; Jha and Juanes, 2014; and, Teatini et al., 2014). With the aid of an ad hoc model, we can estimate the sliding of the fault/thrust, and hence predict the seismic moment. The seismic literature presents several empirical relationships enabling us to predict the possible magnitude M induced by a fault/thrust reactivation. Recently, Mazzoldi et al. (2012) have suggested an equation based on the seismicity theory that provides an estimate of the seismic moment M_0 of a possible seismic event induced or triggered by a fault/thrust slip as expressed by Equation 29.

$$M_0 = G \, \Delta L \, \Delta Z_a \, s_a \tag{29}$$

where:

ΔL = horizontal length of the activated portion of the fault/thrust (L)

ΔZ_a = height of the activated portion of the fault/thrust (L)

s_a = average slip of the fault/thrust surfaces (L)

G = shear modulus of the formation incorporating the reactivated fault/thrust $(ML^{-1}T^{-2})$

G is related to soil compressibility through the relationship shown in Equation 30.

$$G = \frac{1}{2c_b} \frac{1 - 2\nu}{1 - \nu} \tag{30}$$

where:

ν = Poisson's ratio (ratio of transverse strain to axial strain in simple uni-axial compression)

The seismic moment M_0 obtained from Equation 29 may be converted into a moment magnitude M used to measure the strength of the seismic event. The M_0 - M relationship was defined by (Kanamori and Anderson, 1975) as shown in Equation 31.

$$M = \frac{2}{3}(\log_{10} M_0 - 9.1) \tag{31}$$

M_0 is expressed in Newton-meters (Nm). As far as G is concerned, in Equation 30 we have to use the value of c_b in the first loading cycle if the aquifer is pumped, and in the second unloading/reloading phase if the aquifer is recharged/repressurized. As a matter of fact, seismicity during reservoir production typically occurs when the pore pressure depletion has achieved relatively high values, that is, with a stress state never experienced previously by the reservoir formation. The Groningen reservoir in The Netherlands is an example where this occurred (van Thienen-Visser and Breunese, 2015.)

6   Example of Anthropogenic Land Subsidence Calculation

We provide herewith a practical example of calculation of land subsidence due to groundwater withdrawal. Data are taken from Venice, Italy, which experienced an important anthropogenic land settlement in the second half of the twentieth century, and are summarized in Gambolati (1972). The data needed for the calculation are of two kinds. The first type comprises litho-stratigraphy of the subsoil down to the depth of interest (that is, the depth where drawdown has occurred) along with the mechanical and hydraulic properties of each stratum (considered to be homogeneous); the second type addresses the history of the piezometric decline experienced in the permeable (that is, sandy) formations

from which the wells pump. Table 2 shows the simplified litho-stratigraphy of the Venice area down to about 300 m depth. The compactable thickness, which differs in some cases from the total thickness, takes account of layers of sand, which are much stiffer than the layers of clay that incorporate them. Table 2 includes several aquifer levels that appear frequently in the sedimentary sequence at various locations in Venice. We refer particularly to layers 2, 4, 6, 8, 11 and 13, which are composed predominantly of sands and which host most of the pumping well intakes as well as the borehole piezometers. Of course, a more accurate subdivision of the litho-stratigraphy is possible when the underground is mapped in greater detail, thus allowing for a better classification of the strata of mixed nature.

Table 2 - Simplified stratigraphy and lithology in the Tronchetto area of Venice, Italy.

Layer	Mid-layer depth (m)	Layer thickness (m)	Compactable thickness (m)	Lithological description
1	28.0	56	45	Clay, mud, sand with clayey intercalations, sandy clay, peaty clay
2	71.5	31	31	Sand, clayey sand, alternating sand and clay
3	92.0	10	10	Prevalently clay
4	102.0	10	10	Sand with thin layers of clay
5	113.0	12	6	Alternate layers of clayey sand and clay
6	137.0	36	36	Sand, sand with clayey intercalations
7	159.0	8	8	Prevalently clay
8	168.0	10	10	Sand, clayey sand
9	194.0	22	22	Clayey sand, sand intercalated by clay
10	210.0	10	10	Prevalently clay
11	222.5	15	15	Prevalently sand
12	242.5	25	25	Prevalently clay
13	267.5	25	25	Prevalently sand, light sandstone, thin layers of light gravel
14	285.0	10	8	Alternate layers of sand and clay

Table 3 shows the piezometric levels measured in 1905 at various depths. The correlation between the depth of Table 3 and the aquifer levels of Table 2 is far from perfect. This could be due to errors in making the measurements of Table 3, but also likely is due to different geologic characteristics and the locations and depths of wells where the values of Table 3 were taken. In recent time, new data have permitted the compilation of Table 4 in which the piezometric levels of the various aquifers are average values based on a number of boreholes of the same depth.

54

Table 3 - Piezometric level observed in Venice as of 1905.

Measurement depth (m)	Piezometric level (m above mean sea level)
56	2.95
91	3.80
112	4.55
135	4.90
155	5.60
170	6.25
198	6.70

Table 4 - Combined data from several wells in the Venice area.

Layer	Piezometric level (m above mean sea level)	
	in 1940	**in 1966**
2	1.5	
4	1.0	-3.0
6	2.5	
11	2.0	-6.0
13	4.0	-4.5

An analysis by Lofgren and Klausing (1969) on nonconsolidated soil (like that of the Venice Lagoon) to a depth of 230 m yielded porosity values from 0.35 to 0.55, with values near 0.4 occurring most frequently. The average specific weight of solid grains in the same study varied from 2680 to 2730 kg/m³. We assume an average value for the porosity ϕ of 0.4 and for the specific weight of soil grains, 2700 kg/m³.

  More difficult is the choice of average values for compressibility of the sand and clay, due to the wide range of variability of these parameters. Figure 34a provides the behavior of c_b versus σ_z for sand and Figure 34b gives the behavior for clay. Notice that the values of Figure 34a are lab values measured on samples that were allowed to expand laterally while in situ compaction occurs with lateral expansion precluded (oedometric conditions). Hence the values of Figure 34a must be multiplied by the factor:

$$\frac{1+\nu}{3(1-\nu)}$$

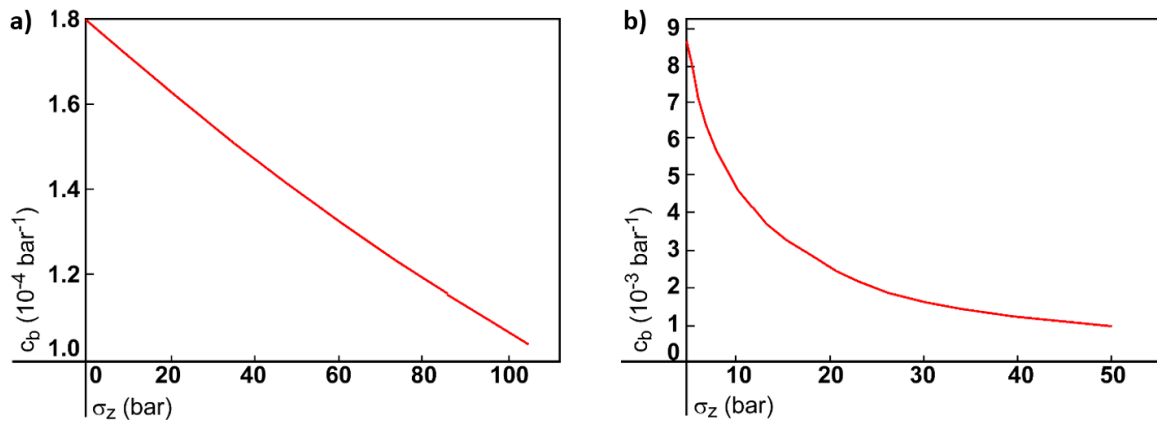that is, 0.55, assuming ν (Poisson ratio) = 0.25.

Figure 34 - Stress-dependent compressibility of a) sand and b) clay in the Venice coastland (modified after Gambolati (1972)).

The subsidence calculation is made for the period 1952-1969 where subsidence observations are available. Table 5 provides the initial stress σ_{z0} for each depth interval of Table 2 assuming full saturation throughout, and the compressibility derived from either Figure 34a for sand or Figure 34b for clay. Numerical values for the midplane of each stratum were used in the calculation.

Table 5 - Initial stress and compressibility for layers of the Venice lithostratigraphic sequence.

Layer	σ_{z0} (bar)	c_b (10^{-4} bar^{-1})
1	3.0	50.0
2	7.0	0.96
3	9.0	50.0
4	10.0	0.94
5	11.0	45.0
6	13.5	0.93
7	15.5	33.0
8	16.5	0.91
9	19.5	0.90
10	21.0	25.0
11	22.5	0.89
12	24.0	22.0
13	26.5	0.87
14	29.0	18.0

The data in Tables 3 and 4 are not sufficient to support an unequivocal deduction of the piezometric decline in the aquifers. However, one may note that the two deepest aquifers have had approximately equal decreases in piezometric level between 1940 and 1966, about twice the drop recorded in the layer at 100 m depth. Therefore, it is reasonable to postulate the existence of two distinct families of hydraulically disconnected aquifers separated by the clay layer at 210 m depth (layer 10 in Tables 2 and 5).

We have summarized our analysis and evaluation of the piezometric level data available in the representative data of Table 6. In some cases, the values differ from the observations of Tables 3 and 4, although they retain the order of magnitude involved and individually have only a slight influence on the final calculation of subsidence, which is substantially affected by the difference between the piezometric levels of successive periods. The difference in values used in the practical calculation are summarized in Table 7. Between 1900 and 1944, from 1944 to 1966, and between 1966 and beyond, we assume a linear time dependence of the piezometric level.

Table 6 - Derived data for the decline of the piezometric levels in the Venice aquifer.

Layer (aquifer only)	Piezometric level (m above mean sea level)		
	1900	**1944**	**1966**
2	3.0	1.5	-3.0
4	5.0	1.5	-3.0
6	5.0	1.5	-3.0
8	5.0	1.5	-3.0
11	5.0	3.0	-5.0
13	5.0	3.0	-5.0

Table 7 - Computation of the subsoil compaction and total land subsidence in the Tronchetto area of Venice.

Layer	c_v (m²/year)	Piezometric level change 1952-1969 (m)	Compaction 1952-1969 (cm)
1			3.95
2		-3.5	0.10
3	0.45		1.20
4		-3.5	0.03
5			0.90
6		-3.5	0.10
7	0.45		0.75
8		-3.5	0.03
9			0.07
10	0.45		0.87
11		-6.4	0.08
12	0.45		1.10
13		-6.4	0.13
14			0.28
Total subsidence 1952-1969 (cm):			**9.60**

Finally, to make use of these data, we must have a value of the coefficient of consolidation c_v of clay. Referring again to the experience by Lofgren and Klausing (1969),

we adopt the value c_v = 0.45 m²/year found for clay at depth. For the upper layer we ignore the existence of delay, and we extend this assumption to the strata with thin alternations of sand and clay, because of the small thickness of the clay layers.

We have calculated, for each sand and clay stratum, the compaction from 1952 through 1969, with data from Tables 2, 5, and 6. For clay layers 3, 7, 10, and 12 it was necessary to calculate, with the data of Table 7, the compaction that occurred between 1900 and 1952 and between 1900 and 1969. This was done using Figure 17, by distributing the reduction in piezometric level proportionally over the periods 1900-10, 1910-20, 1920-30, 1930-40, 1940-44, 1944-52, 1952-60, 1960-69. It was assumed that the piezometric decline over each period occurred instantaneously at the period beginning with the superposition of the effects of all the instantaneous declines. It was also assumed that the effect of the extraction did not propagate below 290 m, the depth of the deepest well in the Venice Lagoon area. The results of our calculations are shown in Table 7. The computed subsidence amounts to 9.6 cm and compares quite satisfactorily with the value of 12 cm measured in Venice over the 1952-1969 period.

7   Conclusions

Anthropogenic land subsidence as related to subsurface fluid production has been known for almost a century. Groundwater withdrawal is the primary cause worldwide. Although overall damage today is estimated at billions of dollars a year (for example, Borchers and Carpenter, 2014), it is expected to increase due to population and economy growth. Land subsidence is still a problem that is under-evaluated by both governments and public opinion, especially in developing countries. Impacts include the loss of conveyance capacity in canals, streams and rivers, diminished effectiveness of levees, damage to roads, bridges, buildings, water wells, pipelines and other surface structures and infrastructures, increasing vulnerability of aquifers to saltwater intrusion, contamination of shallow aquifers through ground ruptures, and the flooding of coastal and inland urban areas (for example, New Orleans, Louisiana, USA and Mexico City, Mexico). The environmental impact of land subsidence has shifted over the last decade from rural and industrial sites (for example, the Antelope Valley, California, USA, or the Po River delta, Italy) to urban centers (for example, Shanghai, China and Mexico City, Mexico) because of increasing population and growth of mega-cities. Whereas in 1950, New York was the only urban area totaling more than 10 million people, presently more than 30 cities in the world exceed this impressively large number, most of them located on the coasts of developing countries.

When estimating the impacts of land subsidence over horizontal multi-aquifers, an initial approach uses 1-D vertical movement with ground settlement $\eta = \Delta p \, c_b \, s_0$ (that is, equal to the compaction η of the pumped unit with initial thickness s_0 and uniaxial vertical compressibility c_b subject to the pore pressure decline (Δp). If the fraction of clayey/silty soils (namely aquitards/confining beds and intersperse clayey/silty lenses) is important,

compaction, hence land subsidence, can be delayed in time relative to the compaction of the pumped sandy formations. As a major consequence land subsidence can still continue after well pumping ceases. Rebound due to aquifer recharge and aquitard re-pressurization (either natural or artificial) can make up for only a small fraction of the overall land subsidence as c_b in expansion is generally significantly smaller than virgin c_b in compression, and especially so in clayey/silty units.

The mechanisms underlying the basic process are well understood and universally accepted, and the mathematical modeling of past events and expected future cases is also well established. Modern computer technology allows for the simulation of complex geology and geometry in subsiding basins, of arbitrarily distributed pumping rates, of heterogeneity, anisotropy and non-linearity of the porous media properties, with a degree of accuracy inconceivable until only a few years ago. Measuring and monitoring anthropogenic land subsidence is presently at a very advanced stage, especially with the aid of satellite technology. Scientists can help support decision makers toward predicting, preventing or at least mitigating land subsidence successfully, although certain specific areas may still require more in-depth investigation. These include the 3-D deformation and stress fields correlating to groundwater pumping, uplift caused by water injection, and inverse modeling calibration. Land subsidence rates have been drastically reduced in several places around the world, for example, in Venice, Italy; Tokyo, Japan; and more recently Shanghai, China by exploiting water resources other than groundwater. However, for the majority of other mega-cities this target is not within easy reach. This is why land subsidence was recently mentioned as one of the most urgent threats to sustainable development, in the latest UNESCO International Hydrological Programme VIII (2014-2020).

Major research advancements are needed to better predict earth fissuring, hydraulic fracturing, fault activation, and induced seismicity. Modeling these processes require approaches developed in the field of discontinuous mechanics, approaches only partially assimilated in geosciences so far. Significant progress has been made in understanding theoretical mechanisms. However, monitoring their occurrence, characterizing their rheological properties, and developing reliable, robust, and accurate numerical models still pose major challenges for research efforts in the near future.

8   Exercises

Exercise 1

Compute the total stress, vertical effective stress, and water pore pressure at a depth of 15 m below the bottom of a 6 m deep lake. The soil below the lake bottom consists of soft clay with a thickness of more than 15 m (Figure Exercise 1-1). The clay porosity is 40 percent and the specific weight of soil is 2700 kg/m³. How will the effective stress change if the water level in the lake drops to 4 m?
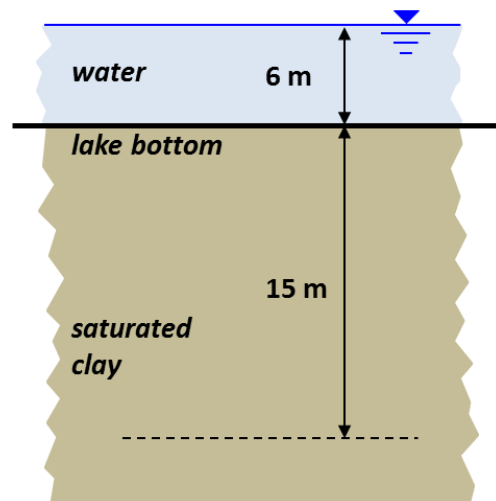

Figure Exercise 1-1 - Sketch of exercise 1.

[Click here for solution to exercise 1](#)⤵

Exercise 2

The aquifer system shown in Figure Exercise 2-1 undergoes groundwater pumping. The decline of the water table and piezometric head are recorded after 1 month and shown in the figure. The following information is available:

- aquitard: soil compressibility $c_b = 10^{-3}$ bar^{-1};
- phreatic aquifer: porosity 35 percent, moisture content 10 percent, $c_b = 10^{-4}$ bar^{-1}; and,
- confined aquifer: $c_b = 2 \times 10^{-5}$ bar^{-1};

Compute the cumulative land subsidence after 1 month and after 10 years assuming that the pressure decrease within the aquifers remains constant and that the aquitard hydraulic conductivity is three orders of magnitude smaller than that of the aquifers.
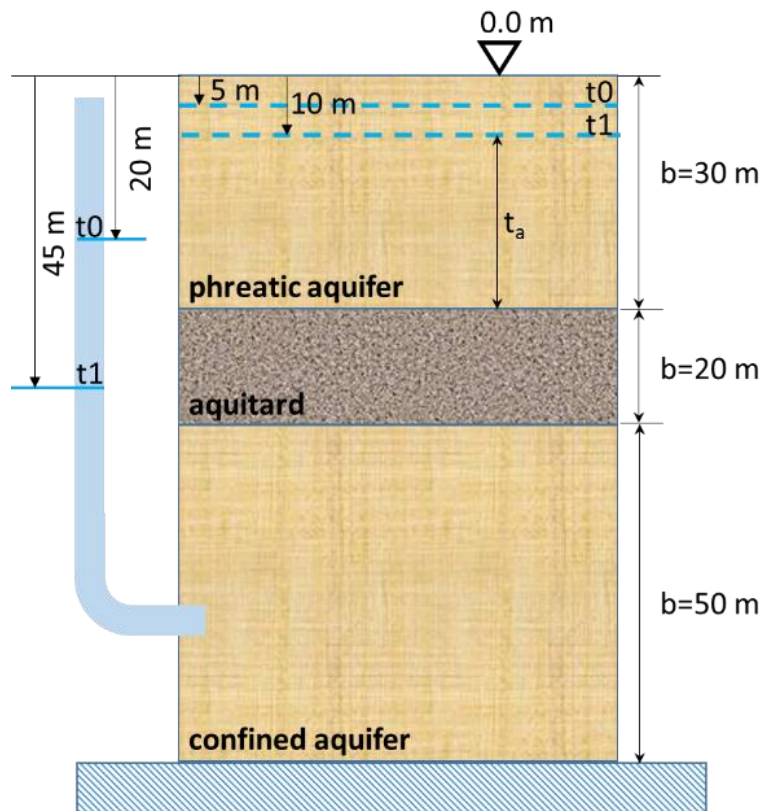

Figure Exercise 2-1 - Sketch of exercise 2.

Click here for solution to exercise 2 ⤸

Exercise 3

Groundwater is pumped from the two confined aquifers shown in Figure Exercise 3-1. After 1 year, a cumulative land subsidence equal to 0.1 m is measured at the land surface. The piezometric drawdown recorded at the same time in aquifer 1 and aquifer 2 amounts to 20 m and 15 m, respectively. Assuming a steady state pressure in the intervening aquitard, and the following ratios between the layer compressibility $c_{b,aquifer1} = 2\ c_{b,aquifer2}$ and $c_{b,aquifer1} = 0.1\ c_{b,aquitard}$, compute the compressibility of the three soil layers.
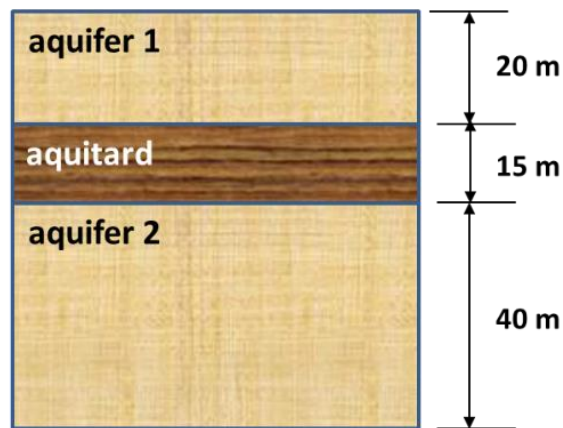

Figure 3-1 - Sketch of exercise 3.

Click here for solution to exercise 3 ↴

9   References

Allen, S.A., 1984, Types of land subsidence. *in*, Guidebook to Studies of Land Subsidence Due to Ground-Water Withdrawal, editor, J.F. Poland. United Nations Educational Scientific and Cultural Organization, Paris, France, pages 291–305.

Allis, R., C. Bromley, and S. Currie, 2009, Update on subsidence at the Wairakei-Tauhara geothermal system, New Zealand. Geothermics, volume 38, pages 169–180.

Amelung, F., D. Galloway, J.W. Bell, H.A. Zebker, and R.J. Laczniak, 1999, Sensing the ups and downs of Las Vegas: InSAR reveals structural control of land subsidence and aquifer system deformation. Geology, volume 27, pages 483–486.

Aobpaet, A., M.C. Cuenca, A. Hooper, and I. Trisirisatayawong, 2013, InSAR time-series analysis of land subsidence in Bangkok, Thailand. International Journal of Remote Sensing, volume 34, number 8, pages 2969–2982.

Baisch, S., R. Vörös, E. Rother, H. Stang, R. Jung, and R. Schellschmidt, 2010, A numerical model for fluid injection induced seismicity at Soultz-sous-Forêts. International Journal of Rock Mechanics and Mining Sciences, volume 47, pages 405–413.

Bankher, K.A., and A.A. Al-Harthia, 1999, Earth fissuring and land subsidence in Western Saudi Arabia. Natural Hazards, volume 20, pages 21–42.

Baú, D., M. Ferronato, G. Gambolati, and P. Teatini, 2002, Basin-scale compressibility of the Northern Adriatic by the radioactive marker technique. Géotechnique, volume 52, number 8, pages 605–616.

Bear, J., 1972, Dynamics of Fluids in Porous Media. Elsevier, New York.

Bell, J.W., F. Amelung, A. Ferretti, M. Bianchi, and F. Novali, 2008, Permanent scatterer InSAR reveals seasonal and long-term aquifer system response to groundwater pumping and artificial recharge. Water Resources Research, volume 44, W02407, doi:10.1029/2007WR006152↗.

Berardino, P., G. Fornaro, R. Lanari, and E. Sansosti, 2002, A new algorithm for surface deformation monitoring based on small baseline differential SAR interferograms. Institute of Electrical and Electronics Engineers Transactions on Geoscience and Remote Sensing, volume 40, number 11, pages 2375–2383.

Biot, M.A., 1941, A general theory of three-dimensional consolidation. Journal of Applied Physics, volume 12, number 2, pages 155–164.

Biot, M.A., 1955, Theory of elasticity and consolidation for a porous anisotropic solid. Journal of Applied Physics, volume 26, number 2, pages 182–185.

Borchers, J.W., and M. Carpenter, 2014, Land subsidence from groundwater use in California, Full Report of Findings. California Water Foundation, 151 pages.

Buckley, S.M., P.A. Rosen, S. Hensley, and B.D. Tapley, 2003, Land subsidence in Houston, Texas, measured by radar interferometry and constrained by extensometers. Journal of Geophysical Research, volume 108, number B11, page 2542, doi:10.1029/2002JB001848↗.

Budhu, M., 2008, Mechanisms of earth fissures using the Mohr-Coulomb failure criterion. Environmental Engineering and Geoscience, volume 14, number 4, pages 281–295.

Cabral-Cano, E., T.H. Dixon, F. Miralles-Wilhelm, O. Díaz-Molina, O. Sánchez-Zamora, and R.E. Carande, 2008, Space geodetic imaging of rapid ground subsidence in Mexico City. Geological Society of America Bulletin, volume 120, number 11-12, pages 1556-1566.

Carpenter, M.C., 1993, Earth-fissure movements associated with fluctuations in ground-water levels near the Picacho Mountains, south-central Arizona, 1980-84. United States Geological Survey, Professional Paper, series 497, chapter H, 49 pages.

Carréon-Freyre, D., M. Cerca, R. Gutierrez-Calderon, and M.H.L. de Guevara, 2010, Monitoring of land subsidence and fracturing in Iztapalapa, Mexico City, *in*, Land Subsidence, Associated Hazards and the Role of Natural Resources Development, editors, D. Carréon-Freyre, M. Cerca, and D.L. Galloway. International Association for Hydro-Environment Engineering and Research Publication, volume 339, Wallingford, United Kingdom, pages 44–50.

Carreon-Freyre, D., M. Cerca, G. Ochoa-Gonzalez, P. Teatini, and F.R. Zuñiga, 2016, Shearing along faults and stratigraphic joints controlled by land subsidence and hydraulic gradient in the Valley of Queretaro, Mexico. Hydrogeology Journal, volume 24, number 3, pages 657-674.

Castelletto, N., M. Ferronato, G. Gambolati, M. Putti, and P. Teatini, 2008, Can Venice be raised by pumping water underground? A pilot project to help decide. Water Resources Research, volume 44, W01408, doi:10.1029/2007WR006177↗.

Chaussard, E., S. Wdowinski, E. Cabral-Cano, and F. Amelung, 2014, Land subsidence in central Mexico detected by ALOS InSAR time-series. Remote Sensing of the Environment, volume 140, pages 94-106.

Chen, C.T., J.T. Hu, C.Y. Lu, J.C. Lee, and Y.C. Chan, 2007, Thirty-year land elevation change from subsidence to uplift following the termination of groundwater pumping and its geological implications in the Metropolitan Taipei Basin, Northern Taiwan. Engineering Geology, volume 95, pages 30-47.

Chilingarian, G.V., and L. Knight, 1960, Relationship between pressure and moisture content of kaolinite, illite, and montmorillonite clays. American Association of Petroleum Geologists Bulletin, volume 44, pages 101-106.

Cian, F., J.M.D. Blasco, and L. Carrera, 2019, Sentinel-1 for monitoring land subsidence of coastal cities in Africa using PSInSAR: A methodology based on the integration of SNAP and StaMPS. Geosciences, volume 9, page 124; doi:10.3390/geosciences9030124↗.

Colazas, X.C., and R.W. Strehle, 1995, Subsidence in the Wilmington oil field, Long Beach, California, USA, *in*, Subsidence Due to Fluid Withdrawal, editors, G.V. Chilingarian, E.C. Donaldson, and T.F. Yen. Elsevier Science, Amsterdam, Netherlands, pages 285-335.

64

Collins, P.M., 2007, Geomechanical effects on the SAGD process. Society of Petroleum Engineers Reservoir Evaluation and Engineering, volume 10, number 4, pages 367–375.

Comerlati, A., M. Ferronato, G. Gambolati, M. Putti, and P. Teatini, 2004, Saving Venice by sea water. Journal of Geophysical Research, Earth Surface, volume 109, F03006, doi:10.1029/2004JF000119↗.

Conway, B.D., 2014, Land subsidence monitoring. Arizona Department of Water Resources Technical Report 2, Phoenix, Arizona, 35 pages.

Cooper, H.H., Junior., 1966, The equation of groundwater flow in fixed and deforming coordinates. Journal of Geophysical Research, volume 71, number 20, pages 4785–4790.

Da Lio, C., P. Teatini, T. Strozzi, and L. Tosi, 2018, Understanding land subsidence in salt marshes of the Venice Lagoon from SAR Interferometry and ground-based investigations. Remote Sensing of the Environment, volume 205, pages 56-70.

Dang, V.K., C. Doubre, C. Weber, N. Gourmelen, and F. Masson, 2014, Recent land subsidence caused by the rapid urban development in the Hanoi region (Vietnam) using ALOS InSAR data. Natural Hazards and Earth System Science, volume 14, pages 657–674.

DeWiest, R.J.M., 1966, On the storage coefficient and the equations of groundwater flow. Journal of Geophysical Research, volume 71, number 4, pages 1117–1122.

Dong, S., S. Samsonov, H. Yin, and S. Ye., 2014, Time-series analysis of subsidence associated with rapid urbanization in Shanghai, China measured with SBAS InSAR method. Environmental Earth Sciences, volume 72, number 3, pages 677–691.

Du, J., S.J. Brissenden, P. McGillivray, S.J. Bourne, P. Hofstra, E.J. Davis, W.H. Roadarmel, S.L. Wolhart, S. Marsic, R.W. Gusek, C.A. Wright, 2008, Mapping reservoir volume changes during cyclic steam stimulation using tiltmeter-based surface deformation measurements. Society of Petroleum Engineers Reservoir Evaluation and Engineering, volume 11, number 1, pages 63–72.

Ellsworth, W.L., 2013, Injection-induced earthquakes, Science, volume 341, pages 142–147.

Erban, L.E., S.M. Gorelick, and H.A. Zebker, 2014, Groundwater extraction, land subsidence, and sea-level rise in the Mekong Delta, Vietnam. Environmental Research Letters, volume 9, 084010, doi:10.1088/1748-9326/9/8/084010↗.

Ezquerro, P., C. Guardiola-Albert, G. Herrera, J.A. Fernández-Merodo, M. Béjar-Pizarro, and R. Bonì, 2017, Groundwater and subsidence modeling combining geological and multi-satellite SAR data over the Alto Guadalentín aquifer (SE Spain). Geofluids, Article identification document 1359325, doi:10.1155/2017/1359325↗.

Ferretti, A., C. Prati, and F. Rocca, 2001, Permanent scatterers in SAR interferometry. Institute of Electrical and Electronics Engineers Transactions on Geoscience and Remote Sensing, volume 39, number 1, pages 8–20.

Ferretti, A., A. Fumagalli, F. Novali, C. Prati, F. Rocca, and A. Rucci, 2011, A new algorithm for processing interferometric data-stacks: Squee-SAR™. Institute of

65

Electrical and Electronics Engineers Transactions on Geoscience and Remote Sensing, volume 49, number 9, pages 3460–3470.

Ferronato, M., G. Gambolati, C. Janna, and P. Teatini, 2008, Numerical modelling of regional faults in land subsidence prediction above gas/oil reservoirs. International Journal for Numerical and Analytical Methods in Geomechanics, volume 32, pages 633–657.

Ferronato, M., N. Castelletto, G. Gambolati, C. Janna, and P. Teatini, 2013, II cycle compressibility from satellite measurements. Géotechnique, volume 63, number 6, pages 479–486.

Feth, J.H., 1951, Structural reconnaissance of the Red Rock Quadrangle, Arizona. United States Geological Survey Open File Report 51–199, 32 pages.

Finol, A., and Z.A. Sancevic, 1995, Subsidence in Venezuela, *in*, Subsidence Due to Fluid Withdrawal, editors, G.V. Chilingarian, E.C. Donaldson, and T.F. Yen. Elsevier Science, Amsterdam, Netherlands, pages 337–372.

Freeze, R.A., 2000, Social decision making and land subsidence. *in*, Proceedings of sixth International Symposium on Land Subsidence, volume 1, editors, L. Carbognin, G. Gambolati, and A.I. Johnson. La Garangola Publication, Padova, Italy, pages 353–384.

Fuller, M., 1908, Summary of the controlling factors of Artesian flows, United States Geological Survey, Bulletin 319, 44 pages.

Gabriel, A.K., R.M. Goldstein, and H.A. Zebker, 1989, Mapping small elevation changes over large areas: Differential radar interferometry, Journal of Geophysical Research, volume 94, number B7, pages 9183–9191.

Gabrysch, R.K., and R.J. Neighbors, 2000, Land-surface subsidence and its control in the Houston-Galveston region, *in* Proceedings of sixth International Symposium on Land Subsidence, volume 2, editors, L. Carbognin, G. Gambolati, and A. I. Johnson. La Garangola Publication, Padova, Italy, pages 91–92.

Galloway, D., and F.S. Riley, 1999, San Joaquin Valley, California: Largest human alteration of the Earth's surface, *in*, Land Subsidence in the United States, United States Geological Survey, Circular 1182, editors, D. Galloway, D.R. Jones, and S.E. Ingebritsen. United States Geological Survey, Denver, Colorado, pages 23–34.

Galloway, D.L., and J. Hoffmann, 2007, The application of satellite differential SAR interferometry-derived ground displacements in hydrogeology. Hydrogeology Journal, volume 15, pages 133–154.

Galloway, D., D.R. Jones, and S.E. Ingebritsen, editors, 1999, Land subsidence in the United States. United States Geological Survey, Circular 1182, 177 pages.

Gambolati, G., 1972, Estimate of subsidence in Venice using a one-dimensional model of the subsoil. IBM Journal of Research and Development, volume 16, number 2, pages 130–137.

Gambolati, G., 1973a, Equation for one dimensional vertical flow of groundwater: 1. The rigorous theory. Water Resources Research, volume 9, number 4, pages 1022–1028.

Gambolati, G., 1973b, Equation for one dimensional vertical flow of groundwater: 2. Validity range of the diffusion equation. Water Resources Research, volume 9, number 5, pages 1385–1395.

Gambolati, G., 1974, Second order theory of flow in three dimensional deforming media. Water Resources Research, volume 10, number 6, pages 1217–1228.

Gambolati, G., and R. A. Freeze, 1973, Mathematical simulation of the subsidence of Venice: 1. Theory. Water Resources Research, volume 9, number 3, pages 721–733.

Gambolati, G., P. Gatto, and R. A. Freeze, 1974, Mathematical simulation of the subsidence of Venice: 2. Results. Water Resources Research, volume 10, number 3, pages 563–577.

Gambolati, G., P. Gatto, and G. Ricceri, 1984, Land subsidence due to gas/oil removal in layered anisotropic soils by a finite element model, *in*, Proceedings of the Third International Symposium on Land Subsidence, International Association of Hydrological Sciences Publication, volume 151, editors, A.I. Johnson, L. Carbognin, and L. Ubertini, International Association of Hydrological Sciences, Wallingford, United Kingdom, pages 29–41.

Gambolati, G., G. Ricceri, W. Bertoni, G. Brighenti, and E. Vuillermin, 1991, Mathematical simulation of the subsidence of Ravenna. Water Resources Research, volume 27, number 11, pages 2899–2918.

Gambolati, G., P. Teatini, L. Tomasi, and M. Gonella, 1999, Coastline regression of the Romagna region, Italy, due to sea level rise and natural and anthropogenic land subsidence. Water Resources Research, volume 35, number 1, pages 163–184.

Gambolati, G., P. Teatini, D. Baú, and M. Ferronato, 2000, The importance of poro-elastic coupling in dynamically active aquifers of the Po river basin, Italy. Water Resources Research, volume 36, number 9, pages 2443–2459.

Gambolati, G., P. Teatini, and M. Ferronato, 2005, Anthropogenic land subsidence, *in*, Encyclopedia of Hydrological Sciences, editor, M. G. Anderson. John Wiley and Sons, Chichester, United Kingdom, volume four, chapter 158, pages 2444–2459.

Gambolati, G., and P. Teatini, 2014, Venice Shall Rise Again - Engineered Uplift of Venice Through Seawater Injection. Elsevier Insights, Elsevier, Amsterdam, Netherlands, 100 pages.

Gan, Q., and D. Elsworth, 2014, Thermal drawdown and late-stage seismic-slip fault-reactivation in enhanced geothermal reservoirs, Journal of Geophysical Research - Solid Earth, volume 119, pages 8936–8949.

Geerstma, J., 1973, Land subsidence above compacting oil and gas reservoirs. Journal of Petroleum Technology, volume 25, pages 734–744.

Gebremichael, E., M. Sultan, R. Becker, M. El Bastawesy, O. Cherif, and M. Emil, 2018, Assessing land deformation and sea encroachment in the Nile Delta: A radar interferometric and inundation modeling approach, Journal of Geophysical Research: Solid Earth, volume 123, pages 3208–3224.

Gloe, C.S., 1984, Case history number 9.1. Latrobe Valley, Victoria, Australia, *in,* Guidebook to Studies of Land Subsidence Due to Ground-Water Withdrawal, editor, J. F. Poland. United Nations Educational, Scientific and Cultural Organization, Paris, pages 145–153.

González, P.J., K.F. Tiampo, M. Palano, F. Cannavó, and J. Fernándex, 2012, The 2011 Lorca earthquake slip distribution controlled by groundwater crustal unloading, Nature Geoscience, volume 5, pages 821–825.

Häring, M.O., U. Schanz, F. Ladner, and B.C. Dyer, 2008, Characterization of the Basel 1 enhanced geothermal system, Geothermics, volume 37, pages 469–495.

He, Z., B. Ma, J. Long, H. Zhang, K. Liang, and D. Jiang, 2017, Recent ground fissures in the Hetao basin, Inner Mongolia, China. Geomorphology, volume 295, pages 102–114.

Hermann, R.B., and S.K. Park, 1981, The Denver earthquake of 1967–1968. Bulletin of the Seismological Society of America, volume 71, pages 731–745.

Hermansen, H., H.A. Landa, J.E. Sylte, and L.K. Thomas, 2000, Experiences after 10 years of waterflooding the Ekofisk Field, Norway. Journal of Petroleum Science and Engineering, volume 26, pages 11–18.

Hernandez-Marin, M., and T.J. Burbey, 2010, Controls on initiation and propagation of pumping-induced earth fissures: Insights from numerical simulations. Hydrogeology Journal, volume 18, number 8, pages 1773–1785.

Hernandez-Marin, M., and T.J. Burbey, 2012, Fault-controlled deformation and stress from pumping-induced groundwater flow. Journal of Hydrology, volumes 428–429, pages 80–93.

Hertz, H., 1881, On the contact of elastic solids, Journal für die Reine und Angewandte Mathematik, volume 92, pages 156–171.

Higgins, S.A., I. Overeem, M.S. Steckler, J.P.M. Syvitski, L. Seeber, and S.H. Akhter, 2014, InSAR measurements of compaction and subsidence in the Ganges-Brahmaputra Delta, Bangladesh. Journal of Geophysical Research - Earth Surface, volume 119, pages 1768–1781, doi:10.1002/2014JF003117↗.

Hoffmann, J., H.A. Zebker, D.L. Galloway, and F. Amelung, 2001, Seasonal subsidence and rebound in Las Vegas Valley, Nevada, observed by synthetic aperture radar interferometry. Water Resources Research, volume 37, number 6, pages 1551–1556.

Hoffmann, J., D.L. Galloway, and H.A. Zebker, 2003, Inverse modeling of interbed storage parameters using land subsidence observations, Antelope Valley, California. Water Resources Research, volume 37, number 2, 1031 pages, doi:10.1029/2001WR001252↗.

Holland, A., 2013, Earthquakes triggered by hydraulic fracturing in south-central Oklahoma. Bulletin of the Seismological Society of America, volume 103, pages 1784–1792.

Holzer, T.L., and S.N. Davis, 1976, Earth fissures associated with water-table declines. Geological Society of America Abstract Programs, volume 8, number 6, pages 923–924.

Holzer, T.L., S.N. Davis, and B.E. Lofgren, 1979, Faulting caused by groundwater extraction in southcentral Arizona. Journal of Geophysical Research, volume 84, number B2, pages 603–612.

Holzer, T.L., 1981, Preconsolidation stress of aquifer systems in areas of induced land subsidence. Water Resources Research, volume 17, number 3, pages 693–704.

Holzer, T.L., and D.L. Galloway, 2005, Impacts of land subsidence caused by withdrawal of underground fluids in the United States, *in*, Humans as Geologic Agents, Reviews in Engineering Geology, volume 26, editor, J. Ehlen, W.C. Haneberg, and R.A. Larson. Geological Society of America, Boulder, Colorado, pages 87–99.

Holzer, T.L., and E.H. Pampeyan, 1981, Earth fissures and localized differential subsidence, Water Resources Research, volume 17, number 1, pages 223–227.

Horton, S., 2012, Disposal of hydrofracking waste fluid by injection into subsurface aquifers triggers earthquake swarm in central Arkansas with potential for damaging earthquake. Seismological Research Letters, volume 83, pages 250–260.

Huizar-Álvarez, R., L.M. Mitre-Salazar, S. Marín-Córdova, J. Trujillo-Candelaria, and J. Martínez-Reyes, 2011, Subsidence in Celaya, Guanajuato, Central Mexico: Implications for groundwater extraction and the neotectonic regime. Geofísica Internacional, volume 50, number 3, pages 255–270.

Hung, W-C., C. Hwang, J.C. Liou, Y.S. Lin, and H.L. Yang, 2012, Modeling aquifer-system compaction and predicting land subsidence in central Taiwan. Engineering Geology, volumes 147–148, number 6, pages 78–90.

Hwang, C., W.C. Hung, and C.H. Liu, 2008, Results of geodetic and geotechnical monitoring of subsidence for Taiwan high speed rail operation. Natural Hazards, volume 47, pages 1–16.

Ikeda, H., S. Kunisue, D. Nohara, K. Ooba, and T. Kokubo, 2015, In-situ formation compaction monitoring in deep reservoirs by use of fiber optics, Proceedings of the International Association of Hydrological Sciences, volume 372, pages 393-394, doi:10.5194/piahs-372-393-2015↗.

Ikehara, M.E., S.P. Phillips, 1994, Determination of land subsidence related to groundwater level declines using global positioning system and leveling surveys in Antelope Valley, Los Angeles and Kern Counties, California. United States Geological Survey Water - Resources Investigations Report, series 94-4184.

Ikehara, M.E., S.K. Predmore, and D.J. Swope, 1997, Geodetic network to evaluate historical elevation changes and to monitor land subsidence in Lower Coachella Valley, California, 1996. United States Geological Survey Water-Resources Investigations Report, series 97-4237.

Ingerson, I.M., 1941, The hydrology of the of the Southern San Joaquin Valley, California, and its relation to important water supplies. Transaction AGU, volume 22, number 1, pages 20–45.

Jachens, R.C., and T.L. Holzer, 1979, Geophysical investigations of ground failure related to groundwater withdrawal - Picacho Basin, Arizona. Ground Water, volume 17, number 6, pages 574–585.

Jacob, C.E., 1940, On the flow of water in elastic artesian aquifer, Transaction AGU, volume 21, number 2, pages 574–586.

Jha, B., and R. Juanes, 2014, Coupled multiphase flow and poromechanics: A computational model of pore pressure effects on fault slip and earthquake triggering. Water Resources Research, volume 50, number 5, pages 3776–3808.

Kanamori, H., and D.L. Anderson, 1975, Theoretical basis of some empirical relations in seismology. Bulletin of the Seismological Society of America, volume 65, pages 1073–1095.

Khan, A.S., D.S. Khan, and D.M. Kakar, 2013, Land subsidence and declining water resources in Quetta Valley, Pakistan. Environmental Earth Science, volume 70, pages 2719–2727.

Kim, W.Y., 2013, Induced seismicity associated with fluid injection into a deep well in Youngstown, Ohio. Journal of Geophysical Research - Solid Earth, volume 118, pages 3506-3518.

Leonards, G.A., 1962, Engineering properties of soils, in Foundation Engineering. editor, G. A. Leonards. McGraw-Hill, New York, pages 66–240.

Liu, J., Y. Wang, Y. Lu, J. Wei, and D. Kanungo, 2017, Application of distributed optical fiber sensing technique in monitoring the ground deformation. Journal of Sensors, article number 6310197, doi:10.1155/2017/6310197↗.

Lofgren, B.E., and R.L. Klausing, 1969, Land subsidence due to groundwater withdrawal-Tulare Wasco area, California. United States Geological Survey paper 437-B.

Lofgren, B.E., 1971, Significant role of seepage stresses in compressible aquifer systems, EoS Transaction AGU, volume 52, number 11, page 832.

Lohaman, S.W., 1961, Compression of elastic artesian aquifers, United States Geological Survey Professional Paper, series 424-B, pages B47–B49.

Mahmoudpour, M., M. Khamehchiyan, M.R. Nikudel, and M.R. Ghassemi, 2013, Characterization of regional land subsidence induced by groundwater withdrawals in Tehran, Iran. Geopersia, volume 3, number 2, pages 49–62.

Maltman, A., editor, 1994, The Geological Deformation of Sediments. Springer Science and Business Media, Dordrecht.

Mazzoldi, A., A.P. Rinaldi, A. Borgia, and J. Rutqvist, 2012, Induced seismicity within geological carbon sequestration projects: Maximum earthquake magnitude and leakage potential from undetected faults. International Journal of Greenhouse Gas Control, volume 10, pages 434-442.

Meinzer, O.E., and H.A. Hard, 1925, The artesian-water supply of the Dakota Sandstone in the North Dakota with special reference to the Edgeley quadrangle. United States Geological Survey Water-Supply Paper, series 520-E, pages 73–95.

70

Meinzer, O.E., 1928, Compressibility and elasticity of artesian aquifers. Economic Geology, volume 23, number 3, pages 263–291.

Miller, M.M., and M. Shirzaei, 2015, Spatiotemporal characterization of land subsidence and uplift in Phoenix using InSAR time series and wavelet transforms. Journal of Geophysical Research - Solid Earth, volume 120, pages 5822-5842, doi:10.1002/2015JB012017↗.

Ng, A.H.M., L. Ge, X. Li, H.Z. Abidin, H. Andreas, and K. Zhang, 2012, Mapping land subsidence in Jakarta, Indonesia using persistent scatterer interferometry (PSI) technique with ALOS PALSAR. International Journal of Applied Earth Observation and Geoinformation, volume 18, pages 232–242.

Ortiz-Zamora, D., and A. Ortega-Guerrero, 2010, Evolution of long-term land subsidence near Mexico City: Review, field investigations, and predictive simulations. Water Resources Research, volume 46, W01513, doi:10.1029/2008WR007398↗.

Pacheco, J., J. Arzate, E. Rojas, M. Arroyo, V. Yutsis, and G. Ochoa, 2006, Delimitation of ground failure zones due to land subsidence using gravity data and finite element modeling in the Queretaro valley, Mexico. Engineering Geology, volume 86, pages 143–160.

Paris, A., P. Teatini, S. Venturini, G. Gambolati, and A.G. Bernstein, 2010, Hydrological effects of bounding the Venice (Italy) industrial harbour by a protection cut-off wall: A modeling study. Journal of Hydrologic Engineering, volume 15, number 11, pages 882-891.

Pepe, A., and F. Calò, 2017, A review of interferometric Synthetic Aperture RADAR (InSAR) multi-track approaches for the retrieval of Earth's surface displacements. Applied Sciences, volume 7, page 1264, doi:10.3390/app7121264↗.

Phien-wej, N., P.H. Giao, and P. Nutalaya, 2006, Land subsidence in Bangkok, Thailand. Engineering Geology, volume 82, pages 187–201.

Pierce, R.L., 1970, Reducing land subsidence in the Wilmington Oil field by use of saline waters. Water Resources Research, volume 6, number 5, pages 1505–1514.

Poland, J.F., and G.H. Davis, 1969, Land subsidence due to withdrawal of fluids, in, Reviews in Engineering Geology, volume 2, editor, D.J. Varnes, and G. Kiersch. Geological Society of America, Boulder, Colorado, pages 187–269.

Poland, J.F., editor, 1984, Guidebook to Studies of Land Subsidence Due to Groundwater Withdrawal. United Nations Educational, Scientific and Cultural Organization, Paris, 305 pages.

Poland, J.F., and B.E. Lofgren, 1984, San Joaquin valley, California, U.S.A., in Guidebook to Studies of Land Subsidence Due to Groundwater Withdrawal, editor, J. F. Poland. United Nations Educational, Scientific and Cultural Organization, Paris, pages 263–277.

Pratt, W.E., and D.W. Johnson, 1926, Local subsidence of the Goose Creek oil field, Journal of Geology, volume 34, number 7, Part 1, pages 577–590.

Qu, F., Q. Zhang, Z. Lu, C. Zhao, C. Yang, and J. Zhang, 2014, Land subsidence and ground fissures in Xian, China 2005–2012 revealed by multi-band InSAR time-series analysis. Remote Sensing of the Environment, volume 155, pages 366–376.

Raffensperger, J.P., and R.E. Ferrell Jr., 1991, An empirical model of intrinsic permeability in reactive clay-bearing sands. Water Resources Research, volume 27, number 11, pages 2835-2844.

Rappleye, H.S., 1933, Recent areal subsidence found in releveling. Engineering News-Record, volume 110, page 848.

Raspini, F., C. Loupasakis, D. Rozos, and S. Moretti, 2013, Advanced interpretation of land subsidence by validating multi-interferometric SAR data: The case study of the Anthemountas basin (Northern Greece). Natural Hazards and Earth System Science, volume 13, pages 2425–2440.

Riley, F.S., 1986, Developments in borehole extensometry, *in,* Proceedings of the 3rd International Symposium on Land Subsidence. International Association of Hydrological Sciences Publication, volume 151, editors, Arnold Ivan Johnson, Laura Carbognin, and Lucio Ubertini. International Association of Hydrological Sciences, Wallingford, United Kingdom, pages 169–186.

Rintoul, W., 1981, The case of disappearing land, *in,* Drilling Ahead: Tapping California's Richest Oil Field, Valley Publishers, Santa Cruz, California, pages 116–137.

Rivera, A., E. Ledoux, and G. de Marsily, 1991, Nonlinear modeling of groundwater flow and total subsidence of the Mexico City aquifer-aquitard system, *in,* Proceedings of 4th International Symposium on Land Subsidence, International Association of Hydrological Sciences Publication, volume 200, editor, A. I. Johnson. International Association of Hydrological Sciences, Wallingford, United Kingdom, pages 44–58.

Schenato, L., 2017, A review of distributed fibre optic sensors for geo-hydrological applications. Applied Sciences, volume 7, page 896; doi:10.3390/app7090896↗.

Schenato, L., L. Palmieri, M. Camporese, S. Bersan, S. Cola, A. Pasuto, A. Galtarossa, P. Salandin, and P. Simonini, 2017, Distributed optical fibre sensing for early detection of shallow landslides triggering. Scientific Reports, volume 7, article number 14686, doi:10.1038/s41598-017-12610-1↗.

Schmidt, D.A., and R. Burgmann, 2003, Time dependent land uplift and subsidence in the Santa Clara Valley, California, from a large InSAR data set. Journal of Geophysical Research - Solid Earth, volume 108, number B9, page 2416, doi:10.1029/2002JB002267↗.

Schultz, R., R. Wang, Y.J. Gu, K. Haug, and G. Atkinson, 2017, A seismological overview of the induced earthquakes in the Duvernay play near Fox Creek, Alberta. Journal of Geophysical Research - Solid Earth, volume 122, pages 492–505.

Segall, P., and S.D. Fitzgerald, 1996, A note on induced stress changes in hydrocarbon and geothermal reservoirs. Tectonophysics, volume 289, pages 117–128.

Shau, P., and P.K. Sikdar, 2011, Threat of land subsidence in and around Kolkata City and East Kolkata Wetlands, West Bengal, India. Journal of Earth System Science, volume 120, number 3, pages 435–446.

Sheng, Z., and D.C. Helm, 1998, Multiple steps of earth fissuring caused by ground-water withdrawal, *in,* Current Research and Case Studies: Proceedings of the Joseph F. Poland Symposium on Land Subsidence, editor, J. Borchers. Star Publishing Company, Belmont, California, pages 229–238.

Sheng, Z., D.C. Helm, and J. Li, 2003, Mechanisms of earth fissuring caused by groundwater withdrawal. Environmental Engineering and Geoscience, volume 9, number 4, pages 313-324.

Shi, X., Y. Xue, S. Ye, J. Wu, Y. Zhang, and J. Yu, 2007, Characterization of land subsidence induced by groundwater withdrawals in Su-Xi-Chang area, China. Environmental Geology, volume 52, number 1, pages 27–40.

Sreng, S.L., H. Sugiyama, T. Kusaka, and M. Saitoh, 2011, Upheaval phenomenon in clay ground induced by rising groundwater level. Poromechanics, DEStech Publications, Lancaster, Pennsylvania, volume 4, pages 196–203.

Stancliffe, R.P.W., and M.W.A. van der Kooij, 2001, The use of satellite-based radar interferometry to monitor production activity at the Cold Lake heavy oil field, Alberta, Canada. American Association of Petroleum Geologists Bulletin, volume 85, number 5, pages 781–793.

Taylor, D.W., 1948, Fundamentals of Soil Mechanics. John Wiley, New York, 700 pages.

Teatini, P., N. Castelletto, M. Ferronato, G. Gambolati, C. Janna, E. Cairo, D. Marzorati, D. Colombo, A. Ferretti, A. Bagliani, F. Bottazzi, 2011a, Geomechanical response to seasonal gas storage in depleted reservoirs: A case study in the Po River basin, Italy. Journal of Geophysical Research – Earth Surface, volume 116, F02002, doi:10.1029/2010JF001793↗.

Teatini, P., N. Castelletto, M. Ferronato, G. Gambolati, and L. Tosi, 2011c, A new hydrogeological model to predict anthropogenic Venice uplift. Water Resources Research, volume 47, W12507, doi:10.1029/2011WR010900↗.

Teatini, P., N. Castelletto, and G. Gambolati, 2014, 3D geomechanical modelling for CO_2 geological storage: A case study in an offshore northern Adriatic reservoir, Italy. International Journal of Greenhouse Gas Control, volume 22, pages 63–76.

Teatini, P., M. Ferronato, G. Gambolati, and M. Gonella, 2006, Groundwater pumping and land subsidence in the Emilia-Romagna coastland, Italy: Modeling the past occurrence and the future trend. Water Resources Research, volume 42, W01406, doi:10.1029/2005WR004242↗.

Teatini, P., G. Gambolati, M. Ferronato, T. Settari, and D. Walters, 2011b, Land uplift due to fluid injection. Journal of Geodynamics, volume 51, pages 1–16.

Teatini, P., L. Tosi, and T. Strozzi, 2012, Comment on "Recent subsidence of the Venice Lagoon from continuous GPS and interferometric synthetic aperture radar" by Y.

Bock, S. Wdowinski, A. Ferretti, F. Novali, and A. Fumagalli. Geochemistry, Geophysics, Geosystems, volume 13, Q07008, doi:10.1029/2012GC004191↗.

Teatini, P., L. Tosi, T. Strozzi, L. Carbognin, U. Wegmüller, and F. Rizzetto, 2005, Mapping regional land displacements in the Venice coastland by an integrated monitoring system. Remote Sensing of the Environment, volume 98, number 4, pages 403-413.

Terzaghi, K., 1923, Die berechnung der durchlassigkeitsziffer des tones aus dem verlauf der hidrodynamichen span-nungserscheinungen akademie der wissenschaften in wien. Mathematish-Naturwissen-Schaftiliche Klasse, volume 132, pages 125-138.

Terzaghi, K., and R.B. Peck, 1948, Soil Mechanics in Engineering Practice, John Wiley, New York, 566 pages.

Teufel, L.W., D.W. Rhett, and H.E. Farrell, 1991, Effect of reservoir depletion and pore pressure drawdown on in situ stress and deformation in the Ekofisk field, North Sea, *in*, the thirty--second United States Symposium on Rock Mechanics, editor, J.C. Roegiers. American Rock Mechanics Association paper 91-063.

The Royal Society and the Royal Academy of Engineering, 2012, Shale Gas Extraction in the UK: A Review of Hydraulic Fracturing. London, United Kingdom, https://www.raeng.org.uk/publications/reports/shale-gas-extraction-in-the-uk↗.

Theis, C.V., 1935, The relationship between the lowering of the piezometric surface and the rate and duration of discharge of a well using groundwater storage. Transaction American Geophysical Union, volume 16, pages 519–524.

Thu, T.M., and D.G. Fredlund, 2000, Modelling subsidence in the Hanoi City area, Vietnam. Canadian Geotechnical Journal, volume 37, pages 621–637.

Todd, D.K., 1960, Groundwater Hydrology. second edition, John Wiley, New York, 552 pages.

Tokunaga, T., 2008, Groundwater potential in the central district of Tokyo, *in*, Groundwater Management in Asian Cities - Technology and Policy for Sustainability, editor, S. Takizawa. Springer, pages 61–78.

Tosi, L., P. Teatini, L. Carbognin, and J. Frankenfield, 2001, A new project to monitor land subsidence in the Northern Venice coastland (Italy). Environmental Geology, volume 52, pages 889-898.

Tosi, L., C. Da Lio, T. Strozzi, and P. Teatini, 2016, Combining L- and X-band SAR Interferometry to assess ground displacements in heterogeneous coastal environments: The Po River Delta and Venice Lagoon, Italy. Remote Sensing, volume 8, page 308, doi:10.3390/rs8040308↗.

USEPA, 2002, Technical program overview: Underground control regulations, United States Environmental Protection Agency Technical Report 816-R-02-025, Washington, District of Columbia, 81 pages.

van Thienen-Visser, K., and J.N. Breunese, 2015, Induced seismicity of the Groningen gas field: History and recent developments. The Leading Edge, June, pages 664–671, doi:10.1190/tle34060664.1↗.

Vasco, D.W., A. Rucci, A. Ferretti, A. Novali, R.C. Bissell, P.S. Ringrose, A.S. Mathieson, and I.W. Right, 2010, Satellite-based measurements of surface deformation reveal flow associated with the geological storage of carbon dioxide. Geophysical Research Letters, volume 37, L03303, doi:10.1029/2009GL041544↗.

Verruijt, A., 1969, Elastic storage of aquifers, *in*, Flow Through Porous Media, editor, R. De Wiest. Academic Press, New York, pages 331–376.

Ye, S., Y. Xue, J. Wu, and Q. Li, 2012, Modeling visco-elastic-plastic deformation of soil with modified Merchant model. Environmental Earth Sciences, volume 66, number 5, pages 1497-1504.

Ye, S., Y. Luo, J. Wu, X. Yan, H. Wang, X. Jiao, and P. Teatini, 2016, Three-dimensional modeling of land subsidence in Shanghai, China. Hydrogeology Journal, volume 24, number 3, pages 695-709.

Ye, S., A. Franceschini, Y. Zhang, C. Janna, X. Gong, J. Yu, and P. Teatini, 2018, A novel approach to model earth fissure caused by extensive aquifer exploitation and its application to the Wuxi case, China. Water Resources Research, volume 54, doi:10.1002/2017WR021872↗.

Yi, L., F. Zhang, H. Xu, S. Chen, W. Wang, and Q. Yu, 2011, Land subsidence in Tianjin, China. Environmental Earth Sciences, volume 62, pages 1151–1161.

Yu, J., Z. Li, and J. Wu, 2009, Land subsidence in the Changzhou-Wuxi region mapped by InSAR/GPS integration approach. Progress in Natural Science, volume 19, number 11, pages 1267–1271.

Yu, J., G. Wang, T.J. Kearns, and L. Yang, 2014, Is there deep-seated subsidence in the Houston-Galveston area? International Journal of Geophysics, volume 2014, number 11, doi:10.1155/2014/942834↗.

Wang, G.Y., G. You, and B. Shi, 2009, Earth fissures triggered by groundwater withdrawal and coupled by geological structures in Jiangsu Province, China. Environmental Geology, volume 57, number 5, pages 1047–1054.

Wegmüller, U., C. Werner, T. Strozzi, and A. Wiesmann, 2004, Multitemporal interferometric point target analysis, *in* Analysis of Multi-Temporal Remote Sensing Images, Series Remote Sensing, volume 3, editors, P. Smits and L. Bruzzone. World Science, Hoboken, New Jersey, pages 136–144.

Wu, J., X. Shi, S. Ye, Y. Xue, Y. Zhang, Z. Wei, and Z. Fang, 2010, Numerical simulation of viscoelastoplastic land subsidence due to groundwater overdrafting in Shanghai, China. Journal of Hydrologic Engineering, volume 15, number 3, pages 223–236.

Wu, J., H. Jiang, J. Su, B. Shi, Y. Jiang, and K. Gu, 2015, Application of distributed fiber optic sensing technique in land subsidence monitoring. Journal of Civil and Structure Health Monitoring, volume 5, pages 587–597.

Xue, Y., Y. Zhang, S. Ye, J. Wu, and Q. Li, 2005, Land subsidence in China. Environmental Geology, volume 48, number 6, pages 713–720.

Zaman, M.M., A. Abdulraheem, and J.C. Roegiers, 1995, Reservoir compaction and surface subsidence in the North Sea Ekofisk field, *in* Subsidence Due to Fluid

75

Withdrawal, editors, E.C. Donaldson, G.V. Chilingarian, and T.F. Yen. Elsevier Science, Amsterdam, Netherlands, pages 373–423.

Zanello, F., P. Teatini, M. Putti, and G. Gambolati, 2011, Long term peatland subsidence: Experimental study and modeling scenarios in the Venice coastland. Journal of Geophysical Research - Earth Surface, volume 116, F04002, doi:10.1029/2011JF002010↗.

Zhang, Y., H. Gong, Z. Gu, R. Wang, X. Li, and W. Zhao, 2014, Characterization of land subsidence induced by groundwater withdrawals in the plain of Beijing city, China. Hydrogeology Journal, volume 22, number 2, pages 397–409.

Zhang, Y., J. Wu, Y. Xue, Z. Wang, Y. Yao, X. Yan, and H. Wang, 2015, Land subsidence and uplift due to long-term groundwater extraction and artificial recharge in Shanghai, China. Hydrogeology Journal, volume 23, pages 1851–1866.

Zhao, C., X. Ding, Q. Zhang, Z. Lu, and Z. Li, 2008, Monitoring of recent land subsidence and ground fissures in Xian with SAR interferometry. The International Archives of the Photogrammetry, Remote Sensing and Spatial Information Sciences, volume 37, part B1, pages 147–150.

Zhu, L., H. Gong, X. Li, R. Wang, B. Chen, Z. Dai, and P. Teatini, 2015, Land subsidence due to groundwater withdrawal in the northern Beijing plain, China. Engineering Geology, volume 193, number 2, pages 243-255, doi:10.1016/j.enggeo.2015.04.020↗.

Zhu, H.H., B. Shi, and C.C., Zhang, 2017, FBG-based monitoring of geohazards: current status and trends. Sensors, volume 17, page 452; doi:10.3390/s17030452↗.

Ziaie, A., K. Kumarci, A.R. Ghanizadeh, and A. Mahmodinejad, 2009, Prediction of earth fissures development in Sirjan. Research Journal of Environmental Science, volume 3, number 4, pages 486–496.

Zimmerman, R., 1991, Compressibility of sandstones. Developments in Petroleum Science, volume 29, Elsevier, Amsterdam, Netherlands, 183 pages.

Zoback, M.D., 2007, Reservoir Geomechanics. Cambridge University Press, Cambridge, United Kingdom, 452 pages.

10 Boxes

Box 1 Justification of Terzaghi's Principle

To justify Equation 3, namely that $\Sigma\, A_i \ll 1$, we can provide the following rough calculation. Assume the solid grains are spherical with radius r. According to Hertz's theory (Hertz, 1881), the contact area A' of two spheres pressed by the force P reads:

$$A' = 1.23\pi\left(0.5\frac{Pr}{E_r}\right)^{2/3} \tag{Box 1-1}$$

with E_r the sphere Young modulus (which reflects the stiffness of a solid as the ratio of its tensile stress and axial strain, $ML^{-1}T^{-2}$). Let's take a representative porous medium depth (250 m) and spheres radius equal to, $r = 0.5$ mm, and assume full saturation. Considering the buoyant force exerted by water the weight P of a grain column of height h is:

$$P = \frac{h}{2r}\gamma'\frac{4}{3}\pi r^3 \tag{Box 1-2}$$

where:

γ' = specific weight of the spheres minus the upward buoyant force

Using Equation Box 1-2, A' above becomes Equation Box 1-3:

$$A' = 1.23\pi r^2\left(\frac{\pi h\gamma'}{3E_r}\right)^{2/3} \tag{Box 1-3}$$

Setting $h = 250$ m, γ' 1.7×10^4 N/m^3 (N is a Newton, the SI unit of force [MLT^{-2}], and 1 N is equal to 1 kg m s^{-2}) and $E_r = 1\times10^{11}$ N/m^2 (corresponding to a volumetric grain compressibility $c_{b,r} = 0.16\times10^{-10}$ m^2/N and a grain Poisson ratio $v_r = 0.25$, being:

$$c_{b,r} = 3\frac{1 - 2v_r}{E_r}$$

we obtain:

$$A' = 1.23\,\pi\,(0.5\text{ mm})^2\left(\frac{\pi}{3}\frac{250\text{ m }1.7x10^4\frac{\text{N}}{\text{m}^3}}{1x10^{11}\frac{\text{N}}{\text{m}^2}}\right)^{2/3} \cong 0.00121\text{ mm}^2$$

that is, equal to 0.121 percent of the horizontal projection area of the spheres (equal to 1 mm^2). Hence the assumption that $\Sigma\, A_i \ll 1$ is fully warranted.

[Return to where text linked to Box 1](#)↥

Box 2 Visualization of Relationship between Effective Stress and Void Ratio

To visualize the relationship between compaction and void ratio presented in Figure 2, which is repeated here for the readers convenience, it is useful to view abstract version of Figure 2. In the abstract version (Figure Box 2-1) in which all solids are grouped with no pore space, and all pore space occupies the remainder of the volume, with example values are assigned, as illustrated in Figure Box 2-1. The total compaction η of a layer as illustrated in Figure 2, with initial thickness s_0 and initial void ratio e_0 is completely due to reduced pore space as reflected by Equation 4 (repeated here for the readers convenience).

$$\eta = \Delta z \frac{\Delta e}{1 + e_0} \qquad \text{(repeat of Equation 4)}$$
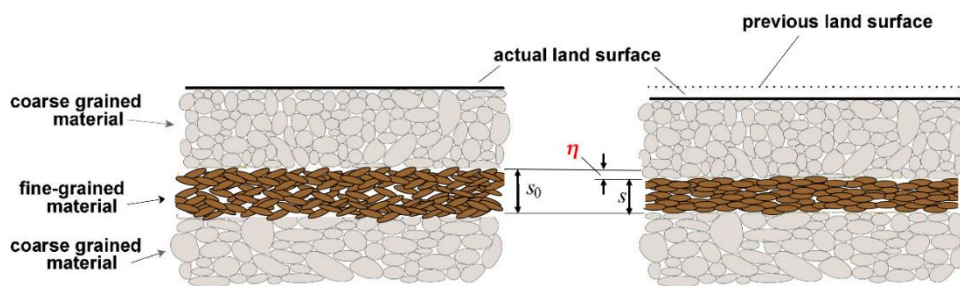
Repeat of Figure 2 for the reader's convenience - Soil compaction η with a reduction of the porous space (grains are incompressible for all practical purposes).
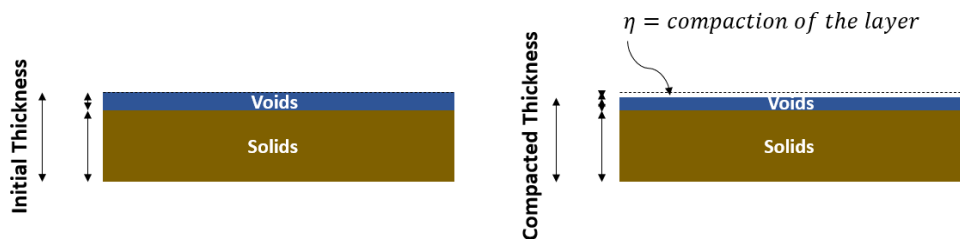

Figure Box 2-1 - Abstract representation of the fine-grained layer of Figure 2 in which all solids are grouped with no pore space, all pore space occupies the remainder of the volume.

$$\eta = s_0 \frac{\Delta e}{1 + e_0} = 30 \text{ m} \frac{0.0625}{1 + 0.25} = 1.5 \text{ m}$$

$$e_{before\ compaction} = \frac{Vv}{Vs} = \frac{0.2}{0.8} = 0.25$$

$$e_{after\ compaction} = \frac{Vv}{Vs} = \frac{0.15}{0.8} = 0.1875$$
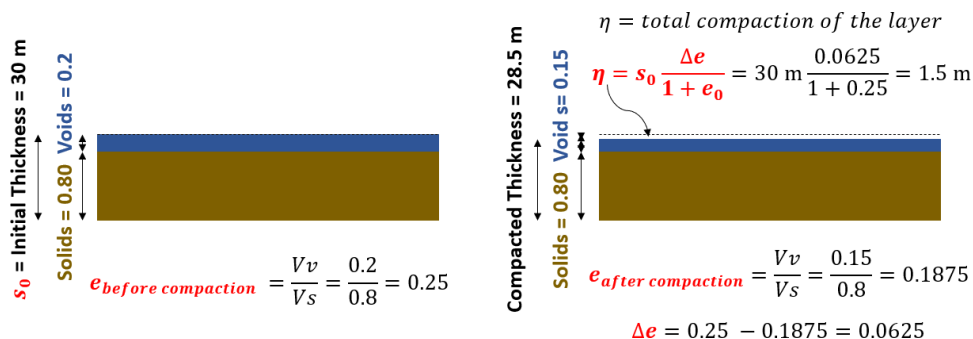
$$\Delta e = 0.25 - 0.1875 = 0.0625$$

Figure Box 2-2 - Soil compaction η illustrated using the abstract example of the fine-grained material shown in Figure Box 2-1 with example values assigned to the pertinent parameters.

78

Calculation of the change in effective stress for a decline in the piezometric level from A to B at a point within an unconfined aquifer as shown in Figure 13, is illustrated in Figure Box 2-3 and Figure Box 2-4.
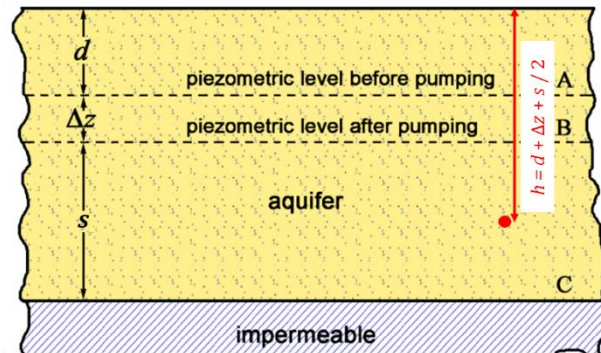
For piezometric level A the effective stress at ● is (Equation 9)

σ_{zA} = weight of overlying solids $(1-\phi) \; \gamma'(d+\Delta z+s/2)$

     reduced by the bouyancy of the saturated overlying solids $- (1-\phi) \; \gamma(\Delta z+s/2)$

     plus the weight of the moisture in the unsaturated zone $+ \; \gamma\theta_w d$

When the piezometric level declines to B the effective stress at ● is

σ_{zB} = weight of overlying solids $(1-\phi) \; \gamma'(d+\Delta z+s/2)$

     reduced by the bouyancy of the saturated overlying solids $- (1-\phi) \; \gamma(s/2)$

     plus the weight of the moisture in the unsaturated zone $+ \; \gamma\theta_w (d+\Delta z)$

Blue terms show the different thicknesses pertinent to calculating the effective stress for the different piezometric levels resulting in

$$\Delta\sigma_{z(AtoB)} = \gamma\Delta z \; (1 - \phi + \theta_w) \text{ (Equation 8)}$$

Figure Box 2-3 - Presentation of Equations 8 and 9 in words.

Assume the following values
d = 18 m Δz = 9 m s = 32 m
Φ = 0.2 Θ = 0.04 γ' = 2650 kg/m^3 γ = 1000 kg/m^3

For piezometric level A the effective stress at ● is

σ_{zA} = weight of overlying solids $(1-0.2) \; 2650 \; \frac{kg}{m^3} \; (18 \text{ m} + 9 \text{ m} + \frac{32}{2} \text{ m})$

     reduced by the bouyancy of the saturated overlying solids $- (1-0.2) \; 1000 \; \frac{kg}{m^3} \; (9 \text{ m} + \frac{32}{2} \text{ m})$

     plus the weight of the moisture in the unsaturated zone $+ 1000 \; \frac{kg}{m^3} \; 0.04 \; (18 \text{ m})$

$= 71,880 \; \frac{kg}{m^2}$

When the piezometric level declines to B the effective stress at ● is

σ_{zB} = weight of overlying solids $(1-0.2) \; 2650 \; \frac{kg}{m^3} \; (18 \text{ m} + 9 \text{ m} + \frac{32}{2} \text{ m})$

     reduced by the bouyancy of the saturated overlying solids $- (1-0.2) \; 1000 \; \frac{kg}{m^3} \; (\frac{32}{2} \text{ m})$

     plus the weight of the moisture in the unsaturated zone $+ 1000 \; \frac{kg}{m^3} \; 0.04 \; (18 \text{ m} + 9 \text{ m})$

$= 79,440 \; \frac{kg}{m^2}$

$\sigma_{zB} - \sigma_{zA} = 7560 \; \frac{kg}{m^2}$

CHECK: $\Delta\sigma_{z(AtoB)} = 1000 \; \frac{kg}{m^3} \; 9 \text{ m} \; (1 - 0.2 + 0.04 \;) = 7560 \; \frac{kg}{m^2}$

Figure Box 2-4 - Worked example of calculating effective stress.

79

Box 3 3-D Poroelasticity Equations

Theoretically, land subsidence is best analyzed according to the theory of consolidation (Biot, 1941), which holds that consolidation itself represents the response of a compressible porous medium to changes in the flow field operating within it. A complete analysis of land subsidence requires determination of the 3-D deformation field accompanying the 3-D flow field, and must be accomplished in a complex multi-aquifer system. A few basic principles underlie the consolidation process. As outlined above, the first principle advanced by Terzaghi (1923) states that the total stress σ_{tot} at any point of the porous medium is equal to the sum of the effective intergranular σ_{eff} and the neutral pore pressure p:

$$\sigma_{tot} = \sigma_{eff} + p$$

Deformation of the porous body is controlled exclusively by variation of the effective stress σ_{eff}. If we consider changes relative to an initial undisturbed state of equilibrium, the Cauchy equations of equilibrium are cast in terms of incremental effective stress and pore pressure as shown in Equation Box 3-1.

$$\frac{\partial \sigma_{xx}}{\partial x} + \frac{\partial \tau_{xy}}{\partial y} + \frac{\partial \tau_{xz}}{\partial z} = \frac{\partial p}{\partial x}$$
$$\frac{\partial \tau_{yx}}{\partial x} + \frac{\partial \sigma_{yy}}{\partial y} + \frac{\partial \tau_{yz}}{\partial z} = \frac{\partial p}{\partial y} \qquad \text{(Box 3-1)}$$
$$\frac{\partial \tau_{zx}}{\partial x} + \frac{\partial \tau_{zy}}{\partial y} + \frac{\partial \sigma_{zz}}{\partial z} = \frac{\partial p}{\partial z}$$

where:

σ_{xx} = incremental normal effective stress in x direction

σ_{yy} = incremental normal effective stress in y direction

σ_{zz} = incremental normal effective stress in z direction

and, the incremental shear stresses:

$\tau_{xy} = \tau_{yx}$
$\tau_{xz} = \tau_{zx}$
$\tau_{yz} = \tau_{zy}$

The relationships between the incremental effective stress tensor σ and the incremental strain tensor ε for a geomechanical isotropic medium are shown in Equation Box 3-2.

$$\begin{bmatrix} \sigma_{xx} \\ \sigma_{yy} \\ \sigma_{zz} \\ \tau_{xy} \\ \tau_{xz} \\ \tau_{yz} \end{bmatrix} = D^{-1} \begin{bmatrix} \varepsilon_{xx} \\ \varepsilon_{yy} \\ \varepsilon_{zz} \\ \varepsilon_{xy} \\ \varepsilon_{xz} \\ \varepsilon_{yz} \end{bmatrix} \qquad \text{(Box 3-2)}$$

with matrix D^{-1} as shown in Equation Box 3-3.

$$D^{-1} = \frac{E}{(1+v)(1-2v)} \begin{bmatrix} 1-v & v & v & 0 & 0 & 0 \\ v & 1-v & v & 0 & 0 & 0 \\ v & v & 1-v & 0 & 0 & 0 \\ 0 & 0 & 0 & \dfrac{1-2v}{2} & 0 & 0 \\ 0 & 0 & 0 & 0 & \dfrac{1-2v}{2} & 0 \\ 0 & 0 & 0 & 0 & 0 & \dfrac{1-2v}{2} \end{bmatrix} \quad \text{(Box 3-3)}$$

where:

E = Young's modulus (stiffness of a solid as the ratio of its tensile stress and axial strain, ML^{-1}T^{-2})

v = Poisson's ratio (reflects deformation of a solid in the direction perpendicular to loading, the negative ratio of transverse strain to axial strain, dimensionless)

Typically, in layered aquifer systems laid down in a depositional environment, the geomechanical properties along the vertical direction (v) are different from those in a horizontal direction (h). The geomechanical properties of a transversally isotropic porous medium are fully described by five independent parameters E_v, E_h, v_v, E_h, G_v, with G the shear modulus. G_h is dependent on E_h and v_h through Equation Box 3-4.

$$G_h = \frac{E_h}{2(1-v_h)} \quad \text{(Box 3-4)}$$

Thermodynamic consistency requires the positive definiteness of matrix C^{-1} relating the stress tensor to the strain tensor, which implies (Ferronato et al., 2013):

$$1 - v_h^2 > 0 \quad \text{and} \quad 1 - v_h - 2v_h^2 \frac{E_v}{E_h} > 0$$

then, as shown in Equations Box 3-5, setting,

$$\vartheta = \frac{E_h}{E_v}$$
$$\eta = \frac{E_h}{2(1+v_h)G_v} \quad \text{(Box 3-5)}$$
$$\alpha = \frac{1}{E_v}\left(1 - \frac{2v_v^2}{1-v_h}\frac{E_v}{E_h}\right)$$

the constitutive matrix C^{-1} (equivalent to D^{-1} for a transversally isotropic medium) is Equation Box 3-6 (Ferronato et al., 2013).

$$C^{-1} = \frac{1}{(1-v_h^2)\,\alpha} \begin{bmatrix} C_1^{-1} & 0 \\ 0 & C_2^{-1} \end{bmatrix} \quad \text{(Box 3-6)}$$

where:

$$C_1^{-1} = \begin{bmatrix} \vartheta - v_v^2 & v_v^2 + \vartheta v_h & v_v(1 + v_h) \\ v_v^2 + \vartheta v_h & \vartheta - v_v^2 & v_v(1 + v_h) \\ v_v(1 + v_h) & v_v(1 + v_h) & 1 - v_v^2 \end{bmatrix}$$

$$C_2^{-1} = \frac{\vartheta(1 - v_h) - 2v_v^2}{2} \begin{bmatrix} 1 & 0 & 0 \\ 0 & 1/\eta & 0 \\ 0 & 0 & 1/\eta \end{bmatrix}$$

The coefficient α provided in Equation Box 3-5 is the vertical oedometric compressibility of the medium prevented from expanding laterally (Gambolati et al., 1984). Setting $v_h = v_v$, $E_h = E_v$, and $G_h = G_v$, Equation Box 3-6 becomes Equation Box 3-2 and α becomes Equation Box 3-7.

$$\alpha = \frac{(1 + v)\ (1 - 2v)}{(1 - v)E} \qquad \text{(Box 3-7)}$$

Equation Box 3-7 is the vertical compressibility of an isotropic soil. If we replace the relations between the effective stress and the strain above into the Cauchy equations, we obtain the equilibrium equations for a porous medium subject to internal pore pressure variations, p, written in terms of displacements (isotropic medium) as in Equation Box 3-8.

$$G\nabla^2 u + (\lambda + G)\frac{\partial \varepsilon}{\partial x} = \frac{\partial p}{\partial x}$$

$$G\nabla^2 v + (\lambda + G)\frac{\partial \varepsilon}{\partial y} = \frac{\partial p}{\partial y} \qquad \text{(Box 3-8)}$$

$$G\nabla^2 w + (\lambda + G)\frac{\partial \varepsilon}{\partial z} = \frac{\partial p}{\partial z}$$

where:

u, v, w = components of the incremental position vector along the coordinate axes x, y, and z, respectively

∇^2 = Laplace operator

λ = Lamè constant equal to $vE/[(1 - 2v)\ (1 + v)]$

ε = $\varepsilon_{xx} + \varepsilon_{yy} + \varepsilon_{zz}$, volume strain or dilatation

Similar equations hold for a transversally isotropic medium, not given here, however, because of their greater complexity. There are three equations with four unknowns: u, v, w, and p. The additional equation needed to close the system is provided by the groundwater flow equation that controls subsurface flow within the aquifer.

The flow equation is based on the principle of mass conservation for both solid grains and water. Thus, Darcy's law must be cast in terms of the relative velocity of fluid to grains. Cooper (1966) and Gambolati (1973a) derived the flow equations by assuming a grain velocity different from zero, and worked with material derivatives (total derivatives and substantial derivatives) in the appropriate places in the development. Gambolati (1973b) showed that the grain velocity can be discarded, that is, assumed to be zero, as long as the final soil settlement does not exceed 5 percent of the original aquifer thickness, a condition reached in nearly all applications. DeWiest (1966) took into consideration the

82

dependence of the hydraulic conductivity on the water's specific weight, γ, via the intrinsic permeability and the dependence of γ on the incremental pressure variation. Gambolati (1973b) again showed that the influence of the dependence of γ on the hydraulic conductivity is slight, and can safely be neglected. Later, within this framework, the groundwater flow equation as originally developed by Biot (1941, 1955) was elegantly and clearly derived by Verruijt (1969), and thus the fourth equation to be added to the above Equation Box 3-8 is Equation Box 3-9.

$$\frac{1}{\gamma} \nabla \cdot \left(K_{ij} \nabla p \right) = \phi \beta \frac{\partial p}{\partial t} + \frac{\partial \varepsilon}{\partial t} \qquad \text{(Box 3-9)}$$

where:

∇ = $\partial/\partial x + \partial/\partial y + \partial/\partial z$

K_{ij} = $k_{ij}\gamma/\mu$, hydraulic conductivity tensor with principal components K_{xx}, K_{yy}, and K_{zz}

k_{ij} = intrinsic permeability tensor

μ = viscosity of water

ϕ = medium porosity

β = compressibility of water

Equation Box 3-8 together with Equation Box 3-9 form the mathematical basis of the so-called "coupled" (or Biot) formulation of flow and stress in an isotropic porous medium experiencing groundwater flow. It is the most sophisticated theoretical approach to the simulation of land subsidence in the area of linear elasticity. Gambolati (1974) showed that at any point P of the porous medium, the deformation may be expressed as the sum of two contributing factors: (1) the pointwise deformation caused by the incremental pore pressure acting at P and (2) the deformation caused by the pressure p acting outside P, namely in the remainder of the medium. Gambolati (1974) called the second factor the "three-dimensional effect": it vanishes, of course, in one-dimensional media. The first factor is expressed as:

$$\varepsilon = \frac{1}{E_v} \left(1 - \frac{2v_v^2}{1 - v_h} \frac{E_v}{E_h} \right) p = \alpha p$$

in a geomechanical transversally isotropic medium, and

$$\varepsilon = \frac{(1 + v)\,(1 - 2v)}{(1 - v)E} p = \alpha p$$

in a geomechanical isotropic medium, with α the vertical compressibility previously defined. Replace the above expression for ε in the flow Equation Box 3-9) and you obtain the so-called "uncoupled" formulation of flow and stress. In the uncoupled formulation the flow equation is solved for p independently of the stress equation, with the gradient of the pore pressure variations later integrated into the equilibrium equations (Equation Box 3-8) as a known external source of strength. The uncoupled flow equation is thus Equation Box 3-10.

$$\nabla \cdot \left(K_{ij} \nabla p \right) = \gamma(\alpha + \phi\beta) \frac{\partial p}{\partial t} \qquad \text{(Box 3-10)}$$

Assuming the medium to be transversally isotropic as far as the hydraulic conductivity is concerned as well, having axes coincident with the principal directions of anisotropy, Equation Box 3-10 becomes Equation Box 3-11.

$$\frac{\partial}{\partial x}\left(K_{xx} \frac{\partial p}{\partial x} \right) + \frac{\partial}{\partial y}\left(K_{yy} \frac{\partial p}{\partial y} \right) + \frac{\partial}{\partial z}\left(K_{zz} \frac{\partial p}{\partial z} \right) = S_s \frac{\partial p}{\partial t} \qquad \text{(Box 3-11)}$$

The coefficient $S_s = \gamma(\alpha + \phi\beta)$ is the specific elastic storage coefficient referred to previously. The uncoupled equation has been the basis of classical groundwater hydrology from the very beginning of quantitative hydrogeology's development (for example, Theis, 1935; Jacob, 1940; Todd, 1960; and Bear, 1972), and is still universally used today. The superiority of the coupled approach in predicting land subsidence due to groundwater pumping has been disputed by Gambolati et al. (2000), who showed that the uncoupled pressure solution can be safely used in predicting land subsidence in compacting sedimentary basins, the coupled and uncoupled solutions being virtually indistinguishable at any time of practical interest.

It may also be of interest to mention some basic definitions of oedometer vertical soil compressibility, which is the main rock parameter controlling land subsidence. The definition of α given above is the one derived from the classical theory of elasticity assuming reversible elastic properties of the porous medium. The problem of defining various rock compressibilities is thoroughly discussed by Zimmerman (1991). In the present analysis, we restrict our discussion to the comparison between α as defined above, and the compressibility c_b as is typically defined in geotechnics by Equation Box 3-4). Assume a 1-D soil sample with initial length Δz experiencing a vertical (oedometer) deformation $\delta(\Delta z)$. In the classical elastic theory, the vertical compressibility α is defined as Equation Box 3-12:

$$\alpha = \frac{\delta(\Delta z)}{\Delta z} \frac{1}{p} = \frac{\varepsilon}{p} \qquad \text{(Box 3-12)}$$

where p, equal and opposite to the incremental effective stress, is negative in the sample compaction $\delta(\Delta z)$. Using the void ratio, we can write Equation Box 3-13:

$$\delta(\Delta z) = [\Delta z + \delta(\Delta z)] \frac{e}{1 + e} - \Delta z \frac{e_0}{1 + e_0} \qquad \text{(Box 3-13)}$$

where:

e_0 = initial void ratio prior to compaction (Figure 2)

Equation Box 3-13 assumes that the individual soil grains are incompressible, so that the sample volume $\delta(\Delta z)$ is equal to the variation of the porous volume (Figure 2). By dividing both sides of Equation Box 3-13 by Δz and rearranging, we obtain Equation Box 3-14.

$$\varepsilon = \frac{\delta(\Delta z)}{\Delta z} = \frac{e - e_0}{1 + e_0} \qquad \text{(Box 3-14)}$$

also,

$$\alpha = \frac{\varepsilon}{p} = \frac{e - e_0}{p(1 + e_0)}$$

and if α does not depend on p then Equation Box 3-15 can be written.

$$\frac{de}{dp} = \alpha(1 + e_0) \qquad \text{(Box 3-15)}$$

That is, the void ratio is proportional to the incremental pressure p (for any given initial e_0). Substitution of Equation Box 3-15 into Equation 5 of the main portion of this book, with $dp = -d\,\sigma_z$, leads to:

$$c_b = \alpha\frac{1 + e_0}{1 + e} = \alpha\frac{1 + e_0}{1 + e_0 + \alpha p\,(1 + e_0)} = \frac{\alpha}{1 + \alpha p}$$

Only when the incremental pressure p approaches 0, do α and c_b coincide. In general, the two compressibilities α and c_b are not equal and cannot be considered simultaneously constant. The expression of c_b versus ε is (using Equation Box 3-14) is as shown in Equation Box 3-16.

$$c_b = \frac{1 + e_0}{1 + e}\frac{d\varepsilon}{dp} = \frac{1}{1 + \varepsilon}\frac{d\varepsilon}{dp} \qquad \text{(Box 3-16)}$$

If α is constant and $d\varepsilon/dp = \alpha$ we have Equation Box 3-17.

$$c_b = \frac{\alpha}{1 + \varepsilon} = \frac{\alpha}{1 + \alpha p} \qquad \text{(Box 3-17)}$$

Gambolati (1973b) has shown that the assumption of constant α can be easily removed to give the general correct relationship between α and c_b as in Equation Box 3-18.

$$c_b = \frac{p\dfrac{d\alpha}{dp} + \alpha}{1 + \alpha p} \qquad \text{(Box 3-18)}$$

If c_b is constant, Equation Box 3-18 can be integrated to provide α as expressed in Equation Box 3-19.

$$\alpha = \frac{\exp^{p\,c_b} - 1}{p} \qquad \text{(Box 3-19)}$$

The assumption that the individual grains are incompressible is fully warranted by the fact that the compressibility of any aquifer system is orders-of-magnitude greater than the compressibility of the single grain. Geerstma (1973) provides the value of $\alpha = 1.6\times10^{-6}$ bar[-1] for grains of silicate. In contrast, the compressibility of aquifer systems is, typically, orders-of-magnitude larger than the compressibility of single grains as shown in Figure Box 3-1. Figure Box 3-1 provides an example of the compressibility of an aquifer system in terms of the relationship of α versus depth and vertical effective intergranular stress σ_{zz} in the sedimentary basin of the river Po plain, Italy (Gambolati et al., 1991, 1999;

and Comerlati et al., 2004). However, as long as the ultimate relative compaction αp does not exceed 5 percent of the compacting unit (which is typically the case in geologic formations, particularly in shallow formations), the difference between α and c_b does not exceed 2-3 percent (Gambolati, 1973b, Figure 14) and for practical applications the two definitions are interchangeable.

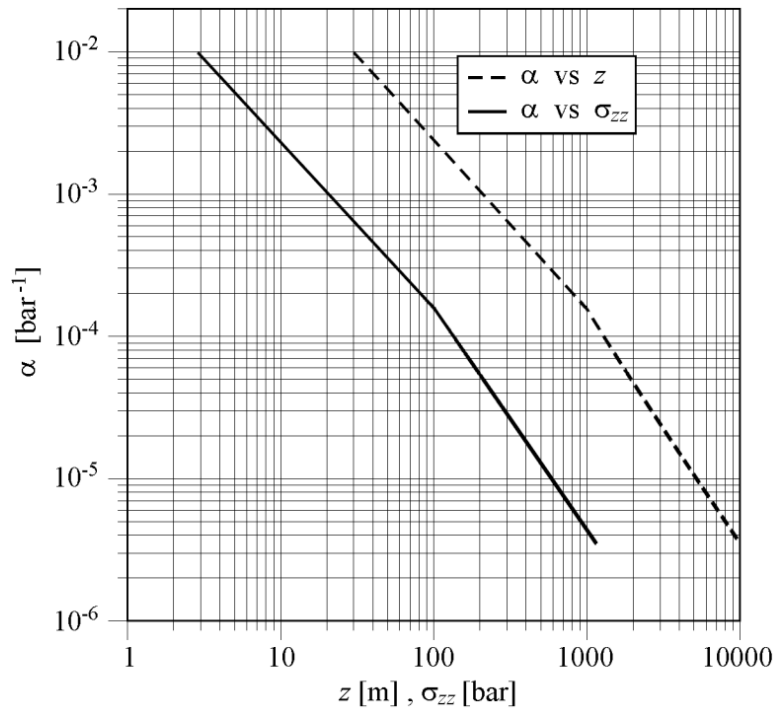**Figure Box 3-1 -** Uniaxial vertical compressibility, α, versus effective stress σ_{zz} and depth z in the Po river plain, Italy (after Comerlati et al., 2004).

Finally, it is worth mentioning that, when comprehensive in situ and lab soil characterizations are available, more realistic constitutive formulations taking into account plastic or viscoplastic behavior may be developed and used for the simulation and prediction of land subsidence in soft under-consolidated alluvial basins (for example, Ye et al., 2012).

Return to where text linked to Box 3↰

86

11   Exercise Solutions

Exercise 1 Solution

Let's denote with $\gamma_w = 1000 \text{ kg/m}^3$ the water specific weight and with $\gamma_{grain} = 2700 \text{ kg/m}^3$ the specific weight of the solid. The specific weight of the saturated clay γ_s can be computed as follows:

$$\gamma_s = \phi\,\gamma_w + (1 - \phi)\gamma_{grain}$$

$$\gamma_s = 0.4\,(1000) + (1 - 0.4)2700 = 2020\ \text{kg/m}^3$$

With a 6 m deep lake, pressure p at 15 m below the lake bottom amounts to

$$p = (6 + 15)\text{ m } 1000\,\frac{\text{kg}}{\text{m}^3} = 21{,}000\,\frac{\text{kg}}{\text{m}^2}$$

Pressure is often reported in bars. There are 9.8067 x 10⁻⁵ bars per $1\frac{\text{kg}}{\text{m}^2}$, so

$$p = 21{,}000\,\frac{\text{kg}}{\text{m}^2} =\ 2.06\text{ bars.}$$

The geostatic stress is:

$$\sigma_c = 6\text{ m } 1000\,\frac{\text{kg}}{\text{m}^3} + 15\text{ m } 2020\,\frac{\text{kg}}{\text{m}^3} = 6000\,\frac{\text{kg}}{\text{m}^2} + 30{,}300\,\frac{\text{kg}}{\text{m}^2} = 36{,}300\,\frac{\text{kg}}{\text{m}^2}$$

$$\sigma_c = 3.56\text{ bar}$$

Rearranging Terzaghi's principle (Equation 3), the effective vertical stress σ_z is equal to:

$$\sigma_z = \sigma_c - p = 3.56\text{ bar} - 2.06\text{ bar} = 1.50\text{ bar}$$

If the water level drops to 4 m, both the pressure and the total vertical stress reduce the same amount (2 m $1000\,\frac{\text{kg}}{\text{m}^3}\,\frac{9.8067\text{ x }10^{-5}\text{ bars}}{1\frac{\text{kg}}{\text{m}^2}} = 0.2$ bar). Hence, σ_z does not vary.

Exercise 2 Solution

Question 1: land subsidence after 1 month

Because of the small hydraulic conductivity, it can reasonably be assumed that pressure depletion has not yet significantly propagated into the aquitard. Therefore, similarly to Equation 13, the total subsidence η_{tot} is the sum of compaction of the phreatic aquifer and the confined aquifer only: $\eta_{tot} = \eta_p + \eta_c$.

The compaction of the phreatic aquifer amounts to $\eta_p \cong t_p\, c_{b,p}\, \Delta\sigma_{z,p}$ with t_p the time-averaged aquifer thickness below the water table (Equation 10). Denoting the porosity with ϕ and the water saturation with θ_w, the effective stress change is given by Equation 7.

$$\Delta\sigma_{z,p} = \gamma_w\, \Delta z_p\, (1 - \phi + \theta_w) = 1000\,\frac{\text{kg}}{\text{m}^3}\; 5\text{ m}\;(1 - 0.35 + 0.10)$$

$$= 1000\,\frac{\text{kg}}{\text{m}^3}\;3.75\text{ m} = 3750\,\frac{\text{kg}}{\text{m}^2}\;\frac{9.8067\times10^{-5}\text{bar}}{\frac{\text{kg}}{\text{m}^2}} = 0.37\text{ bar}$$

Therefore:

$$\eta_p = t_p\, c_{b,p}\, \Delta\sigma_{z,p} = \tfrac{1}{2}(25 + 20)\text{ m}\;\frac{1\times10^{-4}}{\text{bar}}\,0.37\text{ bar} = 0.00083\text{ m} = 0.83\text{ mm}.$$

The compaction of the confined aquifer amounts to:

$$\eta_c = b_c\, c_{b,c}\, \gamma_w\left(\Delta z_c - \Delta z_p(\phi - \theta_w)\right)$$

$$\eta_c = 50\text{ m}\;\frac{2\times10^{-5}}{\text{bar}}\left(\left(1000\,\frac{\text{kg}}{\text{m}^3}(25\text{ m} - 5\,m\,(0.35 - 0.1))\right)\frac{9.8067\times10^{-5}\text{bar}}{\frac{\text{kg}}{\text{m}^2}}\right)$$

$$\eta_c = 50\text{ m}\;\frac{2\times10^{-5}}{\text{bar}}\left(1000\,\frac{\text{kg}}{\text{m}^3}(23.75\text{ m})\frac{9.8067\times10^{-5}\text{bar}}{\frac{\text{kg}}{\text{m}^2}}\right)$$

$$\eta_c = 50\text{ m}\;\frac{2\times10^{-5}}{\text{bar}}\;(2.33\text{ bar })$$

$$\eta_c = 0.00233\text{ m} = 2.33\text{ mm}$$

Hence: $\eta_{tot} = 0.83 + 2.33 = 3.16$ mm

Question 2: land subsidence after 10 years

In this case, aquitard compaction contributes to land subsidence $\eta_{tot} = \eta_p + \eta_{aqt} + \eta_c$. After a period of 10 years, it can be assumed that the pressure within the aquitard has reached an equilibrated distribution, with the ultimate aquitard compaction equal to (Equation 28):

$$\eta_{aqt} = \frac{1}{2}\left(\Delta\sigma_{z,p} + \Delta\sigma_{z,c}\right)t_{aqt}\,c_{b,aqt} = 0.5(0.37\text{ bar} + 2.33\text{ bar})\,20\text{ m}\,\frac{1\times10^{-3}}{\text{bar}} = 0.027\text{ m}$$
$$= 27\text{mm}$$

The cumulative land subsidence is: $\eta_{tot} = 0.83 + 27.0 + 2.33 = 30.16$ mm.

Exercise 3 Solution

The cumulative land subsidence is due to the compaction of the three layers (Equation 13):

$$\eta_{tot} = \eta_{aquifer1} + \eta_{aquitard} + \eta_{aquifer2}$$

The compaction of each aquifer can be obtained by means of Equation 12:

$$\eta_{aquifer1} = t_{aquifer1}\, c_{b,aquifer1}\, \Delta\sigma_{z,aquifer1}$$

$$\eta_{aquifer2} = t_{aquifer2}\, c_{b,aquifer2}\, \Delta\sigma_{z,aquifer2}$$

The ultimate aquitard compaction amounts to (Equation 28):

$$\eta_{aquitard} = t_{aquitard}\, c_{b,aquitard}\; 0.5\left(\Delta\sigma_{z,aquifer1} + \Delta\sigma_{z,aquifer2}\right)$$

The sum becomes:

$$\begin{aligned}
\eta_{tot} = &\left(t_{aquifer1}\, c_{b,aquifer1}\, \Delta\sigma_{z,aquifer1}\right) \\
&+ \left(t_{aquitard}\, c_{b,aquitard}\; 0.5\left(\Delta\sigma_{z,aquifer1} + \Delta\sigma_{z,aquifer2}\right)\right) \\
&+ \left(t_{aquifer2}\, c_{b,aquifer2}\, \Delta\sigma_{z,aquifer2}\right)
\end{aligned}$$

Taking into account the relationships between the compressibility of the three layers, $c_{b,aquifer1} = 2\, c_{b,aquifer2}$ and $c_{b,aquifer1} = 0.1\, c_{b,\,aquitard}$ we can write the expression in terms of the compressibility of aquifer 1:

$$\begin{aligned}
\eta_{tot} = &\left(t_{aquifer1}\, c_{b,aquifer1}\, \Delta\sigma_{z,aquifer1}\right) \\
&+ \left(t_{aquitard}\, 10\, c_{b,aquifer1}\; 0.5\left(\Delta\sigma_{z,aquifer1} + \Delta\sigma_{z,aquifer2}\right)\right) \\
&+ \left(t_{aquifer2}\, 0.5 c_{b,aquifer1}\, \Delta\sigma_{z,aquifer2}\right)
\end{aligned}$$

Substituting the known subsidence (0.1 m), the decreased pressure in aquifers 1 and 2 (20 m and 15 m, and converting those pressures from height of water to kg/m³, so 20,000 kg/m³and 15,000 kg/m³), and their thicknesses (20 m and 40 m), as well as the 15 m aquitard thickness, results in:

$$\begin{aligned}
0.1\text{ m} = &\left(20\text{ m }c_{b,aquifer1}20{,}000\,\frac{\text{kg}}{\text{m}^2}\right) + \left(15\text{ m }10\,c_{b,aquifer1}\,0.5\left(20{,}000\,\frac{\text{kg}}{\text{m}^2} + 15{,}000\,\frac{\text{kg}}{\text{m}^2}\right)\right) \\
&+ \left(40\text{ m }0.5 c_{b,aquifer1}\,15{,}000\,\frac{\text{kg}}{\text{m}^2}\right)
\end{aligned}$$

There are 9.8067×10^{-5} bars per $1\frac{\text{kg}}{\text{m}^2}$, so:

$$\begin{aligned}
0.1\text{ m} = &\left(20\text{ m }c_{b,aquifer1}1.96\text{ bar}\right) + \left(15\text{ m }10\,c_{b,aquifer1}\,0.5\,(1.96\text{ bar} + 1.47\text{ bar})\right) \\
&+ \left(40\text{ m }0.5 c_{b,aquifer1}\,1.47\text{ bar}\right)
\end{aligned}$$

carrying out the multiplications produces:

$$0.1\text{ m} = \left(39.2\text{ m bar }c_{b,aquifer1}\right) + \left(257.4\text{ m bar }c_{b,aquifer1}\right) + \left(29.4\text{ m bar }c_{b,aquifer1}\right)$$

$$0.1\text{ m} = 326.1\text{ m bar }c_{b,aquifer1}$$

$$c_{b,aquifer1} = \frac{0.1\text{m}}{326.1 \text{ m bar}} = 3.1 \times 10^{-4} \text{ bar}^{-1}$$

and,

$$c_{b,\text{aquifer2}} = 0.5\, c_{b,\text{aquifer1}} = 1.5 \times 10^{-4} \text{ bar}^{-1}$$

and

$$c_{b,\text{aquitard}} = 10\, c_{b,\text{aquifer1}} = 3.1 \times 10^{-3} \text{ bar}^{-1} .$$

About the Authors

Giuseppe Gambolati is professor of Numerical Methods in Engineering in the School of Engineering of the University of Padova. He is the author of about 300 scientific papers in internationally refereed journals, books and proceedings, and two books of Numerical Analysis and Numerical Methods in Engineering and Applied Sciences which are used as textbooks for both undergraduate and graduate courses in the University of Padova. With Pietro Teatini he is the author of the book "VENICE SHALL RISE AGAIN" (Elsevier, 100 pp, 2014) that provides an overview of the project to raise Venice by injecting seawater into a 650-1000 deep geologic formations underlying the lagoon. He was the recipient of the 2008 IACMAG excellent contributions award for "significant contributions in research, academic activities and professional service in different regions of the globe". He is FELLOW of the American Geophysical Union (AGU) for "his unique and seminal contributions to geomechanical aspects of subsurface fluid flow". He was also appointed "Commendatore" of the order to the merit of the Italian Republic by the President Giorgio Napolitano. His research and professional activity are mainly concerned with studies of natural and anthropogenic land subsidence, groundwater flow, and subsurface contaminant transport, and the development, validation and implementation of the corresponding numerical methods and models in real world problems.

Dr. Pietro Teatini is associate professor in Hydrology and Hydraulic Engineering at the Department of Civil, Environmental and Architectural Engineering, University of Padova, Italy. In 1994 he received the International Award "Paolo Gatto", Accademia Nazionale dei Lincei, for the modeling of the aquifer system underlying the Venice Lagoon. He is co-founder of M3E S.r.l., a spin-off of the University of Padova, associated researcher at the Italian National Research Council, and associated scientists at the Key Lab of Earth Fissure and Geologic Disasters (Nanjing, China), and Key Lab of Land Subsidence Monitoring and Prevention (Shanghai, China). Currently, he is chair of the IAHS/UNESCO-IHP "Land Subsidence International Initiative - LaSII". His research interests concern modeling geomechanical issues related to fluid withdrawal and injection from/into the subsurface, specifically land subsidence and uplift, induced seismicity, and aseismic earth fissuring accompanying land subsidence. He also focusses his research interest on the evolution of managed peatlands and transitional environments. He has more than 130 papers in peer reviewed international journals.

Please consider signing up to the Groundwater Project mailing list and stay informed about new book releases, events and ways to participate in the Groundwater Project. When you sign up to our email list it helps us build a global groundwater community. Sign-up↗.

`